12-2011

Fluid Mud Underflows in Coastal Dredge Disposal

Mijanur Chowdhury
Clemson University, mchowdh@g.clemson.edu

FLUID MUD UNDERFLOWS IN COASTAL DREDGE DISPOSAL

A Dissertation
Presented to
the Graduate School of
Clemson University

In Partial Fulfillment
of the Requirements for the Degree
Doctor of Philosophy
in Civil Engineering (Applied Fluid Mechanics).

---

by
Mijanur Rahaman Chowdhury
December, 2011

Accepted by:
Dr. Firat Y. Testik, Committee Chair
Dr. Abdul A. Khan
Dr. Nigel B. Kaye
Dr. Earl J. Hayter

ABSTRACT

This manuscript presents the results of a thorough theoretical and experimental investigation on fluid mud underflows generated in a typical coastal dredge disposal operation. The main goal of this investigation is to understand the propagation dynamics of fluid mud underflows that depends upon a number of factors, including: concentrations, rheological properties and released configurations of fluid mud. Laboratory experiments were conducted with different initial fluid mud concentrations in three different experimental set-ups: rectangular flume for constant volume release, rectangular flume for constant flux release, and a square pool for radial constant flux release of fluid mud. The experiments in the rectangular flume generated two-dimensional underflows. The experiments in the pool simulated typical open water pipeline disposal operations with submerged vertical discharge configuration in the field and radially axisymmetric three-dimensional fluid mud underflows were generated in these experiments. As expected, constant volume release experiments generated gravity currents that exhibit slumping, inertial and viscous propagation phases while constant flux release experiments generated initial horizontal buoyant jets which then transform into gravity currents that exhibit inertial and viscous propagation phases. The experiments showed that the propagations of underflows were significantly influenced by the non-Newtonian rheology of released fluid mud. Underflows formed by initial low concentration of fluid mud release did not experience the viscous propagation phase in the limited experimental set-ups that were used in the experimental investigation. However, high concentration fluid mud releases rapidly transitioned into viscous

propagation phase, sometimes even bypassing the expected inviscid phase. The inter-transitions of propagation phases were determined from experimental data and they were related to the initial source parameters by deriving order-of-magnitude expressions for transitions. The theoretical part of this investigation also includes experimental evaluation of three mathematical modeling approaches to model the inertial and viscous propagation of fluid mud gravity currents. These three mathematical modeling approaches are, from simplest to the most complex: force-balance, box model and shallow water/lubrication theory approximation. The force-balance and box model solutions for viscous propagation of non-Newtonian gravity currents were non-existent and hence, derived in this investigation. For the inertial propagation of fluid mud gravity currents, it was concluded that box model would be the most efficient analytical model due to its closed-form solution for all of the release configurations, and its predictive accuracy (based upon its experimental evaluation and inter-comparison of the models). For the viscous propagation, self-similar solution based on the lubrication theory approximation would be the better choice. However, only box model solution can provide analytical solution for all possible release configurations which make it a good alternative, especially for quick predictions. The results of this study are expected to be useful for predicting the temporal fate of fluid mud underflows in coastal dredge disposal operations.

Keywords: Dredge disposal, pipeline disposal, fluid mud, underflows, gravity current, box model, shallow water model, force-balance, viscous propagation, non-Newtonian fluid, turbidity current.

DEDICATION

Dedicated to my parents, *nana* (M. A. Quasem Chowdhury), and *nani* (Mrs. M. A. Quasem Chowdhury), without whom I would not be who I am now.

ACKNOWLEDGMENTS

At first, I express my heartfelt gratitude to my advisor and the chairman of my doctoral dissertation committee, Dr. Firat Y. Testik, for his constant encouragement, guidance, critical evaluation, and valuable suggestions in conducting this research and preparation of this manuscript. Working with him has been a fruitful and enjoyable learning experience. I also thank the members of my doctoral dissertation committee, Dr. Abdul A. Khan, Dr. Nigel B. Kaye, and Dr. Earl J. Hayter for their critical reviews of this manuscript, helpful suggestions, and insightful comments which helped me to make this manuscript complete.

I also highly appreciate the help and cooperation of the members of Flow Physics Laboratory, especially Mike Jacobson, Nazli Yilmaz, and Jiwon Mun in conducting the experiments. Special thanks are due to Mr. Danny Metz of Glenn Department of Civil Engineering, Clemson University for the design and fabrication of the experimental setups. Support for this research was provided by the U.S. Army Corps of Engineers under grant number W912HZ-09-C-0068 which is gratefully acknowledged.

Last but not the least; I owe the deepest appreciation to my brothers – Mahfuz and Riaz, my younger sister – Shadika, and my wife – Samira for their patience and emotional support throughout the entire period of my extended studentship.

TABLE OF CONTENTS

Page

III. EXPERIMENTAL SETUP, METHODOLOGY AND MEASUREMENT TECHNIQUES

IV. PROPAGATION PHASES AND THEIR TRANSITIONS

V. INERTIAL PROPAGATION OF FLUID MUD UNDERFLOWS

VII. CONCLUSIONS AND FUTURE WORK

LIST OF TABLES

LIST OF FIGURES

List of Figures (Continued)

Figure Page

List of Figures (Continued)

List of Figures (Continued)

Figure Page

CHAPTER ONE

INTRODUCTION

In this chapter, first the problem statement and the motivation for this doctoral research are discussed in detail. Then the objectives and approach of this research are outlined. Finally, the organization of the dissertation is given.

1.1 Statement of the Problem

Each year large volumes of sediments are dredged from rivers, waterways, ports and harbors around the world primarily to maintain and enlarge their navigability. An estimated 230 million cubic-meters of sedimentary materials are dredged by the U.S. Army Corps of Engineers in the United States annually (Hales, 1996). Much of these sedimentary materials dredged (especially those from rivers, channels, lakes and estuaries) are cohesive fine-grained fluid mud that consists of water, cohesive sediment particles (clay and silt), and organic material (McAnally, 2007; Teeter, 1992b). Each year the United States spends more than $100,000,000 on dredging operations to remove the fluid mud for maintaining safe navigation in U.S. waters (McAnally et al., 2007). Among the different dredging methods employed in removing fluid mud, the hydraulic pipeline dredging method is one of the most common and economical methods for the maintenance dredging of rivers, estuaries or channels (Barnard, 1978). In this method, the hydraulically dredged fluid mud is generally pumped and then transported through a suitable pipeline to dispose into a designated aquatic disposal area (Neal et al., 1978; Schubel et al., 1978). As soon as they are discharged, the fluid mud starts to descend in

the water column and then flow away from the impingement point at the bottom in the form of an underflow due to the density difference of the fluid mud and the ambient water (Nichols et al., 1978). It is estimated that 99% of the disposed fluid mud in an open water pipeline disposal operations are transported in the form of fluid mud underflows (Nichols et al., 1978; Teeter, 2001). Therefore, the propagations of the underflows play the key role in determining the fate of the discharged fluid mud. In order to develop predictive models for the fate of the discharged fluid mud, it is of importance to understand the propagation dynamics of fluid mud underflows in relation to a number possible controlling factors for a particular disposal operation, namely: density and rheological properties of the discharged fluid mud, depth of the disposal areas (shallow or deep water), release configurations (constant volume or constant-flux release), discharge port configurations (above-water, submerged, discharge angle with the horizontal), ambient water condition (e.g. presence of current and shear stresses) and bathymetry of the bottom (e.g. presence of slope) (Teeter, 2000). *The main goal of this research is to understand the propagation dynamics of fluid mud underflows based on a thorough experimental and theoretical investigation.* The investigation focuses on studying the propagation dynamics of the underflows in relation to the density, rheological properties and release configurations of fluid mud. The influence of other controlling factors such as ambient water conditions and bathymetry of the bottom have not been investigated.

1.2 Motivation

It is evident that the central concern in any open-water disposal operation is the possible environmental impact from the dispersion of the discharged dredged materials on the receiving water environment. This concern is particularly significant in open-water pipeline disposal case because the dredged sediments in this case are mostly cohesive fine-grained which are most susceptible to dispersion (Barnard, 1978). Having the majority of the discharged fluid mud, the fluid mud underflows can be extremely harmful to the receiving aquatic environment (Teeter, 2001). They are believed to be highly dispersive in nature and may propagate several kilometers away from the source depending upon a number of factors such as the bottom slope, the ambient flow field and the released volume of slurry among others. For example, Teeter (2002) observed an underflow propagation of approximately 3 kilometers for the pipeline discharge of approximately $5.2\times10^5\ m^3$ fluid mud. Hence, as the fluid mud underflow spreads, it may overrun everything in its path, killing benthos such as clams and oysters (Nichols et al., 1978). If there is a high bed shear stress, entrainment of the underflows by the ambient water can generate a turbid plume of suspended sediment in the water column (Teeter, 2001). This turbid plume may pollute the water quality and block sunlight, harming underwater flora and fauna. Since dredge material is usually disposed in nearby open water in pipeline disposal, when the fluid mud spreads over a broad area, it may backfill the dredged channel. In addition, the discharged fluid mud may also contain contaminants entrained from the dredging site (Mcanally et al., 2007). If the underflow propagates a broad area, it may pollute the water in this whole area by releasing those contaminants.

An integral part of the assessing the environmental impacts during open water pipeline disposal operation is to predict the post-disposal dispersion behavior and hence, the fate of the discharged fluid mud (Brandsma and Divoky, 1976). In addition, the estimations of the post-disposal dispersion behaviors and the fate of the discharged fluid mud are also required to satisfy the applicable standard for disposal such as meeting the Clean Water Act (Teeter, 2000) and other conventions (see Burt and Fletcher, 1997) as well as to properly select the location and size of the disposal sites, and the specification conditions of the discharge. However, the fates of the discharged fluid mud largely depend on the propagation dynamics of the fluid mud underflow formed at the bottom. Therefore, it is of great environmental importance to investigate the propagation dynamics of such fluid mud underflows. Realizing the importance, a thorough laboratory and theoretical investigation was conducted to analyze the propagation dynamics of fluid mud underflows. The results of this investigation are presented in this dissertation.

There have been very limited analytical, laboratory or field investigations that thoroughly investigate the behavior of fluid mud underflows, generated in a typical open water pipeline disposal operation. Laboratory and field studies had been carried out by Neal et al. (1978), Nicholes et al. (1978), and Thevenot et al. (1992) on the short and long term fate of discharged fluid mud in a typical open water pipeline disposal operation. Those studies mostly focused on the estimation of turbidity generation by fluid mud dispersion. Recently, Teeter (2002) conducted field experiments to evaluate their proposed model for predicting dispersion in open water pipeline disposal operation in Teeter (2001). However, they mainly focused on evaluating their numerical model with

the field data, rather than analyzing the propagation dynamics of fluid mud. As it will be presented in the Chapter 4, 5 and 6 of this dissertation, after the initial short duration of its formation at the impingement point, the fluid mud underflow during a typical open water pipeline disposal operation is generally a gravity current of fluid mud. Since gravity current is a ubiquitous phenomenon, different forms of gravity currents have been studied in many fields (see Simpson, 1997 for different applications). Therefore, there is a large body of literature on different forms of gravity currents (especially, saline gravity currents); the propagation dynamics of which is now well understood based a large number of experimental studies. Based on the understanding of their propagation dynamics, different types of simple analytical mathematical models (e.g. force-balance, box model, shallow water model, lubrication approximation) have been used successfully to approximate the propagation of the gravity currents. However, the earlier theoretical investigations on fluid mud gravity flow (e.g. Teeter, 2002 and Van Kessel and Kranenburg, 1996) mainly provided complex numerical models, rather than simple mathematical models that provide analytical solutions for the quick prediction of the propagation. One of the goals of this investigation is therefore to investigate the flow dynamics of the fluid mud underflows in four different laboratory set-ups and then evaluate the predictions of the some widely-used analytical mathematical models using our experimental observations.

An important complexity associated with the fluid mud underflows is that fluid mud suspensions exhibit profound non-Newtonian behavior (Teeter, 1992b). Therefore, their propagation dynamics when the viscous force becomes pronounced will be

governed by their non-Newtonian behavior. There has not been a thorough understanding how the non-Newtonian rheological characteristics influence the propagation dynamics of a gravity current, mainly because of the lack of experimental studies. Therefore, an important focus of this investigation is determining the impact of the rheological properties on the propagation dynamics of fluid mud underflows.

Apart from the open-water pipeline disposal case, fluid mud underflows may also occur naturally. For example, they can be generated from the cohesive beds after they are fluidized by waves and currents (McAnally et al., 2007), submarine landslide (Jiang, 1993a;1993b), mountain slide by the torrential rain (Mei and Yuhi, 2001). This study would also be useful to understand the propagation dynamics of those naturally occurring fluid mud gravity flows.

1.3 Research Approach and Objectives

The goal of this research is to investigate the propagation dynamics of fluid mud underflows. Our approach in this investigation is in two fronts: laboratory experiments and then mathematical modeling of the experimental observations of the fluid mud underflows. Though the fluid mud underflows are three-dimensional (i.e. radial, henceforth the term radial and three-dimensional are used interchangeably) in open water pipeline disposal operation, we first investigated two-dimensional fluid underflows, a simplified representation of radial underflows. In two-dimensional investigation, laboratory experiments were carried out for fixed volume and constant flux release of dense fluid mud. The constant flux release experiments represent the underflows

generated from the continuous discharge of fluid mud in a typical open water pipeline disposal operation. However, once the discharge of fluid mud is interrupted or completed in a particular disposal operation, the underflow may still propagate resembling fixed volume underflows. Investigation is underway for the radial fluid mud underflows. The major objectives of this work are the followings:

- To investigate the propagation dynamics of the two-dimensional and radial fluid mud underflows through laboratory experiments.

- To determine how the non-Newtonian rheology of the fluid mud influences the dynamics of the underflows.

- To model the flow characteristics of fluid mud underflows. Where available, existing mathematical models are used and when needed, new models are derived.

- To model the transition of the propagation phases from one phase to another phase.

- To provide a large data set of the propagation characteristics of fluid mud underflows.

1.4 Organization of the Dissertation

This dissertation is organized as follows. In Chapter 2, a literature review related to the fluid mud underflows in coastal dredge disposal is given. Experimental set-ups,

methodology and measurement techniques for the experimental investigation of fluid mud underflows are provided in Chapter 3. The propagation phases (e.g. Jet/Slumping, inertia-buoyancy and viscous-buoyancy phases) and the transition among the propagation phases of the fluid mud underflow experiments are discussed in Chapter 4. Then, the inertial propagation (inertia-buoyancy phase) of the fluid mud underflows is approximated with the three existing mathematical models (force-balance, shallow water and box model) in Chapter 5. In Chapter 6, the force-balance and the box model solution for non-Newtonian viscous propagation (viscous-buoyancy phase) are derived. It also provides the modeling of the viscous propagation (viscous-buoyancy phase) of the fluid mud underflows with these two newly derived models (force-balance and box models) and existing lubrication theory approximations. They are followed by the conclusions and future works in Chapter 7.

CHAPTER TWO

LITERATURE REVIEW

In this chapter, a review of literature related to the fluid mud underflows generated in a typical open water pipeline disposal operation is provided. In Section 2.1, the relevant technical information on the open pipeline dredge disposal is summarized. Then, the characteristics of fluid mud suspension are discussed in Section 2.2. Section 2.3 presents the dispersion processes that the discharged fluid mud experiences in a typical open water pipeline disposal operation. Then, the subsequent sections are devoted in illustrating the dynamics and characteristics of the dispersion processes. The discussion is mostly focused on the process of interest of this investigation (i.e. fluid mud underflows).

2.1 Pipeline Dredge Disposal

Hydraulic pipeline dredging is usually carried out for the maintenance dredging of rivers, estuaries or channels located near rivers and estuaries. Generally, any dredging process consists of three phases: removal or excavation of the dredged materials from the channel bottom using a suitable dredger, transportation of the dredged materials by a suitable method and then, utilization or disposal of the dredged materials (USACE, 1983). In order to remove them from channel bottom in a hydraulic dredging operation, the fluid mud are generally pumped and then transported through a suitable pipeline (Henry et al., 1978). Due to its economic viability, a common method of disposing fluid mud in hydraulic pipeline dredging operations is to discharge them into designated open-water or occasionally side channel disposal areas near the dredging site (Neal et al., 1978;

Barnard et al., 1978). The disposal area is generally located within 1000 meters from the dredging site (Johnson, 1974; Barnard 1978). The discharge port (i.e. end of the pipeline) may be either above water or submerged and the dredging and hence, the disposal operation is normally continuous, but occasionally may be interrupted by mechanical breakdown, ship traffic, or bad weather (Barnard, 1978). The important parameters to characterize a hydraulic pipeline disposal operation are: the flow rate of the discharged fluid mud, the water depth at the discharge location, characteristics of dredged materials, discharge configuration, solid contents and bulk density of the fluid mud, and pipeline diameters among others. Though the values of the parameters can be widely varied depending on the particular maintenance dredging operations, Table 2.1 shows typical values for these parameters. The disposed materials in the form of fluid mud in open-water pipeline disposal operations are mainly fine-grained sediments such as silt, clay or both (Nichols et al., 1978).

2.2 Characteristics of Fluid Mud

Fluid mud is generally considered to be a cohesive fine-grained sediment suspension in which settling is substantially hindered. The fine grained sediments primarily are clay- and silt-size particles; with size less than 74 microns (McAnally et al., 2007a; Teeter, 1992b). A typical fluid mud sample with low organic content usually consists of 50-70% clay-sized particles and silt-sized particles are usually secondary to clay. Larger particles (e.g. sand) are occasionally entrained into the fluid mud, but their rapid settling tendency keeps them to less than a few percent. Different types of organic

matter and contaminants can also be entrained from the dredging site in the fluid mud (Mcanally et al., 2007a). Unlike non-cohesive suspension, fluid mud can persist in a fluid-like state for long periods due to largely the cohesive nature of the suspended particles. In the context of dredging, the fluid mud suspension mass concentration, C_m ranges from about 50 to 350 dry-g/L, corresponding to bulk wet density, ρ_m ranges from 1.05 to 1.25 wet-g/cu-cm or to volume concentration, C_v [$C_v = V_s/(V_s + V_w)$, where V_s and V_w are the volume of suspended sediment and water in the prepared suspension, respectively] of 0.02 to 0.13 cm^3 solids/cm^3 mud (Teeter, 1992b).

Table 2.1. Typical conditions for open-water pipeline disposal operations (Barnard, 1978; Brandsma and Divoky, 1976; USACE, 1983)

Parameters	**Typical Values**
Pipeline diameter, d_0 (m)	0.1-0.5
Discharge velocity, u_0 (m/s)	4-6
Depth of water, H (m)	6-12
Type of dredged material	fine-grained (silt, clay)
Concentration of the fluid mud (g/L)	50-350
Solid contents of the fluid mud (%)	10-20
Volume concentration of the fluid mud, C_v	0.02-0.13
Bulk densities of the fluid mud (kg/m^3)	1050-1250
Discharge angle below the horizontal (˚)	0, 90

Behaviors of cohesive fluid mud vary widely depending on the compositions (e.g. particle size distributions, organic contents and pore water chemistry), state, imposed shear stress, shear history and time. Therefore, fluid mud from different locations can act

differently, even at the same concentration or density (Teeter, 1992a; 1992b). However, they always exhibit profound non-Newtonian behavior, exhibiting strong dependency of viscosity with shear rate (Teeter, 1992a; Whitehouse et al., 2000). Non-Newtonian behavior can be a nonlinear stress-strain relationship (referred to as viscoelastic or viscoplastic fluid), or yield stress below which a stress produces no deformation (pseudo-plastic) depending on the characteristics of a particular fluid mud sample (Teeter, 1992b; McAnally, 2007a). Thixotropy is another important characteristic of fluid mud when subjected to constant, sufficiently high strain or stress. Hence, the rheological properties (e.g. viscosity, yield stress) can gradually decrease in time (McAnally, 2007a).

Many constitutive models have been applied to describe the non-Newtonian behavior of fluid mud suspensions. The general form of expression which is mostly used to describe its rheological properties is called the Hurschel-Buckley constitutive equation, defined as (Huang and Garcia, 1998):

$$\tau = \tau_y + m\left|\frac{\partial u}{\partial z}\right|^{n-1}\frac{\partial u}{\partial z}. \tag{2.1}$$

Here τ is the shear stress, τ_y is the yield stress, u is the x-velocity component, $\partial u/\partial z$ is the shear rate, n is the flow behavior index which is a positive real number, and m is the consistency index of the suspension. τ_y, m and n are determined experimentally. When n=1, this expression simplifies to the Bingham plastic model equation.

The Herschel-Bulkley model is often simplified to the Ostwald power-law model given in Eq. (2.2), which can be considered as an asymptotic case of the Herschel-Bulkley model with yield stress, $\tau_y = 0$.

$$\tau = m \left| \frac{\partial u}{\partial z} \right|^{n-1} \frac{\partial u}{\partial z}. \tag{2.2}$$

The power-law model describes pseudo-plastic (i.e. shear-thinning) fluids for the case of $0 < n < 1$, dilatants or shear-thickening fluids for the case of $n > 1$, and Newtonian fluids for the case of $n = 1$. Often fluid muds are shear thinning, but have a lower-limit of viscosity at high-shear rates (see Teeter, 1992b; McAnally, 2007a, Huang and Garcia, 1998 and Coussat and Piau, 1995). The rheological properties of fluid mud have also been modeled using the Bingham plastic model especially for high shear rates (see Mei and Liu, 1987; Van Kessel and Kranenburg, 1996; and Huang and Garcia, 1997).

2.3 Dispersion Processes and the Process of Interest

In a hydraulic pipeline dredging operation, the dredged material is pumped as fluid mud through a pipeline and then discharged at the disposal site as a continuous stream. As soon as the fluid mud exits the pipeline, any coarser material (e.g. gravel, clay balls or coarse sand) will immediately settle to the bottom of the disposal area and usually accumulates directly beneath the discharge point (USACE, 1983). The dispersion of the remaining vast majority of the pipeline-discharged fluid mud can be divided into three distinct processes (Thevenot et al., 1992):

1. Initial descent of the discharged fluid mud and impingement on the bed

2. Underflows of fluid mud on the bottom.
3. Passive dispersion of the suspended sediments in the water column, often called turbidity plume.

A conceptual sketch of the three dispersion phases is shown in Fig. 2.1.

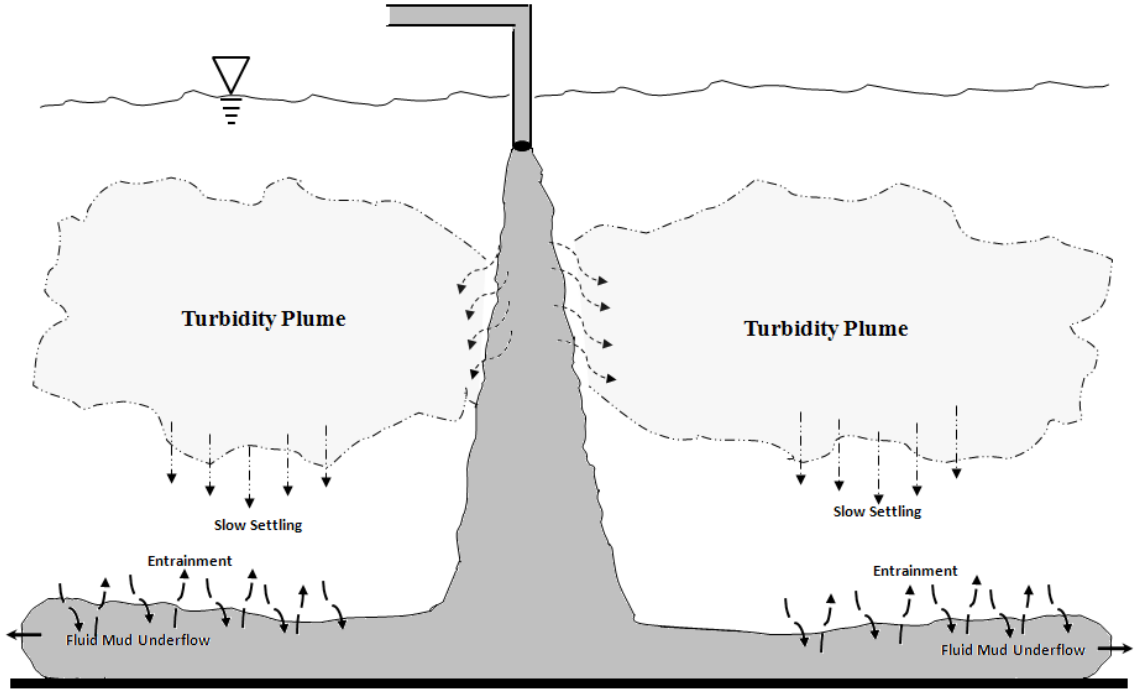

Figure 2.1. Conceptual sketch of the dispersion phases of the discharged fluid mud in a typical open water pipeline disposal operation.

Though the dispersion of pipeline-discharged fluid mud usually consists of the three processes, the nature, degree and extent of each dispersion process are controlled by the discharge conditions of a particular disposal operation and mainly dependent on the following controlling factors: characteristics of the dredged fluid mud (e.g. size distribution of sediment particles, solid concentration, and composition), depth of the disposal areas (shallow or deep water), discharge port configurations (above-water,

submerged, discharge angle with the horizontal), ambient water condition (e.g. presence of current and shear stresses) and bathymetry of the bottom (e.g. presence of slope). The first dispersion phase is regarded as the near-field dispersion process whereas the second and third processes are regarded as far-field dispersion processes. Far field dispersion processes are of greatest environmental concern (Thevenot et al., 1992). The turbidity plume (i.e. third dispersion process) is usually formed by the very fine particles during the interaction of descending buoyant jet of fluid mud with the ambient water and they can be dispersed by a number of processes: turbulent diffusion, shear dispersion and advection by current among others (Neal et al., 1978). It is estimated that the turbidity plume accounts for only 1-3% by mass of the discharged fluid mud while the remaining fluid mud disperse as fluid mud underflows from the impingement point (Neal et al., 1978). Therefore the main focus of this research is on the fluid mud underflow which is the key propagation process of the two far-field dispersion processes as it disperses the majority of the discharged slurry in a typical open water pipeline disposal operation. The fluid mud underflow from the impingement point can also be divided into two main regimes (Chen, 1980; Papakonstantis and Christodoulou, 2010): momentum-dominated wall jet and buoyancy-dominated fluid mud gravity flows. Clearly, these two regimes of fluid mud underflows are generated after the buoyant jet of the slurry impinges the bottom and hence, the source of the inflow for the fluid mud underflows is at the impingement point of the buoyant jet. Hence, the characteristics of the buoyant jet of fluid mud will play vital role for the propagation of fluid mud underflows. Therefore, in the next section, a brief review of the buoyant jet characteristics is given which is

followed by the detailed discussion on the two regimes of fluid mud underflows. Note that there could be another propagation regime in between of these two regimes which is characterized by a balance between the radial momentum flux and the rate of change of the inertial force (Papakonstantis and Christodoulou, 2010). However, there have not been enough evidences that this regime may occur in most of the flow conditions and the physics behind this regime was limited in scope. It was observed in the experimental study by Kotsovinos (2000) on axisymmetric intrusion of saline gravity flows. Hence, this regime will not be considered in this dissertation.

2.4 Descent of the Discharged Fluid Mud to the Bed

After exiting the discharge port (e.g. end of the pipeline), the majority portion of the discharged fluid mud starts to descend in the water by forming a buoyant jet. The buoyant jet of the fluid mud is created due to the high momentum of the discharged fluid mud as well as the density difference between the fluid mud and the water (Hall et al., 2010). Since the fluid mud jet contains sediments unlike single-phase jet (e.g. jet of brine solution), it is a two-phase buoyant jet. However, the analysis of the two-phase sediment-laden turbulent jets is still under active investigation both theoretically and experimentally, compared to single-phase jets (Jiang et al., 2005). Therefore, definitive conclusions are not available for many physical characteristics of the two-phase sediment-laden buoyant jets. However, limited investigations of two-phase sediment laden jets such as in Jiang et al. (2005) and Hall et al. (2010) revealed that their behavior mostly conform to their single-phase counterparts. To our knowledge, none of the

investigations on two-phase jets used cohesive particle such as clay or silt in their investigations. Only Thevenot et al. (1992) provided some experimental observations on the certain aspect of buoyant jet from cohesive mud slurry. However, their investigation is far from complete. Therefore, due to the scarcity of the studies on two-phase cohesive particle-laden buoyant jets, we will mostly use the concept of single-phase buoyant jet when it is not available for two-phase jet.

As noted earlier, there can be a number of discharge configurations in open water pipeline disposal operations, mainly: submerged downward (Fig. 2.2a), submerged horizontal (Fig. 2.2b) and above water horizontal (Fig. 2.2c). In a particular disposal operation, when the dispersion in the water column or free surface needs to minimized, submerged discharge configuration is expected to be chosen since there is no interaction of the descending jet with the free surface in this configuration (Thevenot et al., 1992). On the other hand, if the minimization of the propagation distance of the bottom propagation is desired, above surface discharge would be a good choice. Choosing an above surface vertically downward discharge would not be practical since horizontal discharge will be more effective to minimize the propagation distance of the bottom propagation. Conceptual sketches of the three discharge configurations are shown in Fig. 2.2. Please note that the results of the investigation on this dissertation only focus on the submerged downward configuration (Fig. 2.2a). It is expected that the information gained from this investigation would be the basis for the other two discharge configurations.

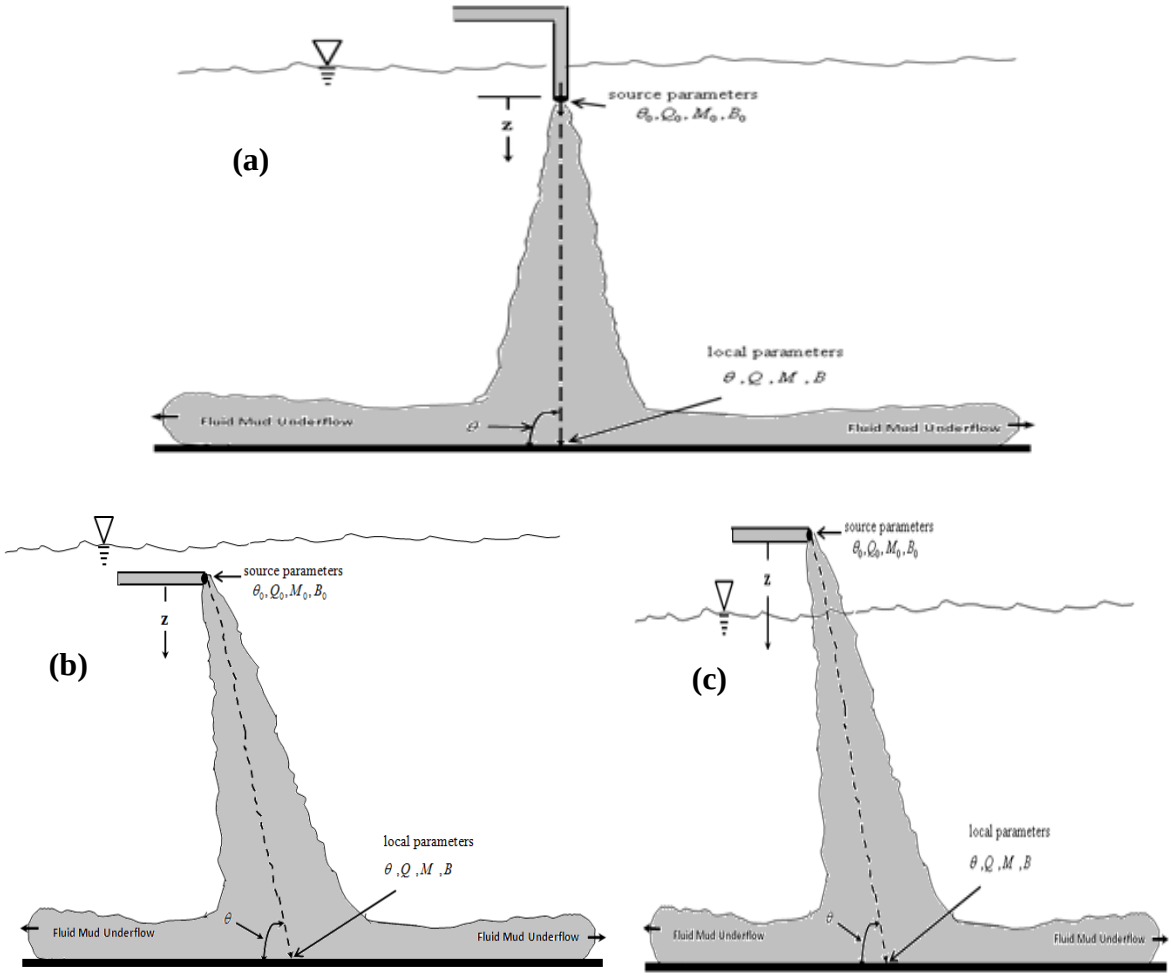

Figure 2.2. Conceptual Sketch of the three discharge configurations of the open-water pipeline disposal, a) submerged vertical, b) submerged, and c) above-water horizontal configurations.

As is seen in Fig. 2.2a, the fluid mud with a density ρ_m is discharged with a velocity, u_0 from the discharge port of diameter, d_0 in open water with density, ρ_a having a depth of H. The distance between the discharge port to the bottom is z^* and the jet impinges the bottom at an angle, θ. The main flow parameters are the initial (at the source) specific volume flux $Q_{0,}$ initial momentum fluxes M_0 and its initial buoyancy flux B_0 defined for the round jet as (Jirka and Doneker, 1992):

$$Q_0 = \frac{1}{4}\pi d_0^2 u_0; \quad M_0 = \frac{1}{4}\pi d_0^2 u_0^2; \quad B_0 = g_0' Q_0$$

Here, $g_0' = \frac{g(\rho_a - \rho_m)}{\rho_a}$ is the negative buoyancy gradient which is also called apparent/reduced acceleration of gravity at the source. The buoyant jet of the slurry would have jet like characteristics depending on its initial volume flux, Q_0, initial momentum fluxes, M_0, and plume like characteristics depending on its initial buoyancy flux, B_0, (Fischer, et al., 1981). The densiometric Froude number Fr_0 and Reynolds number Re_0 at the source are defined as:

$$Fr_0 = u_0 / \sqrt{g_0' d_0}$$

$$\mathrm{Re}_0 = u_0 d_0 / \nu$$

Here ν is the viscosity of the slurry. If the source Reynolds number, Re_0 is such that $\mathrm{Re}_0 \geq 3000$, it ensures fully turbulent source flow conditions and viscous effects then can be neglected (Cavalletti and Davies, 2003). Note that the above definitions of Re_0 and the fully turbulent source flow condition are for a buoyant jet of Newtonian fluid while the discharged fluid mud in pipeline disposal operation are generally non-Newtonian. To the best of the author's knowledge, there has not been any experimental study which provided a condition for turbulent source flow based on a non-Newtonian Reynolds number.

The simplest configuration for open-water pipeline disposal operation is the vertically downward submerged discharge in stagnant water (see Fig. 2.2a), which is the focus of this dissertation. In this configuration, since the discharge is submerged there is no interaction with the water surface. Having no horizontal shear in the water column, the dilution in the water column will also be minimal. Since the receiving water is stagnant and homogeneous, the turbulent buoyant jet behavior will be dependent on Q_0, M_0, B_0 and the distance from the source point, z, provided that the buoyant jet is fully turbulent so that the viscous effects can be neglected (Fischer et al., 1979). Two important lengths scales, discharge length scale - l_Q and jet/plume transition length scale - l_M, derived from dimensional analysis describe the relative importance of the fluxes (i.e. Q_0, M_0 and B_0) on the behavior of the buoyant jet (Fischer et al., 1979: Jirka, 1992) where:

$$l_Q = \frac{Q_0}{M_0^{1/2}}$$

$$l_M = \frac{M_0^{3/4}}{B_0^{1/2}}$$

The first length scale, l_Q is important in the analysis of jet and the second, l_M includes the effect of buoyancy. When $z \gg l_Q$ the flow is fully developed jet and when $z \sim o(l_Q)$, the flow is controlled by the jet exit geometry. The ratio l_Q / l_M is called jet Richardson number. When $z \ll l_M$, the flow is momentum-driven, hence jet-like, and buoyancy effects are secondary, and when $z \gg l_M$ the flow is buoyancy-driven, hence plume-like. Previous investigations on single-phase buoyant jets revealed that the flow will be jet-like

when $z < p_j l_M$ where p_j is a constant which has been found to vary between 0.5 – 1 [e.g. $p_j = 0.53$ in Chen and Rodi (1980), 0.6 in Wang and Law (2002) and 1 in Papanicolaou and List (1988)]. On the other hand, the flow will be plume-like when $z > p_p l_M$ where p_p is a constant which has been found to vary between 5 – 6 [e.g. $p_p = 5.3$ in Chen and Rodi (1980), 6 in Wang and Law (2002) and 5 in Papanicolaou and List (1988)]. The region between $p_j < \frac{z}{l_M} < p_p$ is the transitional region where both buoyancy and momentum govern the behavior of the buoyant jet. Therefore, given enough flow depth (i.e. $z \gg 6 l_M$), all buoyant slurry jets will eventually act as plumes. Determining whether a buoyant jet of the discharged fluid mud shows a plume-like or jet-like behavior at a particular instant (especially at the impingement point) is of importance since it may dictate the behavior of the bottom propagation of the fluid mud from the impingement point. For example, if discharge is carried out in very shallow water, the buoyant jet may impinge the bottom as a jet, since it did not travel enough distance to transition into a plume. In this case, from the impingement point, the fluid mud may spread in all directions as a wall jet before making a transition into a radial gravity current. On the other hand, if there is a sufficient flow depth, the initial buoyant jet will impinge the bottom as a plume. In this latter case, an extended wall jet may not be expected and buoyancy would dominate in the bottom propagation of the discharged fluid mud.

The descent of the buoyant jet of the fluid mud until its impingement to the bottom may be classified into two main distinct regions: zone of flow development and

zone of developed flow (Fischer, et al., 1981; George, 1980). The initial phase of the buoyant jet behavior occurs in the vicinity of the outlet port called zone of flow development region. In this region, the axial velocity maintains the source value (Jiang et al., 2005). The shearing action at the edge of the jet causes a decrease in the edge velocity, but it does not affect the velocity near the center of the jet (George, 1980). For a single-phase turbulent jet of high Re, the flow development region extends a length of about $6d_0$ (Rajaratnam, 1976). Physically, the limit of this region is where the mixing zone penetrates the center of the jet (George, 1980). Jiang et al. (2005) estimated the length of zone of development region for two-phase jets by an empirical expression, while Hall et al. (2010) found the same length of single phase jets. For two-phase sediment-laden jet, Jiang et al. (2005) reported that, in a dilute sediment-laden jet, if the sediment density is close to that of the fluid, the zone of flow development for the sediment velocity should be similar. However, since the sediment is typically heavier, the zone of flow development for the sediment velocity will be longer for a downward jet due to the sediment inertia. A detailed experimental investigation is needed for an accurate quantification of the length of the zone of flow development for fluid mud buoyant jet. Dilution and propagation are minimal in the zone of flow development and the transverse plume velocity and concentration profiles in this zone develop from top-hat to Gaussian shape (Thevenot et al., 1992).

In the developed flow region, starting right after the flow development region, the buoyant jet continues to expand and the mean velocity and concentration decays (Fischer et al., 1979). Unabated entrainment that is driven by the turbulent eddies occurs there.

The mean velocity and concentration profiles in this zone are self-similar; hence, they can be expressed in terms of a maximum value (measured at the jet centerline) and a measure of width (Fischer et al., 1979). The functional forms of velocity and concentration profiles are Gaussian (Fischer et al., 1979; Wang and Law, 2002) for single phase flows. Jiang et al. (2005) reported Gaussian velocity and concentration profiles also for the sediment-laden two phase jet flows. As the buoyant jet descents, the centerline velocity of the jet is decreased and the energy of the jet is diffused into the surrounding fluid. This process continues until all the initial energy of the jet is dissipated, or until the influence of a boundary causes an impinging flow region (George, 1980).

The buoyant jet characteristics at a distance, *z*, from the port will depend on whether it behaves as a momentum-dominated jet or buoyancy-dominated plume. Some of the expressions for the important characteristics of both types of flows are tabulated in Table 2.2. Note that the expressions tabulated in Table 2.2 for the buoyant jets of the fluid mud are for the zone of developed flow region. Perhaps, the behavior of the buoyant jets of the discharged fluid mud at the impingement point of the bed is most relevant to open water pipeline disposal operations because the impingement point characteristics dictate the behavior of the fluid mud underflow from the discharge point.

Table 2.2. Buoyant jet characteristics at a downward vertical distance *z* from the discharge source. The information was compiled from a number of sources (e.g. Wang and Law, 2002; Fischer et al., 1979; Papanicolaou and List, 1988). Notations: *z* – vertical distance from the discharge port, *x* – axial distance from the center of the jet; η_{jw}, η_{pw}, $\eta_{jc}, \eta_{pc}, k_{jw}$ and k_{pw} are all empirical constants for the respective expressions (w - velocity and *C* – concentration; Subscripts: *c*- center line, *0* – initial value at the source, *j* - jet, *p* – plume).

Characteristics	**Jet**	**Plume**
Mean velocity distribution across buoyant jet, *w*	$w = w_c \exp[-(x/\eta_{jw} z)^2]$ $\eta_{jw} = 0.103 - 0.115$	$w = w_c \exp[-(x/\eta_{pw} z)^2]$ $\eta_{cw} = 0.126 - 0.136$
Mean concentration distribution across buoyant, C	$C = C_c \exp[-(x/\eta_{jc} z)^2]$ $\eta_{jc} = 0.126 - 0.136$	$C = C_c \exp[-(x/\eta_{pc} z)^2]$ $\eta_{pc} = 0.109 - 0.125$
Decay of the center-line axial velocity, w_m	$w_c = k_{jw} w_0 d_0 / z$ $k_{jw} = 5.8 - 6.8$	$w_c = k_{pw} B_0^{1/3} z^{-1/3}$ $k_{pw} = 3.4 - 4.13$
Centerline mean concentration, C_m	$C_c = k_{jc} C_0 d_0 / z$ $k_{jc} = 4.96 - 5.4$	$C_c = k_{pc} Q_0 / M_0^{1/2} (z/l_m)^{2/3}$ $k_{pc} = 9.1 - 11.3$

The important local jet parameters at the impingement point are: local specific momentum flux *M*, buoyancy flux *B*, volume flux *Q*, and apparent acceleration to gravity, g'. These parameters are generally different from the initial ones at the source (Papakonstantis et al., 2010). These local parameters at the impingement point are generally estimated using well-established integral models (e.g. Wang and Law, 2002; Fan, 1967; Jirka, 2004) or analytical solutions (e.g. List and Imberger, 1973; Papanicolaou and List, 1988). In integral models, the conservation equations of mass, momentum and buoyancy fluxes are integrated over the jet cross section to yield a set of

ordinary simultaneous differential equations. The solution of these equations yields the parameters at the impingement point (Koh and Brooks, 1975; Wang and Law, 2002). In submerged vertically downward discharge configuration, if there is no shear stress in the water column to interact with the descending jet, the impingement angle, θ (see Fig 2.2a) is expected to be close to 90° which is in line with the experimental observations by Papakonstantis et al. (2010). The impingement angle, $\theta = 90^{\circ}$ signifies that fluid mud spreads away approximately in equal magnitude in all directions (Papakonstantis and Christodoulou, 2010) and hence, the shape of the propagation fluid mud from the impingement point will be circular and radially axisymmetric.

For the horizontal discharge configuration (Fig. 2.2b and 2.2c), the trajectory of the descending jet would be elongated as it is qualitatively shown in Fig. 2.2b and 2.2c. In these discharge configurations, the impingement angle, θ is not expected to be 90° due to the elongation of the trajectory as observed by Papakonstantis and Christodoulou (2010). They found that the bottom propagation in this case is non-circular, not radially symmetric and the downstream propagation is more pronounced that that of the upstream one. A more in-depth experimental investigation is needed to relate the impingement angle, θ to the discharge angle, θ_0. Since the source of the inflow for the fluid mud underflows is at the impingement point, the local parameters at the impingement point (M, B, Q, g') rather than the discharge source parameters (M_0, B_0, Q_0, g_0') should be taken as the source parameters for the fluid mud underflows. Although a steady source constantly feeds the underflow from the impingement point, the propagation rate is

expected to slow down with time and distance (especially for the horizontal bottom) as the kinetic energy of the slurry is spent overcoming the friction of the bed and internal friction between spreading underflow and overlying water (Dankers, 2002).

2.5 Fluid Mud Wall Jet

Generally, from the impingement point, the horizontal propagation of fluid mud may initiate as a momentum-dominated wall jet. In this regime, momentum of the flowing fluid mud far outweighs its buoyancy (Papakonstantis and Christodoulou, 2010). It is subject to driving inertia force, retarding viscous force, and gravitational force that suppresses vertical mixing and enhance lateral propagation (Didden and Maxworthy, 1982). From dimensional analysis, the temporal variation of two-dimensional and radially axisymmetric propagation buoyant wall jets can be expressed as (Chen, 1980):

Two dimensional: $$x_N(t) = C_1 M^{1/4} t^{2/3}. \tag{2.3}$$

Radial: $$r_N(t) = C_2 M^{1/4} t^{1/2}. \tag{2.4}$$

Here, x_N and r_N are the front position of the jet with impingement point as the origin, t is time from its initiation at the impingement point, and C_1 and C_2 are empricial constant. As the jet spreads, the momentum of the jet reduces and the effect of buoyancy becomes more pronounced. When the buoyancy of the fluid mud outweighs its momentum, the fluid mud spreads as a radial gravity current. To the best of the author's knowledge, there has not been any experimental investigation to accurately determine the transition time scale from a radial jet to a gravity current. However, the transition is expected to be

within short duration (Papakonstantis and Christodoulou, 2010) which is in line with the finding of the experiments conducted in the present investigation (see Chapter 3). From the above discussion, it is expected that the momentum-dominated wall jet of the fluid mud is generally short-lived. Therefore, the radial propagation of the fluid mud from the impingement point will occur mostly as a gravity current for most of its propagation, which is the main focus of this dissertation. The next section presents a detailed discussion on the fluid mud gravity currents.

2.6 Fluid Mud Gravity Current

As is discussed in the previous section, fluid mud underflows propagate as a radial gravity current either after the wall jet regime or from the impingement point (when the wall jet is absent) in a particular discharge flow condition. The fluid mud gravity current is caused by the density difference between the dense fluid mud and less dense ambient water (Bonnecaze et al., 1995a). This radial gravity current generally can be approximated as a constant flux release gravity current until the end of the disposal operation since the source at the impingement point releases fluid mud at a constant rate, Q. However, when the disposal operation ends or is interrupted due to, for example, a mechanical breakdown, the propagation of the gravity current can be regarded as the fixed volume released case since more volume of fluid mud is not added from the source. Therefore fluid mud gravity currents from both constant flux and fixed volume releases are investigated in our study and the relevant literature is reviewed in this Section.

As noted earlier, the radial fluid mud gravity current in a typical open water pipeline disposal operation can be axisymmetric (for vertically downward discharge configuration) as well as radially asymmetric (for horizontal discharge configuration). However, to our knowledge, there has been only one experimental study (Papakonstantis and Christodoulou, 2010) that investigated the dynamics of a radial saline gravity current formed from a horizontal discharge configuration. Papakonstantis and Christodoulou found that the downstream propagation of gravity currents in this case is more pronounced than the upstream propagation. However, their investigation could not relate that effect with the source parameters, thus leaving this research area open for new investigation. Since a thorough understanding on the asymmetric radial gravity current generated from horizontal discharge is lacking at this point, the following discussion will mostly focus on axisymmetric radial gravity currents, which is also the focus of this dissertation.

The propagation rate and the extent of radially axisymmetric fluid mud gravity currents depend on a number of source parameters at the impingement point, such as: inflow rate Q, solid concentration and density of the propagation fluid mud, particle size distribution and density of the suspended sediment in the fluid mud, and the rheological properties of the fluid mud among others (Nichols et al., 1978; Teeter, 2000). In addition, the dynamics of the flowing axisymmetric fluid mud gravity current may depend on the bottom topography and hydrodynamic conditions in the ambient water (Nichols et al., 1978; Barnard, 1978). For example, the flow dynamics of a gravity current on a horizontal bottom would differ greatly from a gravity current on a sloping bottom (see

Bonnecaze and Lister, 1999; Huppert, 1982b and Van Kessel and Kranenburg, 1996). Besides, the hydrodynamics conditions such as the presence of waves or current in the ambient water would further complicate the flow of a radially propagation gravity current (see Hallworth et al., 1998; Huppert, 1998; Robinson et al., 2006 and Ng and Fu, 2002). This research is focused on the simplest case: horizontal bottom with no currents and waves and hence, the following discussions will be limited to that case.

There have been very few analytical, laboratory and field investigations which thoroughly investigate the behavior of fluid mud gravity currents generated in open water pipeline disposal operations. Laboratory and field studies had been carried out by Neal et al. (1978), Nicholes et al. (1978), and Thevenot et al. (1992) on the short and long term fate of discharged fluid mud in a typical open water pipeline disposal operation. Those studies mostly focused on the estimation of turbidity generation by fluid mud dispersion. Recently, Teeter (2002) conducted field experiments to evaluate his proposed model (PDFATE – Pipeline Disposal Fate model) for predicting dispersion in open water pipeline disposal operations. However, Teeter (2001) mainly focused on evaluating the numerical model with field data, rather than analyzing the propagation dynamics of fluid mud. Therefore, those limited investigations could not provide a thorough understanding on the dynamics of the fluid mud gravity currents generated in open water pipeline disposal operations and required information in many aspects is lacking. However, the subject of gravity currents is an active area of research for the last few decades (see Ungarish, 2009; Huppert, 2006; Kneller and Buckee, 2000; Meiburg and Kneller, 2010; Simpson, 1997; for review of the recent research on various forms of gravity currents).

There have been extensive experimental and theoretical studies on the propagation dynamics of different forms of gravity currents, especially with saline gravity currents (e.g. Huppert and Simpson, 1980; Rottman and Simposn, 1983; Huppert, 1982 and Didden and Maxworty, 1982) and non-cohesive particle-driven currents (e.g. Bonnecaze et al., 1993; Bonnecaze et al., 1995; and Gladstone et al., 1998). Evidently, fluid mud gravity currents are compositionally and rheologically different than the saline and non-cohesive particle-driven currents investigated in those studies. A fluid mud gravity current is a cohesive, fine-grained particle driven current, and the suspension has profound non-Newtonian behavior (see Section 2.2). Hence, the propagation dynamics are expected to be influenced by their composition and rheology. Despite the differences, many of the concepts, results, and conclusions of these prior investigations provide broad background for the analysis of the propagation dynamics of fluid mud gravity currents.

Most insights gained on gravity currents were from two-dimensional experimental studies (e.g. Huppert and Simpson, 1980; Rottman and Simposn, 1983; Huppert, 1982 and Didden and Maxworty, 1982; Bonnecaze et al., 1993; Bonnecaze et al., 1995; and Gladstone et al., 1998). The reason to choose two-dimensional experiments is the simplicity. Therefore, both radial and two-dimensional propagation of fluid mud gravity currents will be explored in this study. An in-depth discussion on fluid mud gravity currents on a horizontal bottom in calm ambient water is given next.

2.6.1 Anatomy of a Gravity Current

The three-dimensional flow structure of a typical gravity current can be divided into two main parts: frontal zone and body. The frontal zone of a propagating saline gravity current had been investigated in a number of previous studies (e.g. Simpson, 1969; Fleischmann et al., 1994; Haertel et al., 2000; and La Rocca et al., 2008). Fig. 2.3 shows a typical flow structure of the frontal zone of a gravity current. Those studies revealed that gravity currents advance forming characteristic frontal zones where there are a distinct dividing lines between the intruding current and the ambient, less dense fluid. The leading edge of the frontal zone has a foremost point or nose that is slightly raised above the bed. The overhanging nose is shown to be the direct result of the no-slip boundary condition at the bottom boundary (Simpson, 1997; Middleton, 1993; Parsons and Garcia, 1998). The interface of the frontal zone and the ambient fluid can be characterized by two-types of instabilities: billows (right above and behind the head of the current) and lobe and clefts (at the leading edge and right behind the nose) (Britter and Simpson, 1979; Simpson, 1987). Both types of instabilities are shown in Fig. 2.3. The lobes are the protruding regions of the flow and are separated by sharp cusps called clefts. The formation of the lobe and cleft at the leading edge is due to the gravitational instability caused by the overrunning of less dense ambient fluid by the dense gravity current (Simpson and Britter, 1979). Britter and Simpson (1978) and Parsons and Garcia (1998) in two experimental investigations found that the lobe-cleft instability is the direct result of the no-slip boundary condition and the elevated nose. Their experimental investigations, with an apparatus that allowed them to evaluate gravity currents without

no-slip condition, revealed that the elevated nose and the lobe-cleft instability disappeared; only billows were observed. As the current propagates, the clefts do not simply disappear but are absorbed in or absorb neighboring clefts; thus, all lobes are continually shrinking or swelling. Once a lobe reaches a maximum size, a new cleft forms within it (see Simpson, 1997).

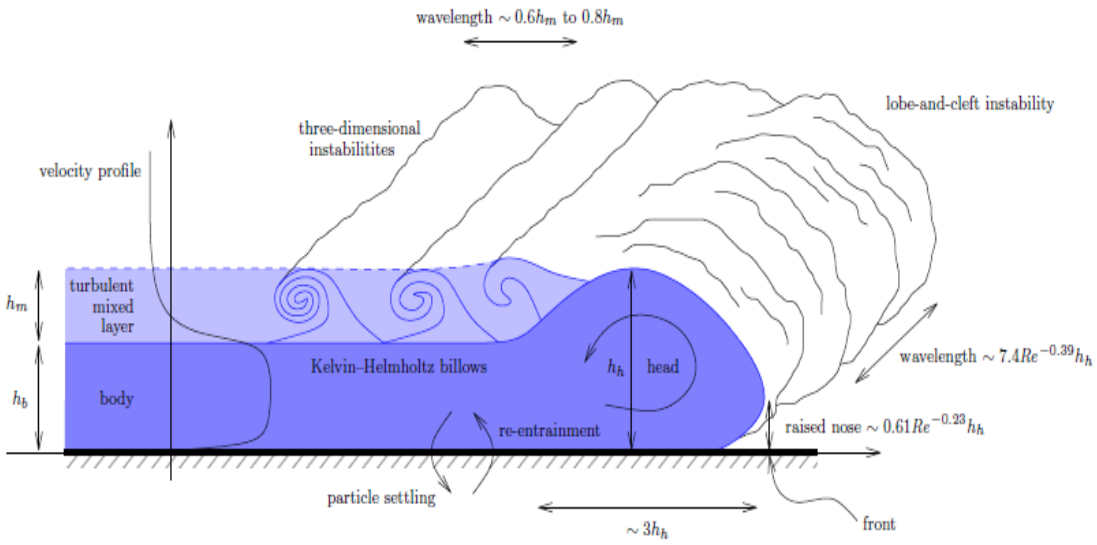

Figure 2.3. Typical flow structures of an inertial gravity current illustrating instabilities (courtesy of Anja Catharina Slim; copied from Slim, 2006).

As the lighter fluid is displaced by the current, a portion of the dense fluid is swept up behind the head of the current by the lighter fluid which causes the formation of billows at and behind the head of the current. Hence, the billows are created by velocity shear between the layers that counteract the stabilizing buoyancy forces (De Silva et al, 1996). The investigation of salt-water gravity currents by Simpson and Britter (1979) revealed that these billows were both qualitatively and quantitatively similar to the Kelvin-Helmholtz (K-H) instability of a shear layer separating two fluids of different

density. Cantero et al. (2007) applied direct numerical simulations (DNS) of high Reynolds number lock exchange experiments that allowed for an in-depth look at the creation of the K-H billows. They found that K-H billows form in the head, are shed as the current advances, and 'manifest as interfacial undulations'. As the current propagated, the amplitude of the undulations decreased with time indicating that the strength of the billows decrease with time. Further, it was observed that the rate of formation decreased with time as well. Please note that the above descriptions of K-H billows are for the gravity currents in inertia-buoyancy propagation phase. When the current reaches the viscous-buoyancy phase, the K-H billows are negligible (Cantero et al., 2008). The inertia-buoyancy and viscous-buoyancy propagation phases are discussed in Section 2.6.2 in detail.

Notably less research has been conducted on the body than the head. The body of the gravity current is best described as two separate regions: a dense underlying layer and a region of less dense fluid mixed out of the head of the current (Britter and Simpson, 1978; Simpson and Britter, 1979). Some researchers believe that this mixed layer is not a part of the gravity current and should be deemed as a "zone of clouded water" (see Kneller and Buckee, 2000 and references therein).

2.6.2 Propagation Dynamics of a Gravity Current

Extensive experimental investigations on different forms of gravity currents (e.g. Britter, 1979; Huppert and Simpson, 1980; Rottman and Simpson, 1983; Bonnecaze et al., 1993; Bonnecaze et al., 1995; and Gladstone et al., 1998) confirmed that their

propagation dynamics are governed by the inter-play among three key forces, namely: buoyancy, inertia and viscous forces. During the earlier propagation phase (henceforth, inertia-buoyancy phase) of a gravity current, the propagation dynamics is governed by the buoyancy and inertia forces. The propagation dynamics is governed by the buoyancy and viscous forces during the later propagation phase (henceforth, viscous-buoyancy phase). The propagation of a gravity current in the earlier inertia-buoyancy propagation phase is often referred to as inertial propagation, whereas in the later phase, it is often referred to as viscous propagation. In the next three sections, in-depth descriptions of the two propagation phases and their transitions, along with the description of different mathematical modeling approaches to approximate their propagation characteristics are provided.

2.6.2.1 Inertial Propagation of a Gravity Current

In the inertia-buoyancy phase, the propagation of a gravity current is governed by the driving buoyancy force that is balanced by the retarding inertia force, while viscous force is negligible compared to these two forces (Huppert and Simpson, 1980). However, experimental studies (e.g. Huppert and Simpson, 1980; Bonnecaze et al., 1993) revealed that the inertia-buoyancy phase of a gravity current generated from a fixed volume release is preceded by another phase called slumping phase. The slumping phase, occurring near the source of the dense fluid, is an adjustment phase in the formation of a fully developed gravity current with characteristic features like nose, head and body. The current front propagation speed in this phase is approximately constant (Rottman and Simpson, 1983; Gladstone et al., 1998; Huppert and Simpson, 1980). Though the flow in

slumping phase is mainly governed by the inertia - buoyancy balance, the overlying ambient fluid is very dynamic in this phase, affecting the propagation characteristics of the gravity current. After the slumping phase, the inertia-buoyancy phase commences. Here, the front propagation velocity is no longer constant, but decreases with distance. For a gravity current generated from a constant flux release, the inertia-buoyancy phase may be preceded by a wall jet phase (Didden and Maxworthy, 1982) rather than a slumping phase. The wall jet phase is generally not considered a phase of gravity current and hence, discussed separately in Section 2.5.

A significant number of studies have elucidated the quantitative prediction capability (see Von Karman, 1940; Benjamin, 1968; Hurzeler et al., 1996; Kirwan et al., 1986; Bowen et al., 1984; Kuenen, 1952; Mulder et al., 1998) for the propagation characteristics (e.g. front position, height, and volume fraction of particles) of different forms of inertial gravity currents. These studies utilized various mathematical modeling approaches characterized by different levels of complexities, ranging from dimensional analysis to solving complex Navier-Stokes equations. The simplest mathematical model is a simple one-equation model, such as the modified form of the Chezy-type equation (e.g. Kirwan et al., 1986; Bowen et al., 1984; Kuenen et al., 1952; and Mulder et al., 1998). This investigation focuses on three different widely used mathematical modeling approaches for inertial propagation of gravity currents, namely: force-balance, box model and one-layer shallow water modeling approaches. As far as modeling of the fluid mud gravity currents is concerned, this investigation mainly focuses on the models which provide analytical solutions. As will be described in detail in Chapter 5, these

mathematical modeling approaches admit a general form of expression for the propagation of an inertial gravity current:

Two dimensional: $$x_N = K_I \left[g_a' q \right]^{\frac{1}{3}} t^{\frac{\alpha+2}{3}}. \quad (2.5)$$

Radial: $$r_N = K_I (g_a' Q)^{\frac{1}{4}} t^{\frac{\alpha+2}{4}}. \quad (2.6)$$

Here, $g_a' = \frac{g(\rho_c - \rho_a)}{\rho_a}$ (g – acceleration due to gravity, ρ_c - density of the current and ρ_a - density of the ambient) is the reduced gravity in terms of ambient density; and q is a dimensional constant which is related to the volume of the fluid released. K_I is the proportionality constant function for inertial propagation that differs depending upon the modeling approaches. Detailed discussions on the proportionality constant functions for force-balance, box, and shallow water modeling approaches are given in Chapter 5. In Eqs. (2.5) and (2.6), α is a constant that represents the type of released fluid volume source. The cases of $\alpha = 0$ and $\alpha = 1$ represent gravity currents originating from fixed volume and constant flux release of fluid, respectively.

A force-balance expression is usually obtained by equating the expression of two dominant forces in the respective flow regimes. Therefore, for inertial propagation of gravity currents, it can be obtained by equating the order of magnitude of the buoyancy and inertia forces. However, since it is an order-of-magnitude relationship, a pre-

multiplicative constant exists in the resulting expression, and this multiplicative constant need to be determined experimentally.

At the next level of complexity is the box model approach where the current is considered to evolve in a series of boxes of equal area which have uniform properties at any instant of time (Huppert, 1998). Other key assumptions of this approach are that there is no horizontal variation of the flow properties (e.g. current height and volume fraction of particles) within the current, and entrainment of ambient fluid by current head is negligible (Harris et al., 2001). One of the major advantages of this approach is that it leads to closed form analytical solution (Huppert, 1998). The box model approach has been one of the most widely used modeling approaches for predicting the inertial propagation of gravity currents. Huppert and Simpson (1980) first used the box model approach for inertial propagation compositional gravity current. It was later extended by Dade et al. (1995a; 1995b) for inertial propagation of particle-driven currents. Despite having a number of simplifying assumptions, a number of studies (e.g. Huppert and Simpson, 1980; Dade et al., 1995a, 1995b; Gladstone et al., 1998; Hogg et al., 1999; and Huppert, 1998) have shown that the predictions of the box model solution were in general in good agreement with the experimental observations of gravity currents.

Shallow water models are the most complex among the three modeling approaches. In this approach, Navier-Stokes equations are solved in the depth-average form. The basic assumption in this approach is that no significant vertical variations in the properties of the current exist so that the pressure field is purely hydrostatic. This

assumption results in one mean value for each state variable at each point downstream (Kneller, et al., 2000). Therefore, one can find horizontal variations of properties within the current such as velocities and volume concentrations using shallow water model approach. In this approach, the flow dynamics of gravity currents can be approximated by two methods: one layer models and two layer models. In one layer models, the dynamics of gravity currents is estimated by neglecting the dynamics of the overlying water, whereas two-layer models incorporate the dynamics of the overlying fluid layer. Two-layer shallow water models are expected to provide more accurate predictions than those of one-layer models, especially in the slumping phase (for fixed volume release) when the overlying water is dynamic. The disadvantage of two-layer models is that they require numerical solutions as there are no closed form analytical solutions for them. A gravity current with a deep ambient fluid is usually formulated by a one-layer shallow water while a two-layer model is preferred for gravity currents with shallow ambient (Meiburg, et al., 2009). The term 'ambient' is used in this manuscript extensively which refers to the depth of the ambient fluid in relation to the gravity current height. Therefore, a current in shallow ambient implies that the ratio of the current height and the depth of the ambient fluid is high while, for deep ambient, the ratio is low. There have been attempts to predict the flow dynamics of a gravity current in a shallow ambient by a one-layer model such as by Hogg et al. (1999) and Harris et al. (2001). Those studies showed that the predictions of one-layer models are in good agreement with the experimental observations. To model a gravity current governed by an inertia-buoyancy balance, Rottman et al. (1983) proposed a shallow water model for a compositional gravity current, which is later

extended for particle-driven currents of non-cohesive sediments by Bonnecaze et al. (1993; 1995; 1999) and Parker et al. (1986). A one-layer shallow water model for compositional gravity currents admits a similarity solution (Bonnecaze, et al., 1993). However, there has not been any similarity solution even for one-layer shallow water models for particle-driven gravity currents. Only recently, Hogg et al. (2000) and Harris et al. (2001) derived an asymptotic solution of one-layer shallow water models for particle-driven gravity currents which somewhat obviated the necessity to take numerical approach to analyze the propagation of particle-driven currents.

In addition to these mathematical modeling approaches two-dimensional and three-dimensional high-resolution numerical simulations of gravity currents (e.g., Blanchette et al., 2006; Cantero et al., 2008; Haertel et al., 2000; Necker et al., 2002) have been attempted. In terms of modeling, the goal of this study is to apply the described mathematical modeling approaches (force-balance, box, shallow water) which admit analytical solutions. Hence, complex numerical simulations are out of the scope of this study and will not be explored further. In Chapter 5 the expressions for the selected mathematical models are provided and then their predictive capabilities are evaluated using fluid mud gravity current experimental observations.

2.6.2.2 Transition between Inertial and Viscous Propagation

As the gravity current propagates in the inertia-buoyancy propagation phase, it starts experiencing an increasing viscous force. After some time, depending on the rheological properties of the current fluid, the viscous force may become comparable to

the inertia force. As the viscous effect becomes more and more pronounced after further propagation, the gravity current may transition into the viscous-buoyancy propagation phase where the propagation is mainly governed by the driving buoyancy force and the retarding viscous force, with negligible effects due to the inertia force. For the fixed volume case, if viscous effects exhibit greater importance before the slumping phase is completed, the current may not even exhibit the self-similar phase of the inertia-buoyancy phase, but rather directly transition into the viscous-buoyancy phase (Huppert and Simpson, 1980). Such a transition was observed in our experiments, the results of which are presented later in this dissertation. The rheological properties and the inflow rate of the fluid mud at the source will determine when the fluid mud gravity current makes the transition from the inertial propagation to the viscous propagation. Determining the transition time between the two propagation phases is of importance for modeling the propagation of a gravity current because two different models are required to model its flow dynamics in these two distinct phases. The inertia-buoyancy propagation phase of a gravity current is usually modeled by predictive models which are constructed with the assumption that the current is fully governed by an inertia-buoyancy balance with negligible viscous effects. On the other hand, the predictive models of the viscous-buoyancy phase of a gravity current are based on the assumption of a viscous-buoyancy balance with negligible inertia effects. Perhaps one of the most overlooked characteristics of gravity currents, albeit being an active research area in the last few decades, is how currents make the transition from the inertia-buoyancy to viscous-buoyancy phase. The reason for this is most of the experimental gravity currents

generated in laboratory studies were of Newtonian fluids, mainly of saline solution or non-cohesive particle suspensions (see Bonnecaze et al., 1993; 1995; Dade and Huppert, 1995; Gladstone et al., 1998), that did not show pronounced viscous effects in the limited propagation distance of the experimental set-ups. Huppert and Simpson (1980) studied the transition in their saline gravity current experiments and provided an expression for the transition time based on their experimental data. Later, Bonnecaze et al. (1993) derived critical Reynolds number criterion for the transition based on the transition time expression of Huppert and Simpson (1980). Huppert (1982) derived the transition time expressions for two-dimensional and radial gravity currents from order-of-magnitude relationships. All of these expressions/criteria are for Newtonian gravity currents. To the author's knowledge, there is no experimental study which investigated the transition of a non-Newtonian gravity current. Hence, a major focus of this investigation is dedicated to studying the transition from inertial to viscous propagation. In this effort, transition time expressions for the two-dimensional and radial propagation of non-Newtonian gravity currents are derived and their predictions are compared with the transition time observations from fluid mud gravity current experiments, which are described in detail in Chapter 4. Please note that Di Federico et al. (2006) attempted to extend the order-of-magnitude expression of transition time of Huppert (1982) for non-Newtonian gravity currents. However, the final expression provided in their Appendix does not conform to our derivations presented in Chapter 4.

2.6.2.3 Viscous Propagation of a Gravity Current

When the gravity current is in the viscous-buoyancy phase, its propagation dynamics is governed by the driving buoyancy force which is balanced by the retarding viscous force (Huppert and Simpson, 1980). As discussed in Section 2.6.2.2, there have been various theoretical models and extensive laboratory experiments devoted to inertial gravity currents over the last few decades. Conversely, the viscous propagation of gravity currents has received less attention, and most of the literature on viscous propagation has been for the Newtonian currents. The theoretical modeling of viscous propagation of a non-Newtonian gravity current is generally more complex than its Newtonian counterparts, as the non-linear constitutive equation of such currents leads to highly non-linear governing equations which must often be solved numerically (Pascal, 2000). Like inertial propagation, the same three modeling approaches are chosen for viscous propagation of fluid mud gravity current. As it will be described in detail in Chapter 6, these three mathematical modeling approaches also admit a general form of expression for the propagation of a viscous gravity current:

Two dimensional:
$$x_N = K_v q^{\frac{2+n}{2n+3}} \left(\frac{\rho_c g_c'}{m} \right)^{\frac{1}{2n+3}} t^{\frac{n+\alpha(n+2)}{2n+3}}. \qquad (2.7)$$

Radial:
$$r_N = K_v Q^{\frac{2+n}{3n+5}} \left(\frac{\rho_c g_c'}{m} \right)^{\frac{1}{3n+5}} t^{\frac{n+\alpha(n+2)}{3n+5}}. \qquad (2.8)$$

Here, $g_c' = \frac{g(\rho_c - \rho_a)}{\rho_c}$ is the reduced gravity in terms of current density, and K_v is the proportionality constant function for viscous propagation that differs depending upon the modeling approaches and are functions of α and n. Detailed discussions on the proportionality constant functions for force-balance, box, and shallow water modeling approaches are given in Chapter 6. In Section 2.6.2.1, these three different modeling approaches (force-balance, box, shallow water) were discussed for the inertia-buoyancy phase of propagation. Similar theoretical treatments of viscous Newtonian and non-Newtonian gravity current propagations are given below.

The force-balance expression for the viscous-buoyancy balance can be obtained by equating the order of magnitude expressions of buoyancy force and viscous force expressions. Didden and Maxworthy (1982) derived such expressions to model the viscous propagation of two-dimensional and radial axisymmetric Newtonian gravity currents. Predictions of their expressions showed good agreement with their experimental observations for the case of constant flux release. Viscous propagation of two-dimensional forms of such currents for variable inflow rates were then investigated experimentally by Maxworthy (1983). The first attempt to predict the viscous propagation of non-Newtonian gravity currents by a force-balance expression was recently by Chowdhury and Testik (2011). The derivation of this force-balance expression and comparisons of its predictions with viscous propagation of experimental observations of fluid mud gravity currents are detailed in Chapter 5.

Despite its widespread use to predict the inertial propagation of gravity currents (e.g. Huppert and Simpson, 1980; Dade et al., 1995, 1995a; Gladstone et al., 1998, 2000 and Hogg et al., 1999), the box model approach has not been implemented for predicting the propagation of viscous gravity currents. In his recent monograph, Ungarish (2009) described a box model solution for the viscous propagation of Newtonian gravity currents which has not yet been tested experimentally. To the best of the author's knowledge, there has not been any attempt to implement the box model approach on viscous propagation of non-Newtonian gravity currents. In this study, a box model solution for non-Newtonian gravity currents is proposed and the solution is evaluated by the experimental observations of fluid mud gravity currents.

The viscous counterpart of the shallow water modeling approach is the lubrication theory. The main assumption in lubrication theory for viscous gravity current is that the currents spread as a thin layer which, in turn, implies the velocity profile of such a current is parabolic (Huppert, 2004). Hoult (1972), studying the viscous propagation of oil along the free surface of water, obtained a similarity solution for the two-dimensional viscous propagation of a surface gravity current. Then, Huppert (1982) obtained a self-similarity solution for the viscous propagation of bottom gravity currents along a horizontal surface for the case of fixed volume release. Subsequently, Lister and Kerr (1989) investigated the propagation of two-dimensional and axisymmetric viscous gravity currents at a fluid interface and obtained a similarity solution for the governing one-layer shallow water model equations. Recently, Di Federico et al. (2006), Gratton and Minotti (1999) and Pascal (2000) in three separate investigations used the lubrication theory approach with

associated simplifying assumptions for estimating viscous propagation characteristics of non-Newtonian gravity currents. In these investigations they provided analytic expressions that required numerical solutions, except for some limiting cases in which closed form analytic solutions are available (for example, fixed-volume release; see Pascal, 2000; Di Federico et al., 2006). In Chapter 5, the predictions of the shallow water model by Di Federico et al. (2006) are compared with our experimental observations of fluid mud gravity currents.

A comparison can be drawn among the three modeling approaches. The Force-balance expression is the simplest among the three models. However, it has a proportionality constant which needs to be determined experimentally. The box model approach provides a closed-form analytic solution and it does not have any pre-multiplicative constant. However, the box model solutions cannot describe all the characteristics features of gravity currents (e.g. lacks a description of the horizontal variation of the current height). Therefore, at any instant of time, the current height along the current is assumed to be equal to the current height at the head. The shallow water/lubrication thoery model is the most accurate among the three and unlike the box model, it can provide the horizontal variation of gravity current characteristics. However, it provides analytic expressions that require numerical solutions, except for some limiting cases in which closed form analytic solutions are available (for example, fixed-volume release; see Pascal, 2000; Di Federico et al., 2006a; 2006b).

CHAPTER THREE

EXPERIMENTAL SETUP, METHODOLOGY, AND MEASUREMENT TECHNIQUES

In order to investigate the propagation dynamics of fluid mud underflows, two experimental facilities – rectangular flume and square pool - with two different discharge configurations were used. The rectangular flume was used to conduct two series of experiments: one with constant volume release and the other with constant flux release of fluid mud. Those experiments were performed to study two-dimensional propagation of fluid mud underflows. In the square pool, fluid mud with different concentrations was discharged from a submerged vertical pipe, which generated radially axisymmetric fluid mud underflows. The experimental setups for the conducted experiments are described in section 3.1. Experimental procedures for each type of experiment and the apparatus used to measure the flow properties are presented in Section 3.2.

3.1 Experimental Set-ups and Release Configurations

In this section, the experimental facilities are described in detail.

3.1.1 Rectangular Flume

A rectangular Plexiglas flume with a lock-gate was used to conduct constant volume release experiments. The flume was designed and constructed such that with simple modifications, it was also used to conduct constant flux release experiments. The details of both set-ups are presented below.

3.1.1.1 Constant Volume Release

The rectangular flume consists of two sections: a small reservoir section (0.245 m – length, 0.25 m – width, 0.5 m – height) filled with the prepared fluid mud suspension at one end (henceforth, upstream end) of the tank; and the experimental section that is filled with the ambient fluid (i.e., tap water) from the reservoir to the other end (henceforth, downstream end) of the tank. A simplified schematic of the setup is shown in Fig. 3.1.

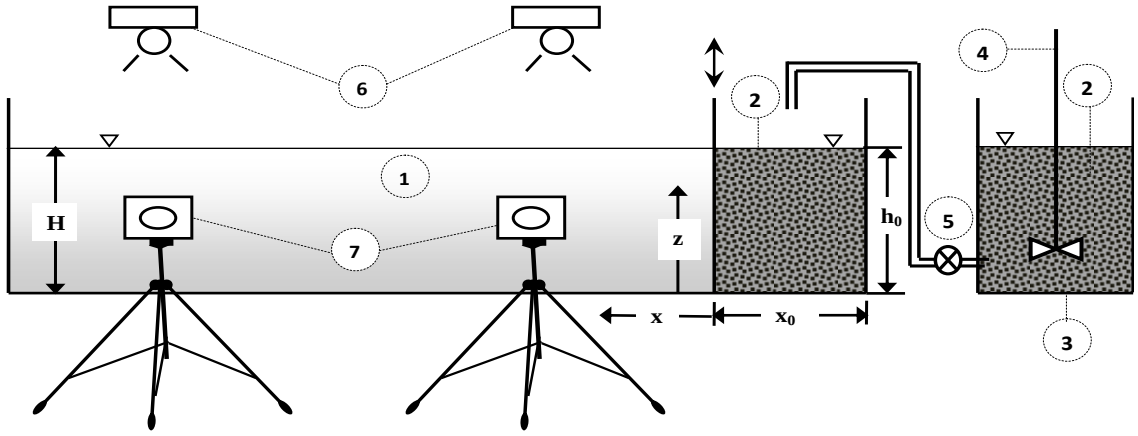

Figure 3.1. Schematic of the 2-D constant volume release experimental setup: 1- experimental section filled with tap water, 2- fluid mud suspension reservoir with fluid mud suspension behind the lock-gate, 3- mixing tank, 4- mixer, 5- pump and the piping, 6- lights, and 7- video cameras. Symbols: h_0 – fluid mud suspension depth before release; x_0 – length of the lock section; x – horizontal coordinate with the origin at the lock gate; z – vertical coordinate with the origin at the tank bottom.

A removable vertical aluminum plate located at a distance x_0 = 24.5 cm from one end of the flume serves as the lock-gate. To avoid exchange of fluids between the two reservoirs (i.e., experimental section filled with tap water and fluid mud reservoirs) before the experiments commence, the gate was sealed with petroleum jelly around its edge. The tank was marked by vertical reference lines every 10 cm from the lock-gate to

the end of the flume. A mixing tank located next to the lock section was used to prepare the fluid mud suspension. A typical experiment in this setup was as follows. First, the experimental section was filled with tap water to a height of h_0. Then, just before the experiment commenced the fluid-mud reservoir was filled to the same level as the water reservoir. For each experiment, fluid mud underflow was generated by the instantaneous release of the dense fluid mud by lifting the lock-gate. As soon as the lock-gate was lifted, a two-dimensional fluid mud underflow formed and began propagating in the 2-D experimental tank. Figure 3.2 presents a photograph of this fluid mud underflow propagating over a horizontal bottom. A total of 12 constant-volume release experiments with different concentrations of fluid mud suspensions were carried out in this set-up. The initial parameters for these experiments are tabulated in Table 3.1.

Figure 3.2. Propagation of the constant-volume released fluid mud underflow in Exp. # 5 after 9 seconds of releasing the fluid mud suspension in a rectangular flume. The current front position, x_N, is at 102 cm from the lock-gate at the shown instant.

Table 3.1. Experimental conditions for the two-dimensional constant volume release experiments in the rectangular flume. Parameter values are given for the prepared fluid mud suspensions before the release.

Exp. # [a]	C_m (g/l) [b]	C_v (%) [c]	ρ_c (g/cm^3) [d]	h_0 (cm) [e]	Rheological Properties	
					m (Pa s^n) [f]	n [g]
1	25	1.0	1.015	15	----	----
2	50	1.9	1.03	15	0.0016	1.00
3	75	2.8	1.045	15	0.0340	0.52
4	100	3.7	1.06	15	0.0880	0.41
5	150	5.4	1.09	15	0.3200	0.30
6	200	7	1.12	15	0.7800	0.24
7	250	8.7	1.14	15	1.6500	0.19
8	300	10.2	1.166	15	2.9000	0.17
9	350	11.8	1.19	15	4.6600	0.15
10	400	13.2	1.214	15	7.0000	0.14
11	450	14.7	1.24	15	10.000	0.124
12	350	11.8	1.19	10	4.6600	0.15

[a] Exp. # - Experiment number
[b] C_m - Sediment mass/volume of water
[c] C_v - Volume Concentration
[d] ρ_c - Density of the suspension
[e] h_0 - Lock height
[f] m – consistency index
[g] n – flow behavior index

3.1.1.2 Constant Flux Release

The two-dimensional experiments from constant flux release of fluid mud were conducted in the same horizontal, rectangular Plexiglas flume used in the constant volume release experiments described in Section 3.1.1.1. However the experimental set-up was modified for a constant flux of dense fluid mud release into the ambient water. A simplified schematic of the modified experimental setup is given in Fig. 3.3.

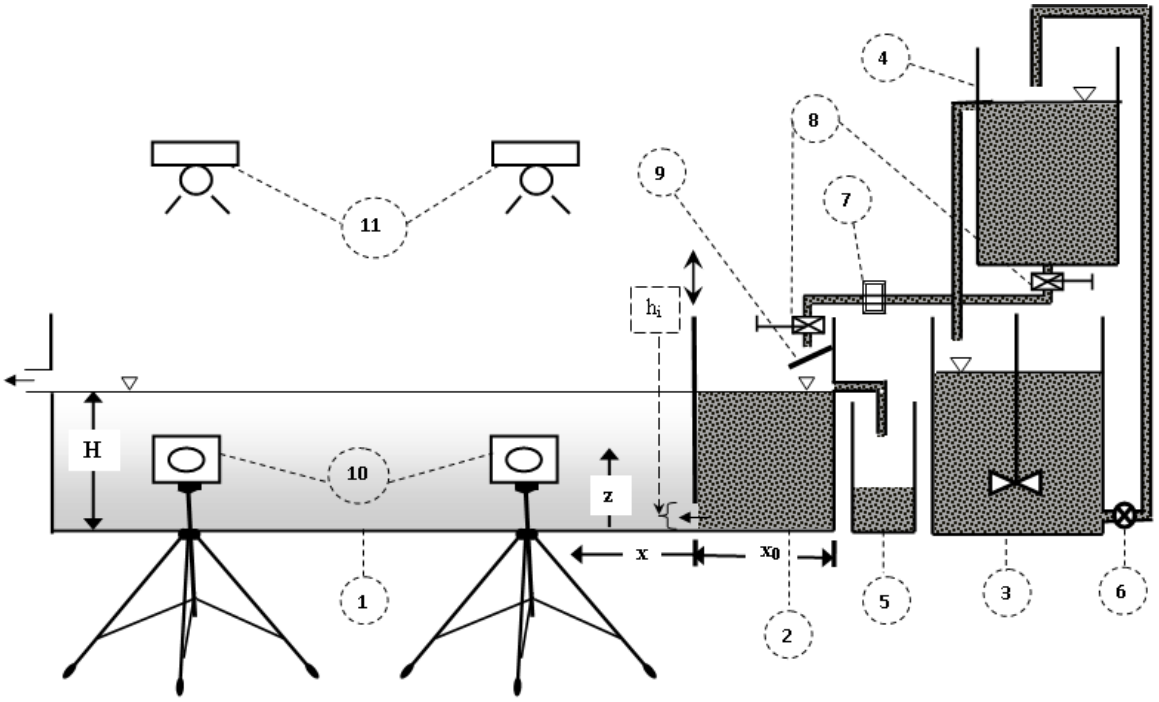

Figure 3.3. Schematic of the 2-D constant flux release experimental setup: 1- experimnental section with tapwater, 2- reservoir with fluid mud suspension, 3- mixing tank, 4- overhead tank, 5- fluid mud spilling tank, 6- pump, 7- electromagnetic flowmeter, 8- adjustable flowrate control valves, 9- splattering plate, 10- video cameras, 11- lights. Symbols: h_i – inlet height ; x_0 – length of the reservoir; x – horizontal coordinate with the origin at the inlet; z – vertical coordinate with the origin at the tank bottom, and H- height of fluids in the reservoir and the experimental section of the tank.

In this setup, two vertical aluminum plates placed adjacent to each other separated the reservoir section from the experimental section. One of the two plates that span the entire width of the tank is fixed with an opening of height, h_i, from the bottom of the tank. The opening under this fixed plate serves as an inlet through which the dense fluid mud is released from the reservoir into the experimental section. The other plate can be moved vertically to the desired height from the bottom. Before an experiment commences, this adjustable plate is extended to the bottom of the tank and is sealed with petroleum jelly around the edge to avoid exchange of fluids between the reservoir and the experimental section. The experimental section is marked by vertical lines every 10 cm

from the inlet position to the downstream end. The downstream wall of the experimental section is cut down to a height of h_r, and prior to each experiment this section is filled with tap water to a height of h_r. Thus, any added volume of fluid mud causes the same volume of water to spill from the experimental section, with the total volume of fluid in the experimental section remains constant throughout an experiment.

The experimental setup also includes a mixing tank to form homogeneous fluid mud mixtures and an overhead tank that provides a constant head of fluid mud to the reservoir of the experimental tank. Fluid mud is first pumped up from the mixing tank approximately 3 m to the overhead tank; the fluid mud overflow is then returned to the mixing tank via a side pipe attached to the overhead tank (see Fig. 3.3). The fluid mud is then discharged from the overhead tank to the reservoir of the flume through a 2.54 cm diameter pipe. To control and measure the discharge flow rate, two valves and an electromagnetic flowmeter (see the description in section 3.2.2) are attached to this discharge pipe. Throughout each experiment, the discharge volume flow rate is acquired at 1 Hz using a computer. The end of the discharge pipe is directed onto a splattering plate to ensure that the discharged fluid mud does not impart any energy onto the fluid mud suspension in the reservoir.

To provide a constant flux release of fluid mud from the reservoir, the fluid mud height in the reservoir was kept constant. Therefore, the excess fluid mud discharged into the reservoir was drained from the reservoir using three circular openings of 1.27 cm diameter at the height of h_r above the bottom of the experimental tank. The drained fluid

mud is collected in a separate container and the collected fluid volume is measured after each experiment. Because the volume flow rate of the drained fluid mud was much smaller than the inlet flow rate (approximately less than 2% of the inlet flow rate), the flowmeter measurements were not corrected by subtracting the average drain rate from the flowmeter readings. Once the constant head of fluid mud in the reservoir was ensured, the adjustable lock-gate was lifted and the dense fluid mud advanced through the inlet into the experimental section forming an underflow flowing under the ambient water.

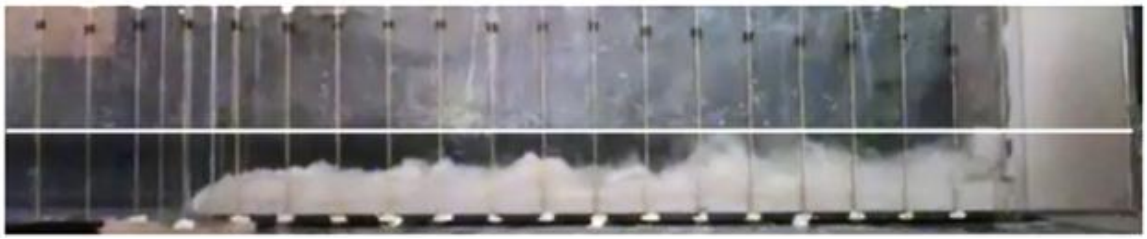

Figure 3.4. A photograph showing the propagation of a constant flux released fluid mud underflow in the rectangular flume. Horizontal white line indicates the water and fluid mud level in the experimental section and the reservoir of the tank, respectively. The blurriness in the reservoir is caused by the splashes of the fluid mud from the splattering plate. Experimental conditions: Exp. #18, t = 14s, x_N = 158 cm.

A photograph of a typical fluid mud underflow in this set-up is shown in Fig. 3.4. A total of 12 experiments (Exps. #13-24) with different concentrations of fluid mud suspensions were carried out in this set-up are tabulated in Table 3.2.

Table 3.2. Experimental conditions for the two-dimensional constant flux release experiments in the rectangular flume. Parameter values are given for the fluid mud mixtures in the reservoir.

Exp. # [a]	C_v (%) [b]	ρ_c (g/cm^3) [c]	q_0 (cm^2/s) [d]	h_i (cm) [e]	h_r (cm) [f]	Rheological Properties	
						m (Pa s^n) [g]	n [h]
13	0.4	1.006	7	3	15	---	---
14	4.43	1.072	10	3	21	0.12	0.33
15	5.67	1.092	25	5	21	0.29	0.28
16	8.38	1.136	35	5	21	1.102	0.20
17	6.40	1.104	24.00	3	15	0.420	0.249
18	6.90	1.111	24.00	3	15	0.550	0.24
19	9.30	1.151	25.00	3	15	1.524	0.187
20	10	1.162	21	3	21	1.963	0.177
21	10.2	1.166	30	5	21	2.1	0.174
22	10.75	1.174	24.00	3	15	2.490	0.168
23	10.8	1176	22.5	3	21	2.55	0.167
24	12.23	1.198	20	3	15	3.854	0.152

[a] Exp. # - Experiment number
[b] C_v - Volume concentration of the fluid mud mixture
[c] ρ_c - Density of the fluid mud
[e] q_0 – Released fluid mud volume flow rate per unit width of the tank at the inlet
[e] h_i - Inlet height
[e] h_r – Depth of fluid mud in the reservoir
[f] m – Consistency index
[g] n – Flow behavior index

3.1.3 Square Pool

The radial experiments were conducted by discharging a constant flux of fluid mud with varying concentrations into an experimental pool (3.6 m - length, 3.6 m - width, 1 m – height), three sides of which are made of Plexiglas for visualization purposes. The bottom floor of the pool was marked by reference concentric circles in 20

cm radial increments from its center. A schematic of the experimental setup and picture of the set-up are shown in Figs. 3.5.

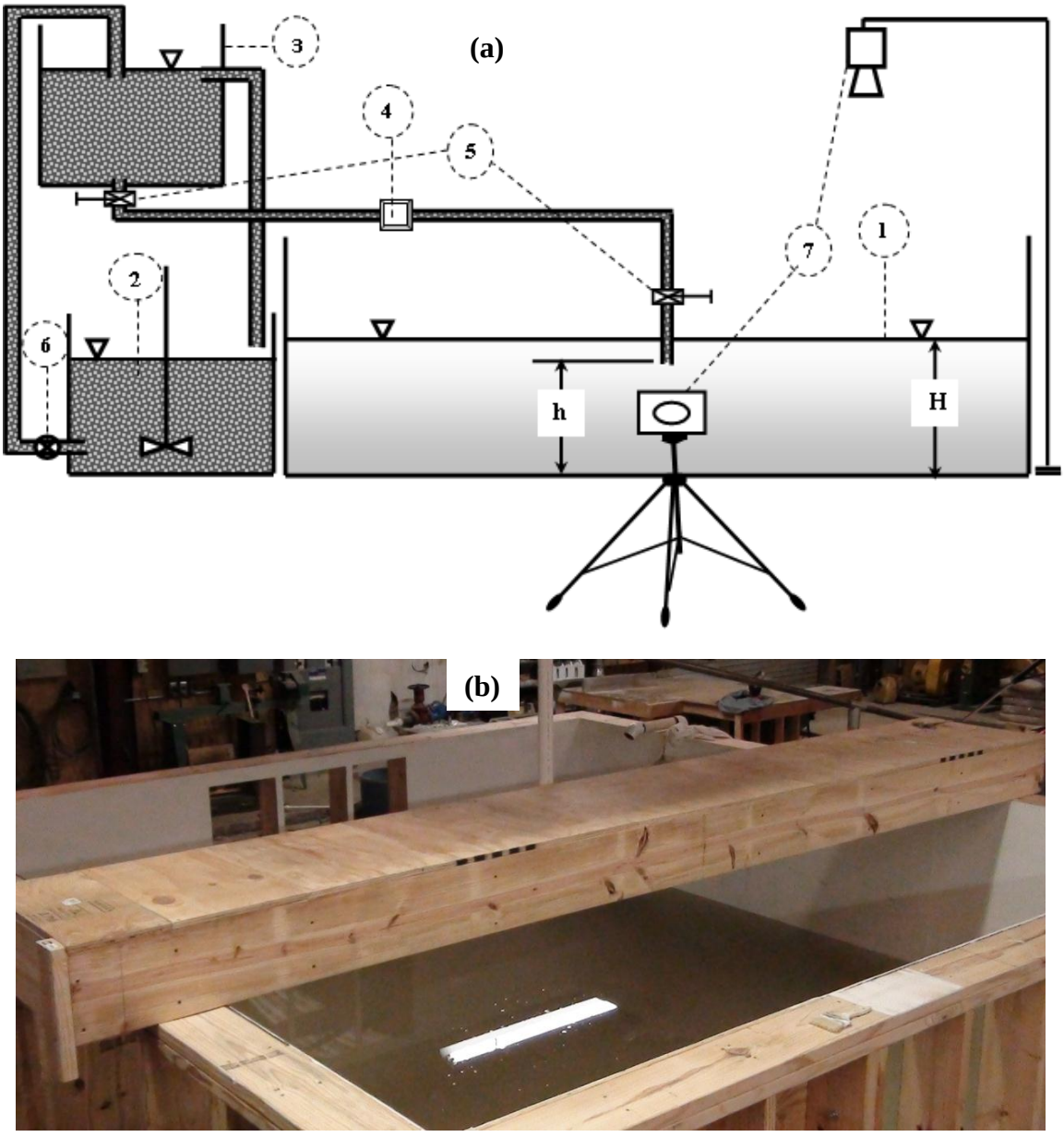

Figure 3.5. Experimental square pool. a) Schematic of the set-up for constant-flux release : 1 - pool with tap water, 2 - mixing tank with fluid mud suspension, 3 –overhead tank with constant head of fluid mud suspension, 4 - electromagnetic flowmeter, 5 - adjustable valves, 6 – pump, and 7 - video cameras, and b) Picture of the pool.

The experimental setup also includes a mixing tank placed beside the pool to form homogeneous fluid mud mixtures. An overhead tank is placed approximately H_o=3.2 m above the bottom of the pool to provide a constant head of fluid mud. Fluid mud was first pumped up from the mixing tank to the overhead tank; the fluid mud overflow is then returned to the mixing tank via a side pipe attached to the overhead tank which ensures a constant head tank of fluid mud suspensions in the overhead tank (see Fig. 3.5).

Before each experiment, the pool was filled with tap water to a depth of H. The delivery of the fluid mud was then introduced from the overhead tank at the center of the pool through a 2.54 cm diameter discharge pipe. The discharged pipe was aligned perpendicular to the center of the bottom floor and positioned h_d = 40 cm (for first series of experiments) or h_d = 10.6 cm (for the second series of experiments) below the free surface of the water in the pool. To control and measure the discharge flow rate, two valves and an electromagnetic flowmeter were attached to the discharge pipeline. The discharge flow rate, water depth and the position of the discharge pipe were chosen from an appropriate scaling analysis of typical pipeline disposal field conditions with Froude number similarity and a fully turbulent discharge condition. A total of 11 constant flux release experiments (Exps. #25-35) were conducted using this setup, the initial conditions of which are tabulated in Table 3.3. The outcomes of those experiments are radial axisymmetric fluid mud underflows. A photograph of a typical radial fluid mud underflow in this set-up can be seen in Fig. 3.6.

Table 3.3. Experimental conditions for the radial axisymmetric constant-flux release fluid mud underflows in the square pool. All the values except h_d/l_M is at the discharge port.

Exp. # [a]	C_v **(%)** [b]	ρ_m **(g/cm^3)** [c]	Q_0 **(cm^3/s)** [d]	h_d **(cm)** [e]	H **(cm)** [f]	Fr_0 [g]	h_d/l_M [h]
25	2.60	1.042	320	40	60	6.2	2.7
26	4.13	1.067	240	40	60	3.7	4.55
27	5.23	1.086	575	40	60	7.8	2.15
28	5.73	1.093	250	40	60	3.2	5.16
29	6.4	1.105	220	10.6	20	2.7	6.22
30	8.3	1.135	185	40	60	2.0	8.40
31	9.8	1.158	640	40	60	6.4	2.62
32	10.23	1.166	110	10.6	20	1.1	15.66
33	11.52	1.186	770	40	60	7.1	2.37
34	9.2	1.147	30	10.6	20	0.3	53.6
35	6.5	1.107	40	10.6	20	0.5	35.2

[a] Exp. # - Experiment number
[b] C_v - Volume concentration of the fluid mud suspension
[c] ρ_m - Density of the discharged fluid mud suspension
[d] Q_0 – Discharge Flowrate
[e] h_d – Discharge height from the bottom
[f] H – Water depth
[g] Fr_0 – Discharge Froude number [$Fr_0 = u_0 \big/ \sqrt{g_0' d_0}$]
[h] h_d/l_M – Dimensionless distance of the bottom from the discharge port.

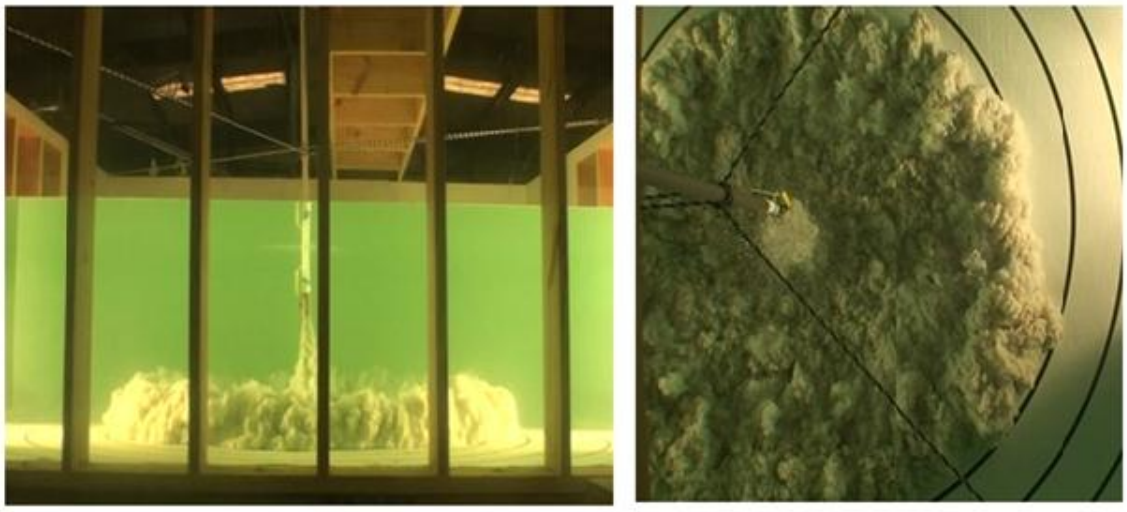

Figure 3.6. Photographs showing the propagation of a typical axisymmetric fluid mud underflows from side (left picture) and from top (right picture). Experimental conditions: Exp. #33, t = 11.75 s, r_N = 77 cm.

3.2 Experimental Methodology and Measurement Techniques

This section describes the instruments and methodologies used in the experiments.

3.2.1 Density and Rheology Measurement

The main constituent of all of the experiments was a homogeneous fluid mud mixture/suspension which, in turn, forms the fluid mud underflows in the respective experiments. Fluid mud was prepared by vigorously mixing cohesive Kaolinite clay particles with tap water in a mixing tank. The mean particle size and the average density of the clay particles are 0.7 μm and 2620 kg m^{-3}, respectively. Before each experiment, the density of the prepared fluid mud mixture was measured by an Anton Paar DMA-35 densitometer with an accuracy of 0.001 g cm^{-3}. The densities of the fluid mud

suspensions prepared for each experiment are listed in respective Tables (Tables 3.1, 3.2 and 3.3)

In addition, the rheological properties of the prepared fluid mud suspensions were obtained using a BrookField LVDVII Pro^{+} viscometer with an enhanced UL (Ultra Low) adapter. For the purpose of clarity, Figure 3.7a shows typical apparent viscosity (μ_a) vs. shear rate, and Fig. 3.7b shows typical shear stress vs. shear rate measurements for fluid mud suspensions of with different concentrations. It is evident from Fig. 3.7a,b that the fluid mud suspensions exhibit shear-thinning non-Newtonian behavior as the viscosity decreases with shear rate. Similar non-Newtonian behavior was observed for all the experimental suspensions, except for the suspensions with low concentration values ($C_v \leq 2\%$) that exhibit Newtonian behavior. Viscosity measurements are not available for the suspension used in Exp. #1 (C_v = 1%) in Table 3.1 and Exp. #13 (C_v = 0.4%) in Table 3.1 due to the limitations of the viscometer. However, since the suspension used in Exp. #2 of Table 3.1 (with higher concentration value than the suspension used in Exp. #1 and 13) exhibits Newtonian behavior, it is evident that the suspensions used in Exp. #1 and 13 also exhibit Newtonian behavior.

The prepared fluid mud suspensions are observed to be shear thinning (see Fig. 3.7a) which can be modeled by the Ostwald power-law constitutive equation presented in Chapter 2 (Eq. 2.2). Therefore, a power-law constitutive equation is fitted to the shear stress vs. shear rate measurements (see solid lines in Fig. 3.7b) to determine the flow behavior index, *n* and consistency index, *m* for the different prepared suspensions. Fitted

values of these rheological constants (symbols) for these suspensions are shown in Fig 3.7 c and d. Here, the *m* value increases and the *n* value decreases with the volume concentration increase. Correlation of the power-law constants (*m* and *n*) to the volume concentration [$C_v = V_s/(V_s + V_w)$, where V_s and V_w are the volumes of suspended sediment and water in the prepared suspension, respectively] for fluid mud suspensions was reported by Ng and Mei (1994). Following the same procedure as Ng and Mei (1994), after measuring the rheological properties of the fluid mud suspensions with different concentrations, the calculated *m* and *n* values of suspensions were correlated to the C_v values of suspensions. This enabled us to predict the m and n values of the suspensions within our range of experimental conditions, minimizing the effects of the measurement range limitations of our viscometer. The empirical parameterizations for *m* and *n* values as a function of volume concentration for the prepared fluid mud suspensions were developed by fitting curves (see solid lines in Fig. 3.7 c,d). Please note that estimation of rheological parameters is difficult due to experimental geometric restrictions, settling of particles, wall slip, edge, and particle segregation effects, a view also shared by Mcanally et al. (2007) and Barnes et al. (1989). Furthermore, correlating power-law constants with the concentration of the fluid mud requires curve fitting the experimental data twice (see Fig. 3.7 c and d) which may also pose additional accuracy limitations. Two empirical parameterizations for *m* and *n* values were developed, one during the fixed volume 2D experiments and another during the constant flux 2D experiments.

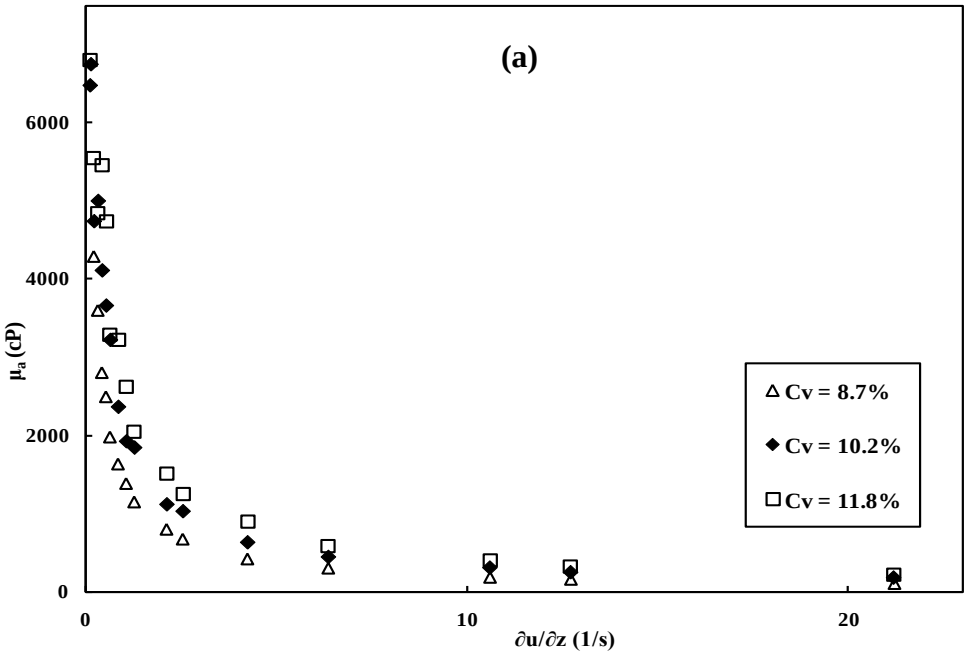
(a)
6000
4000
2000
0
μa (cP)
0
10
20
∂u/∂z (1/s)
Cv = 8.7%
Cv = 10.2%
Cv = 11.8%

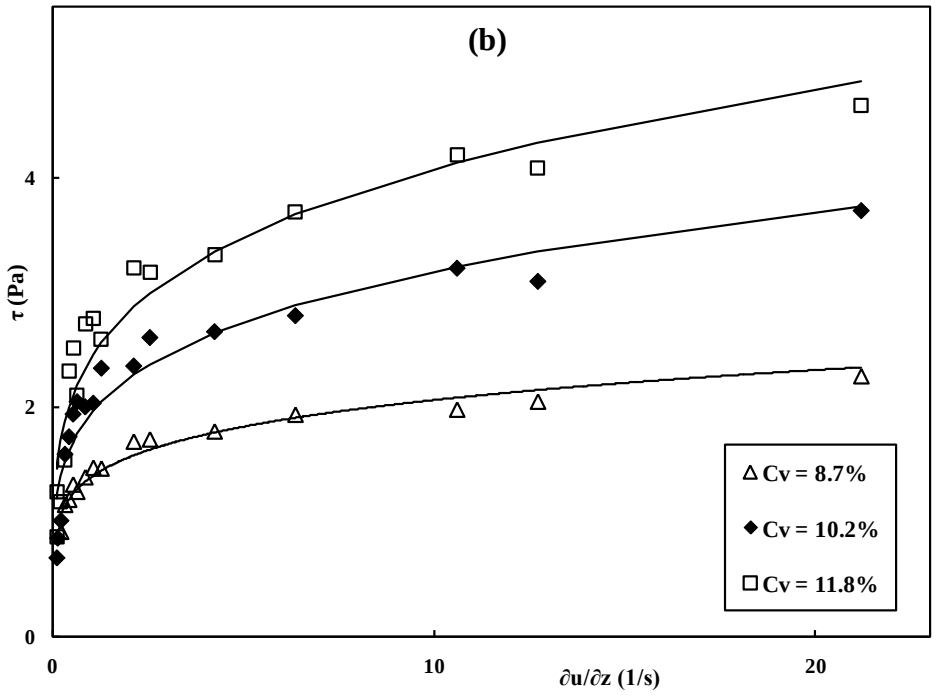
(b)
4
2
0
τ (Pa)
0
10
20
∂u/∂z (1/s)
Cv = 8.7%
Cv = 10.2%
Cv = 11.8%

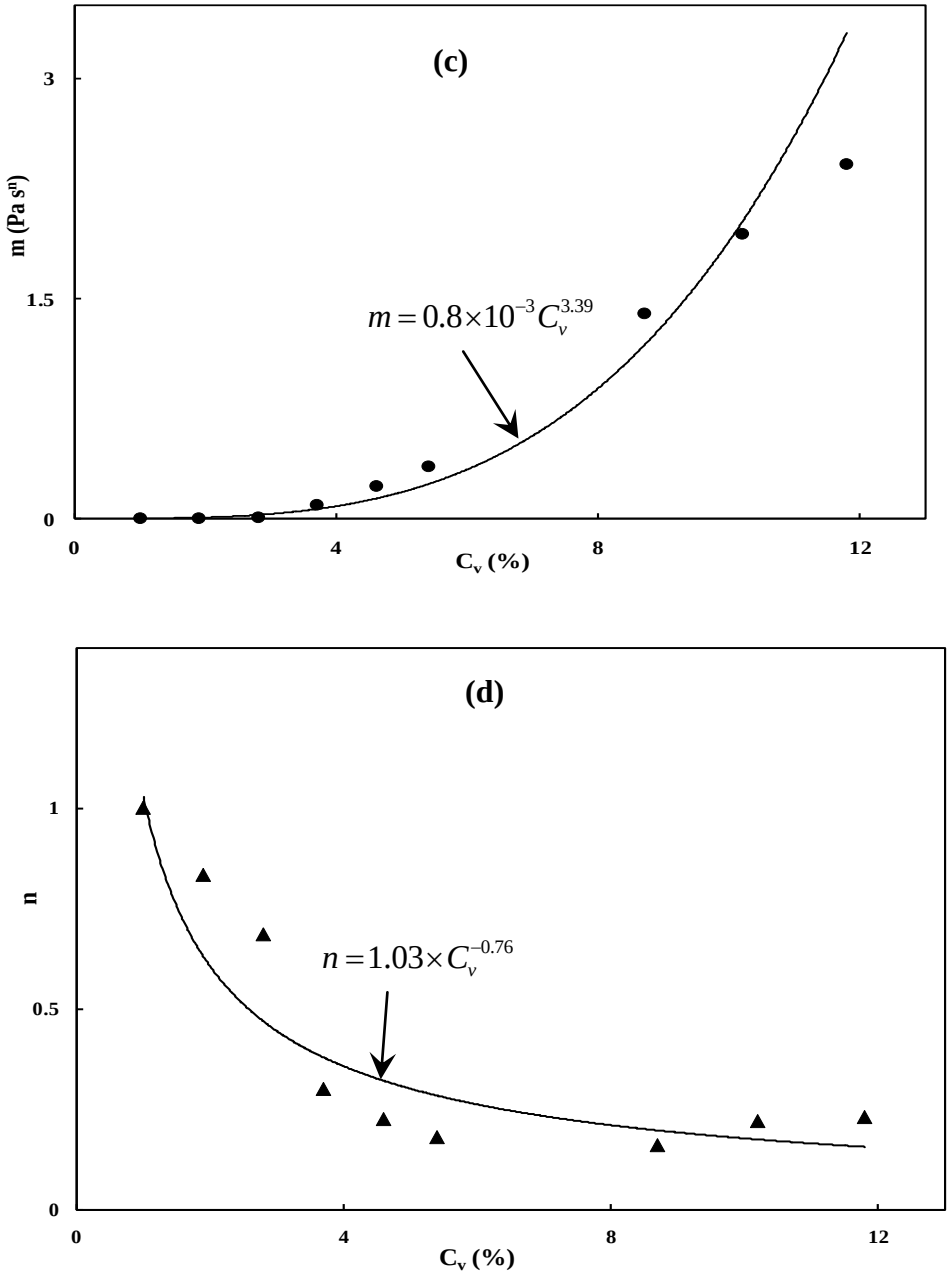

Figure 3.7. Rheological properties of the fluid mud suspension: (a) Measured apparent viscosity, μ_a, as a function of shear rate, $\partial u/\partial z$, (b) shear stress, τ, as a function of shear rate, $\partial u/\partial z$, for three different concentrations of mixtures, (c) consistency index, m, as a function of volume concentration, C_v, (d) flow behavior index, n, as a function of volume concentration, C_v. Symbols represent measurements and the legend identifies the volume concentration values of the fluid mud mixtures. The solid line in (b) indicates the fitted power-law model, and solid lines in (c) and (d) represents the estimations by the developed empirical parameterizations for m and n values as a function of C_v.

For fixed volume experiments tabulated in Table 1, power-law constants (flow behavior index, *n*, and consistency index, *m*) were determined for 7 different suspensions and for the constant flux release experiments tabulated in Table 2, and power-law constants (flow behavior index, *n*, and consistency index, *m*) were determined for 9 different suspensions. The developed parameterizations during fixed volume release experiments were: $m = 1\times10^{-3} C_v^{3.43}$ and $n = 1.26\times C_v^{-0.86}$, and during constant flux experiments were: $m = 0.8\times10^{-3} C_v^{3.40}$ and $n = 1.03\times C_v^{-0.76}$ (here, unit of *m* is $Pa.s^n$). As it appears, the parameterizations are not exactly the same, but differ marginally. However, the developed parameterizations are of the same form as the parameterizations proposed by Ng and Mei (1994). Note that the differences in the parameterization of this study and Ng and Mei (1994) are expected, since different sediments were used in these two studies. The estimated *m* and *n* values using these parameterizations for all of the experiments are tabulated in Tables 3.1 and 3.2.

3.2.2 Flow Rate Measurement

The flow rates for the two dimensional and radial constant flux release experiments were measured by a magnetic flowmeter (Signet Magmeter Flow Sensor) which can measure the flow rate of mud accurately. The magmeter was connected to the computer via 'Signet 3-0250 USB to S^3L Configuration/Diagnostic Tools' interface. Hence, the flowmeter values can be recorded and saved directly to the computer during experiments.

3.2.3 Flow Characteristics Measurement

For the two-dimensional experiments, the propagation of experimental currents was recorded using with two high definition Sony camcorders with 30 frames per second from one side of the Plexiglas tank. The field of view for each camcorder was adjusted to cover the respective half of the flume length. Recorded videos were later digitized using commercial software to obtain 30 images per second of recording. A systematic approach was used to determine the front position and height information over time from the digitized images. First, optical calibration factors (total of 40 calibration factors) between the vertical reference lines along the flume were calculated to be used in converting current geometric characteristics from pixels to real world length units. The reason for calculating more than one calibration factor is simply to avoid any optical distortion errors that are associated with such large field of views (≈ 200 cm for each camera). Then, the experimental front positions were obtained by summing the distance of the front from the closest vertical reference line upstream of the front and the absolute position of the reference line. The distance of the front from the reference line is calculated by multiplying the total number of pixels between the front and the reference line and the respective calibration factor for that position. Similarly, the current height is calculated by multiplying the number of pixels corresponding to the current height and the calibration factor for a given position.

For the radial experiments, each of the experiments was recorded using two high definition Sony camcorders: one from the side and the other from the top. The top camera

was placed high enough to reduce any parallax error. The recorded video signals were then fed into a computer and digitized using commercial software to obtain 30 individual images per second of recording. A similar systematic approach was used to determine radial propagation distance measurements of current fronts as a function of time from the digitized images. First, optical calibration factors (total of 8 calibration factors) between the concentric reference circles on the floor were calculated for use in converting geometric characteristics of a current from pixels to length units. The experimental radial front positions, r_N, were then obtained by summing the distance of the current front from the closest concentric reference circle upstream of the front and the absolute position of that reference line. With respect to the discharge impact point (i.e. center of the concentric circles), the distance of the front from the reference circle was calculated by multiplying the total number of pixels between the front and the reference circle and the respective calibration factor for that position.

CHAPTER FOUR

PROPAGATION PHASES AND THEIR TRANSITIONS

This chapter is devoted to the analysis of the propagation of fluid mud underflows generated in the experimental setups described in the previous chapter (chapter three) to elucidate propagation phases and their transitions. The propagation curves (i.e. temporal evolution of front position) for the fluid mud underflows are presented in section 4.1. Using the propagation curves, the propagation phases observed in experiments are identified in section 4.2. As the fluid mud underflows propagate they undergo distinct propagation phases (e.g. slumping - for fixed volume release, wall jet – for constant flux release, inertia-buoyancy, and viscous-buoyancy, see Chapter 2 for detailed discussion). Because propagation characteristics of each phase vastly differ from one another, a different modeling approach is required for each phase. Therefore, it is important to identify the phase transition positions/times to implement the appropriate modeling approach. Therefore, in section 4.3 the propagation phase transition times and positions for fluid mud underflow experiments listed in Tables 3.1, 3.2 and 3.3 are analyzed and compared with the prediction of developed order-of-magnitude expressions. Part of the results and analysis presented in this chapter appeared in Chowdhury et al. (2009), Chowdhury and Testik (2011a), and Chowdhury and Testik (2011b), and under review in Chowdhury and Testik (2011c).

4.1 Propagation of Fluid Mud Underflows

In this section, the experimental observations on the propagation of fluid mud underflows generated in both rectangular flume and square pool are presented.

4.1.1 Two-Dimensional Fluid Mud Underflows

The outcome of a typical experiment in the rectangular flume (both constant volume and constant flux release) is a two-dimensional fluid mud underflow that propagates along the tank bottom, displacing the less dense ambient water. Fig. 4.1 shows pictorial representation of the propagation of a typical two-dimensional fluid mud gravity current over time.

As is discussed in chapter 2, the typical frontal structure of the saline gravity current was investigated in a number of previous investigations. Encouraged by their investigation, the three-dimensional flow structure of fluid mud underflow generated from constant volume of fluid mud release was captured in this investigation. Fig. 4.2 shows the three-dimensional frontal structure of fluid mud underflows, which qualitatively conforms to that of a salt-water gravity current presented by Simpsons (1999), also described in Chapter 2. As can be seen in Fig. 4.2, the frontal zone is associated with lobe-cleft patterns at the leading-edge and billows that form above and behind the head of the current. The other distinguishable feature of the leading edge is that lobes are observed to grow in size over distance from the nose. After attaining a maximum size at a certain distance from the nose, the lobes gradually decay and subsequently breakdown.

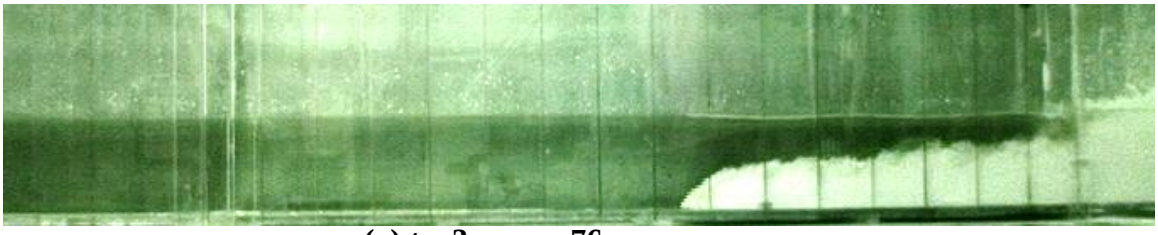

(a) t = 3 s, x_N = 76 cm

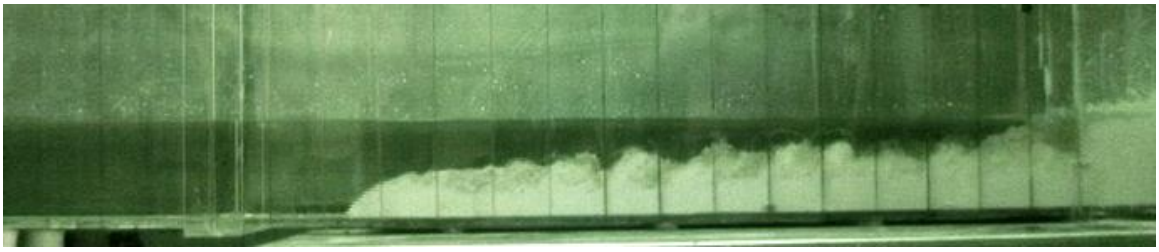

(b) t = 6 s, x_N = 136 cm

(c) t = 36 s, x_N = 385 cm

Figure 4.1. Photographs showing the propagation of two-dimensional fluid mud underflow over time, t. Currents in (a) and (b) are in inertial phase, while current in (c) is in viscous phase. Experimental conditions: Exp. #9 (Table 3.1).

The next two subsections discuss the experimental propagation curves for two-dimensional fluid mud underflows from constant volume and constant flux release experiments.

4.1.1.1 Constant Volume Release

In Fig. 4.3, experimentally measured front positions, x_N (see definition sketch in Fig. 3.1 of chapter 3), of the fluid mud underflows generated by releasing a fixed volume of the dense fluid mud with different initial concentrations in the lock-exchange set-up (see Section 3.1.1, chapter 3) as a function of propagation time, t, are presented (see Table 3.1 for the experimental parameters).

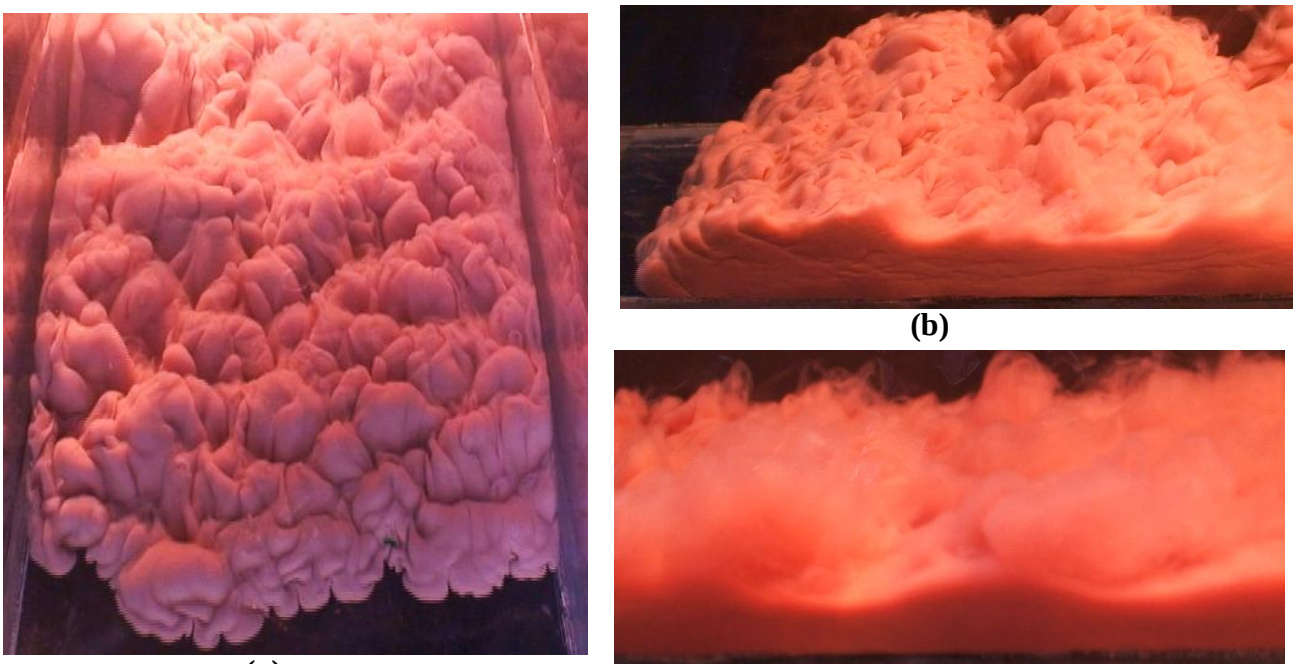

(a) **(b)** **(c)**

Figure 4.2. Frontal structure of fluid mud gravity current. Top- (a) and side-view (b, c) photographs of fluid mud gravity current are presented. In these photographs, lobe-cleft patterns at the leading edge of the current (a), nose and billows above and behind the head of the current (b), decay and breakdown of the billows, and (c) behind the nose can be seen.

As is evident in Fig. 4.3, the initial front propagation velocities of the gravity currents with higher initial concentrations are larger due to the larger driving gravitational / buoyancy force. However, all propagation curves have a similar initial trend, a steep constant-slope initial portion indicating a constant front propagation velocity. These steepest portions of the curves correspond to the slumping phases in the respective experiments. However, a qualitative difference can be seen between the propagation curves in Fig. 4.3a (especially, Exp. #1-5) and Fig. 4.3b. The propagation curves of Fig. 4.3b, which corresponds to the experiments with higher fluid mud concentrations, show a drastic change (decrease) in slope. It may be initially concluded that these experiments experienced the viscous propagation phase and hence the velocity reduced drastically.

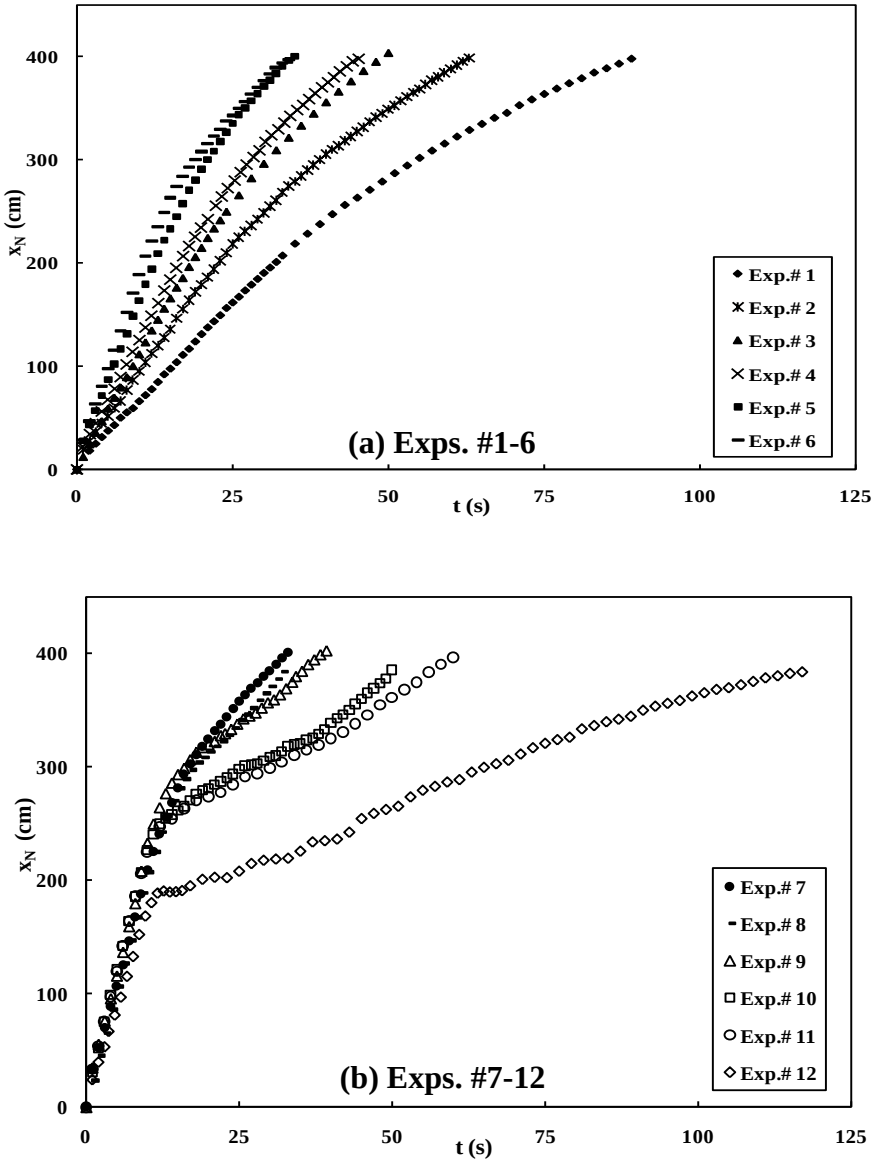

Figure 4.3. Front position of the fluid mud underflows, x_N, as a function of elapsed propagation time, t for the two-dimensional, fixed volume release experiments listed in Table 3.1. Symbols represent the data from the experiments (see the legend).

However, it is difficult to discern the self-similar and viscous phase transitions from this figure. By appropriate scaling, three propagation phases for these curves are distinguished in Section 4.2.1.1.

4.1.1.2 Constant Flux Release

In Fig. 4.4, the experimentally measured front positions, x_N, of fluid mud underflows generated in the two-dimensional constant flux release experimental set-up (see Section 3.1.2 of chapter 3) as a function of propagation time, t, for the experiments listed in Table 3.2 are presented. As is clearly evident, all propagation curves, except for Exp. #13 and 14, have a similar behavior with an initial portion of the curves associated with a steeper slope, and then followed by a relatively abrupt transition to milder slopes. However, it is difficult to discern the respective propagation phases from these curves. They are distinguished by applying an appropriate scaling in Section 4.2.1.2. Note that the slumping phase does not exist for constant flux release experiments, and a two-dimensional horizontally buoyant wall jet may form initially. Subsequently, this jet may first transition into an inertial gravity current, which may then transition into a viscous gravity current.

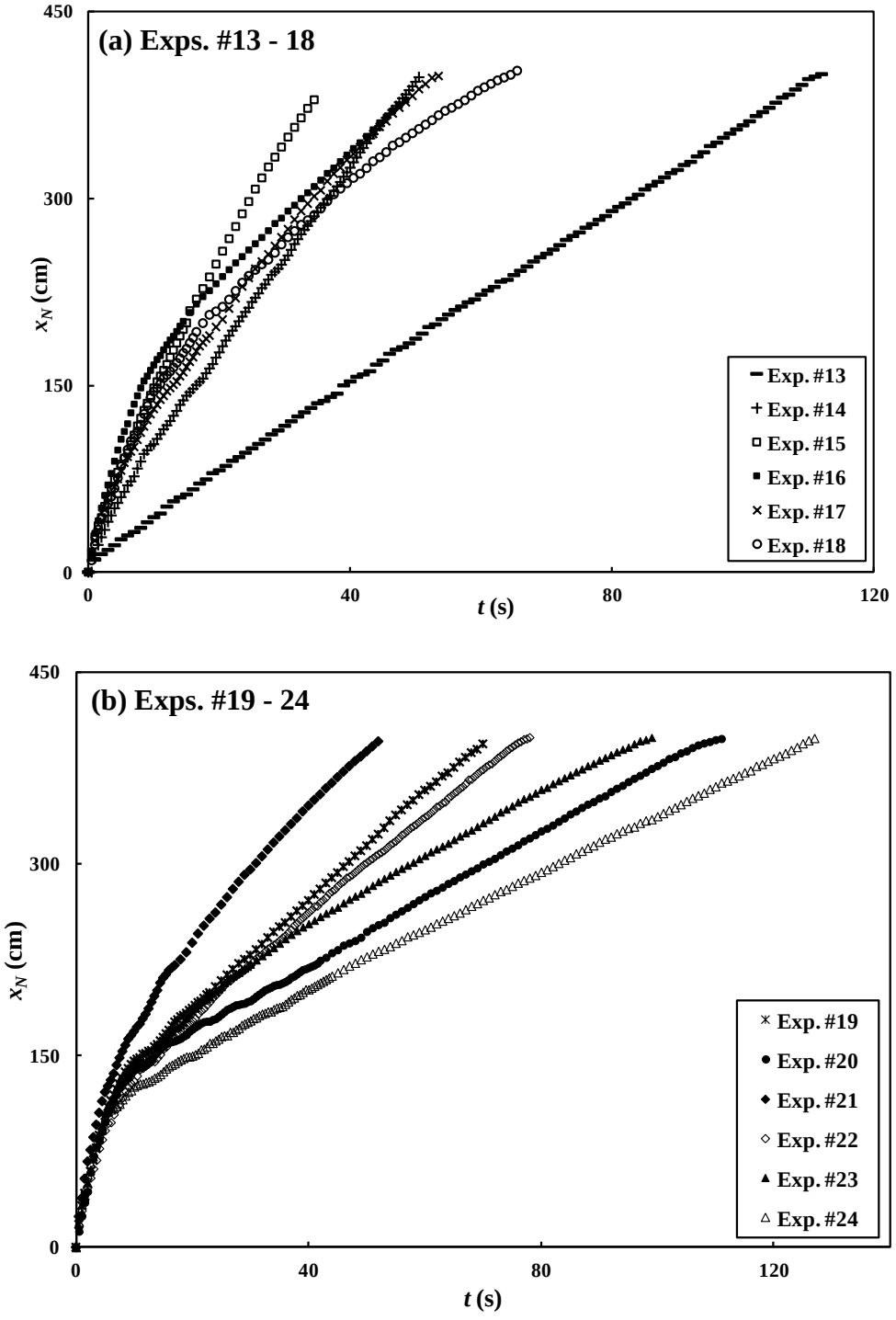

Figure 4.4. Front position of the fluid mud underflows, x_N, as a function of elapsed propagation time, t for the two-dimensional, constant flux release experiments listed in Table 3.2. Symbols represent the data from the experiments (see the legend).

4.1.2 Radial Axisymmetric Fluid Mud Underflow

As soon as the fluid mud is discharged from the discharge pipe in the square pool, it formed a buoyant jet of the discharged fluid mud which impinges on the bottom and generates an axisymmetric fluid mud underflow propagating radially from the impingement point. Since the discharge pipe is vertical in all of our experiment, the shape of the underflow for all experiments were axisymmetric (see Fig. 4.5), which conform to the observations of a number of previous studies (see chapter 2 for detailed discussion). The axisymmetric propagation of fluid mud underflow observed in a typical radial experiment can be seen in the sequential pictures presented in Fig. 4.5.

In Fig. 4.6, experimentally measured radial front positions, r_N, of radially axisymmetric fluid mud underflows for the experiments listed in Table 3.3 as a function of propagation time, t, are presented. As is evident, the initial front propagation velocities of underflows with higher initial concentrations are larger due to the larger driving gravitational/buoyancy force. The propagation phases for these curves are distinguished in section 4.2.2.

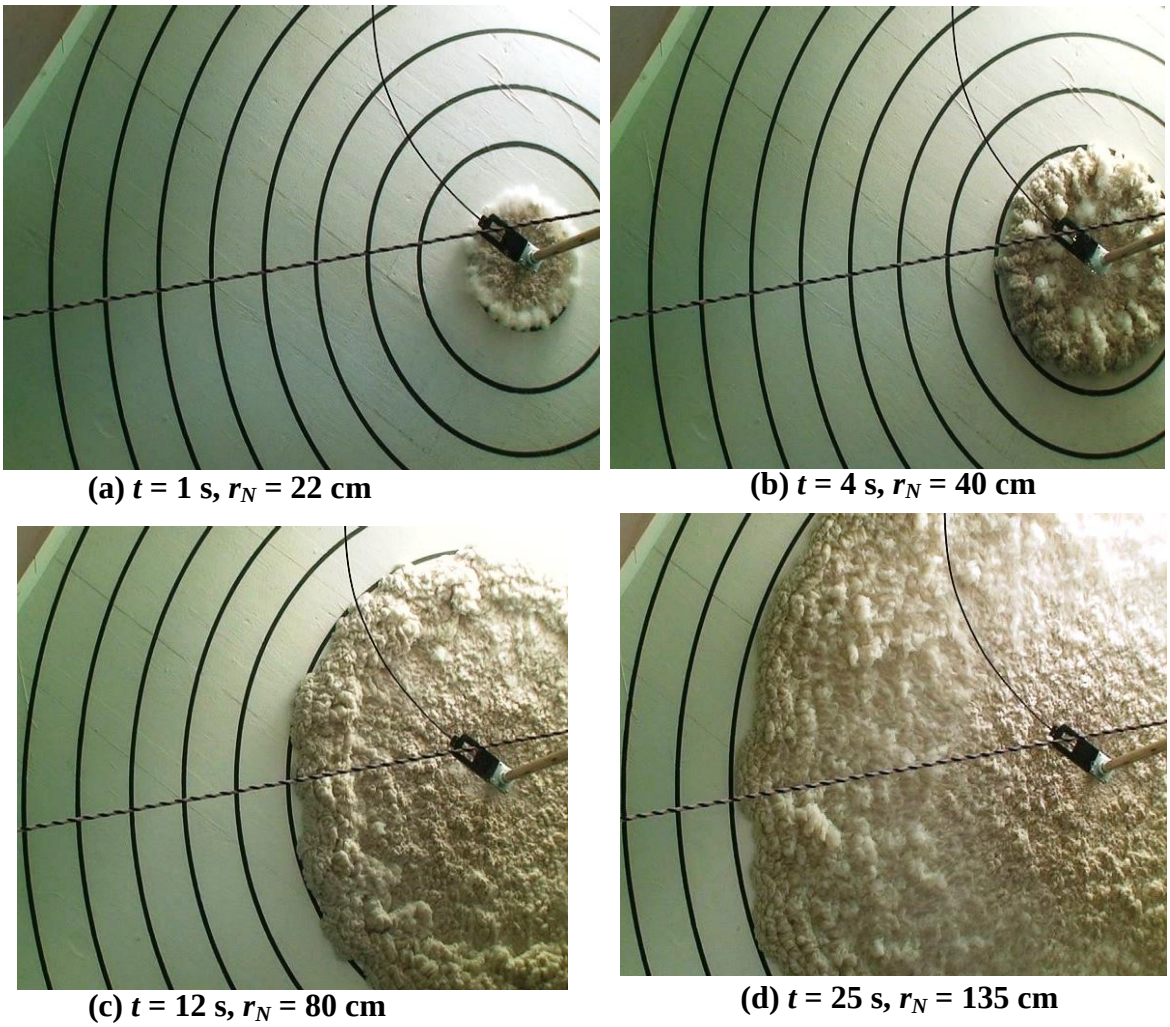

(a) t = 1 s, r_N = 22 cm **(b) t = 4 s, r_N = 40 cm**

(c) t = 12 s, r_N = 80 cm **(d) t = 25 s, r_N = 135 cm**

Figure 4.5. Photographs showing the propagation of radial fluid mud underflows over time, *t*. Experimental conditions: Exp. #29 (Table 3.3)

.

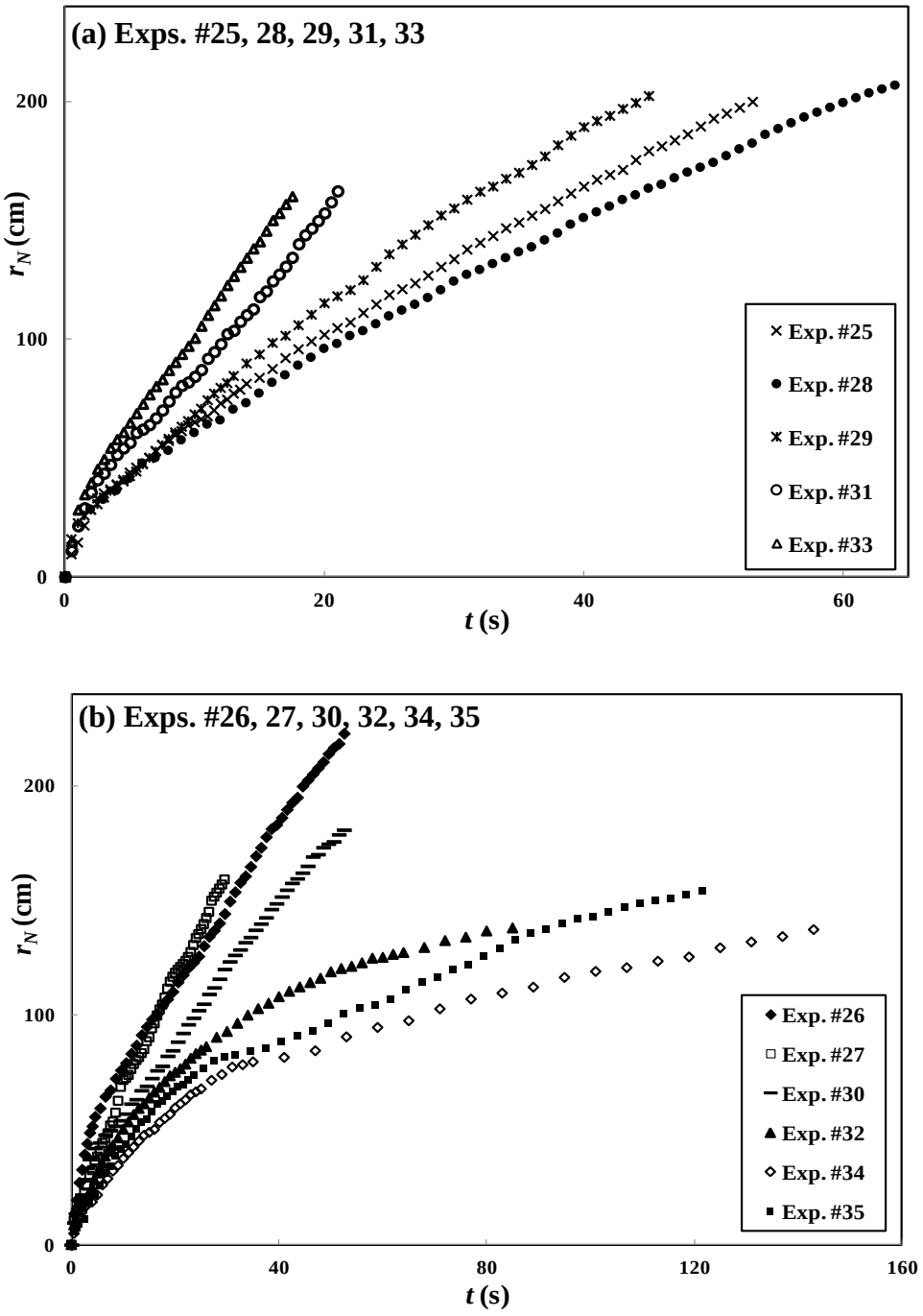

Figure 4.6. Front position of the axisymmetric fluid mud underflow, r_N, as a function of elapsed propagation time, t for the radial, constant flux release experiments listed in Table 3.3. Symbols represent the data from the experiments (see the legends).

4.2 Propagation Phases

In this section, the different phases for the propagation curves presented in section 4.1 are distinguished by a systematic method. This method is based upon relating the slope of the propagation curves on a log-log plot to the predicted slopes of theoretical models. The front positions of two-dimensional and radially axisymmetric underflows vary in different propagation phases with time variable, *t* as tabulated in Table 4.1:

Table 4.1. Variation of front position with time for two-dimensional and axisymmetric fluid mud underflows in different propagation phases.

Current	Slumping	Wall Jet	Inertial	Viscous
2-D	$x_N \sim t$	$x_N \sim t^{\frac{2}{3}}$	$x_N \sim t^{\frac{\alpha+2}{3}}$	$x_N \sim t^{\frac{n+\alpha(n+2)}{2n+3}}$
Axisymmetric	----	$r_N \sim t^{\frac{1}{2}}$	$r_N \sim t^{\frac{\alpha+2}{4}}$	$r_N \sim t^{\frac{n+\alpha(n+2)}{3n+5}}$

When the experimental front positions are plotted as a function of time on a log-log scale, the expected propagation curve slopes for two-dimensional and radial underflows should conform to the power of time given in Table 4.1. Therefore, for the two-dimensional constant volume release case, the slopes corresponding to the slumping and inertial propagation phases are 1 and 2/3, respectively. However, the slope corresponding to the viscous phase will vary depending on the consistency index, *n*. For a Newtonian gravity current, the slope corresponding to the viscous phase is 1/5. For the two-dimensional constant flux release case $\left(i.e.\ \alpha = 1\right)$, the slope corresponding to the buoyant wall jet and inertia-buoyancy phase are 2/3 and 1, respectively. The slope corresponding to the viscous phase for this case varies (slope ≈ 0.68-0.78 for $n \approx 0.1$-1).

For the radial constant flux release case $(i.e.\ \alpha = 1)$, the slopes corresponding to the jet and inertia-buoyancy phases are 1/2 and 3/4, respectively. Again, the slope corresponding to the viscous phase varies depending on the value of *n*.

In the following sub-sections, the propagation phases of each experiment are determined following the method described above.

4.2.1 Two-Dimensional Fluid Mud Underflows

The propagation phases of the propagation curves corresponding to the two-dimensional fluid mud underflows presented in Figs. 4.3 and 4.4 are identified in this section.

4.2.1.1 Constant Volume Release

In order to determine the transitions from the slumping to inertial phase and then inertia to viscous phase, a log-log plot of the dimensionless front position ($X_N = x_N/x_o$; x_0 – lock length and h_0 – lock height) vs. dimensionless time ($T = \frac{t}{x_0 / \sqrt{g'_a h_0}}$) following the procedure of Rottman and Simpson (1983) for saline gravity currents is used. In Fig. 4.7, a log-log plot of X_N vs. T for the fluid mud underflows from our experiments with different initial concentrations is given. In non-dimensionalization and all the calculations presented later in the dissertation, initial value of g'_a for the prepared fluid mud suspensions was used instead of the g'_a value at a given position. Because it is assumed that the underflows density does not change significantly for the experimental

propagation distances and times due to small settling velocities of clay particles and low entrainment of ambient fresh water. To verify this assumption, Exp. #11 was repeated and sampled small amounts of fluid mud from the propagating underflows at 1, 2 and 3 meters from the lock-gate using sampling probes operating under vacuum. The measured densities of those collected samples at different positions showed negligible variation from the initial value, verifying the assumption. As it can be seen from Fig. 4.7, the experimental data are characterized by three distinct slopes: ≈1 (more accurately, 0.95) for the slumping phase, 2/3 for the inertial phase, and a variable slope value as a function of the n value of the fluid mud suspension for the viscous phase which conform to the expected results (see description above and Table 4.1). Please note that given the limited length of the experimental tank only some of the generated fluid mud currents (Exps. # 7-12 in Table 3.1) had sufficient propagation distance to transition into a viscous propagation phase. After the slumping phase, all of the underflows (Exps. # 1-11 in Table 3.1) exhibited the inertial phase, except for the underflow in Exp. # 12 (see Table 3.1) that transitioned directly into the viscous phase bypassing the expected inertial phase.

4.2.1.2 Constant Flux Release

To identify the transition positions and times among the wall jet, inertial and viscous propagation phases for two-dimensional constant flux release experiments (Table 3.2), a different form of scaling than the one used in Section 4.2.1.1 was applied. In Fig. 4.8a, scaled front positions ($X_N = x_N / h_i$) as a function of scaled time ($T = \frac{t}{h_i B_0^{-1/3}}$;

$B_0 = g'_a q_0$ is the initial buoyancy flux at the inlet) are plotted for all of the experiments. As is seen in this figure, initial portions of the scaled propagation curves collapse onto a line (dashed line) with a slope of 0.7, which conform to the expected buoyant jet slope of 2/3. In order to be ascertained that they conform the jet-like propagations, the initial portions of the propagation curve are plotted with scaled front positions ($X_N = x_N / h_i$) as a function of scaled time based on two-dimensional jet-propagation ($T = \frac{t}{h_i M_0^{-1/4}}$; M_0 is the initial momentum flux at the inlet) in Fig. 4.8b for all of the experiments. It can be seen they can be represented by a jet-like expression, $x_N \sim t^{\frac{2}{3}}$. After the conclusion of the jet phase, the propagation curves for Exps. #13-15 collapse onto a line (solid line) with a slope of 1, which is equal to the expected slope value for the inertial phase. The remainder of the experimental propagation curves deviated from these two lines indicating the commencement of viscous propagation phase in respective experiments. As noted earlier, the expected value of the slope for viscous propagation curves of the constant flux release experiments is close to 0.7 (ranging between 0.68-0.78 for the experimental conditions). As it can be seen in Fig. 4.8, the viscous propagation curves approximately conform to the slope value 0.7 (see the triangle with slope 0.7 and the experimental values in Fig. 4.8c). Note that while there was sufficient propagation distance for the underflows generated in Exps. #15-24 to transition into viscous-buoyancy propagation phase, the gravity currents generated in Exps. #13 and 14 did propagate in the inertia-buoyancy phase for their remaining propagation did not transition into viscous phase given the limited size experimental tank.

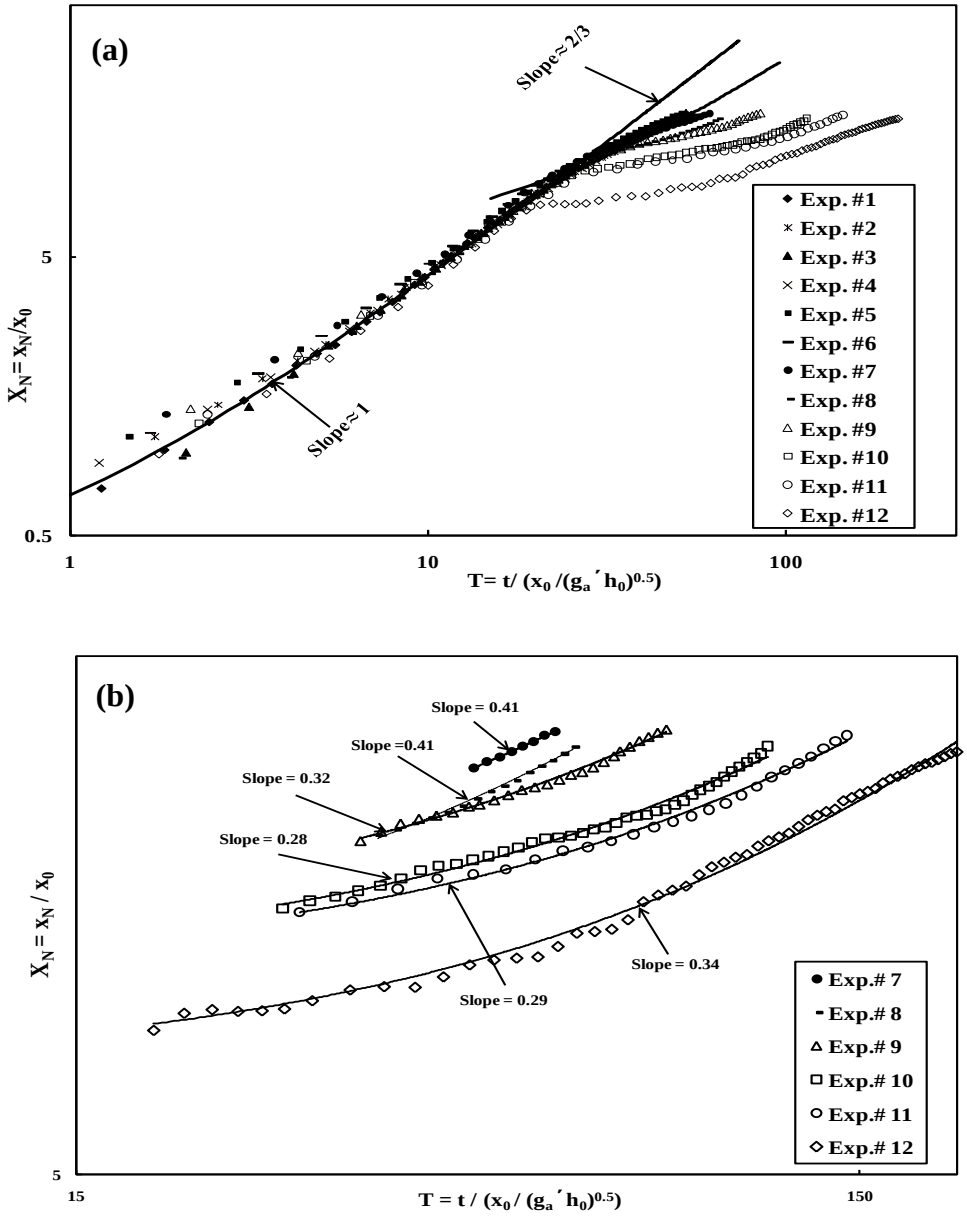

Figure 4.7. Log-log plots of dimensionless front position, X_N, vs. dimensionless time, T, for the 2-D constant volume release experimental currents listed in Table 3.1 (lock-exchange set-up). Experimental data for all three propagation phases (i.e., slumping, inertial, and viscous) are shown in (a), and the part of the data corresponding to only the viscous phase for Exps. # 7-12 are shown in (b). Symbols represent the data from the experiments tabulated in Table 3.1 and are defined in the legend.

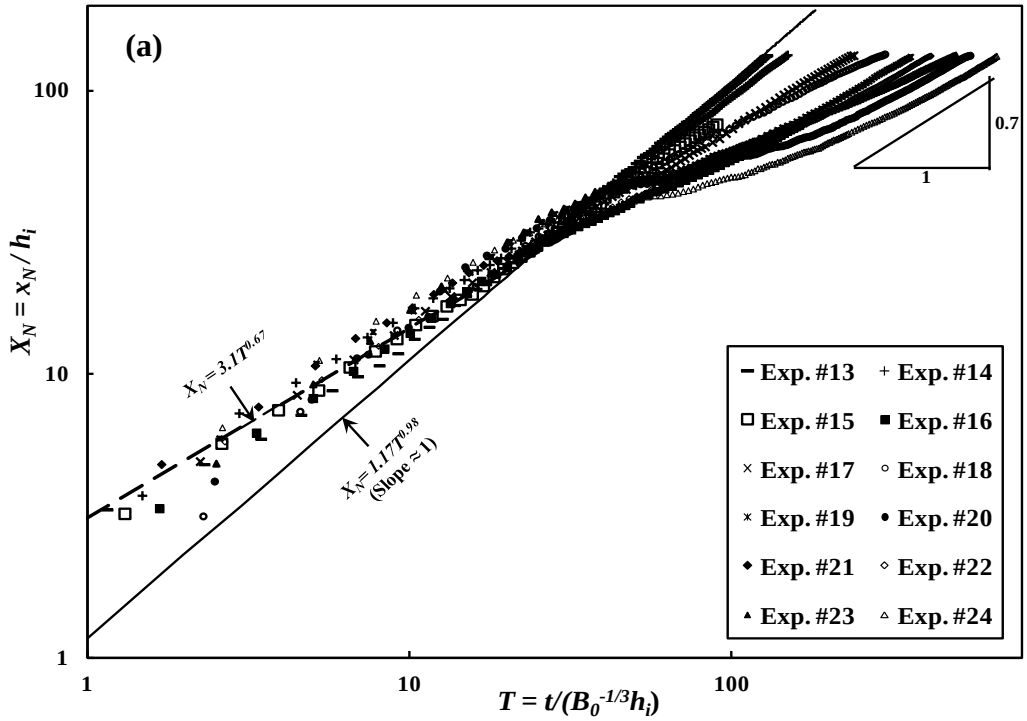
(a)
100
10
1
1
10
100
$X_N = x_N / h_i$
$T = t/(B_0^{-1/3} h_i)$
$X_N = 3.1T^{0.67}$
$X_N = 1.17T^{0.98}$
(Slope ≃ 1)
0.7
1
Exp. #13
Exp. #14
Exp. #15
Exp. #16
Exp. #17
Exp. #18
Exp. #19
Exp. #20
Exp. #21
Exp. #22
Exp. #23
Exp. #24

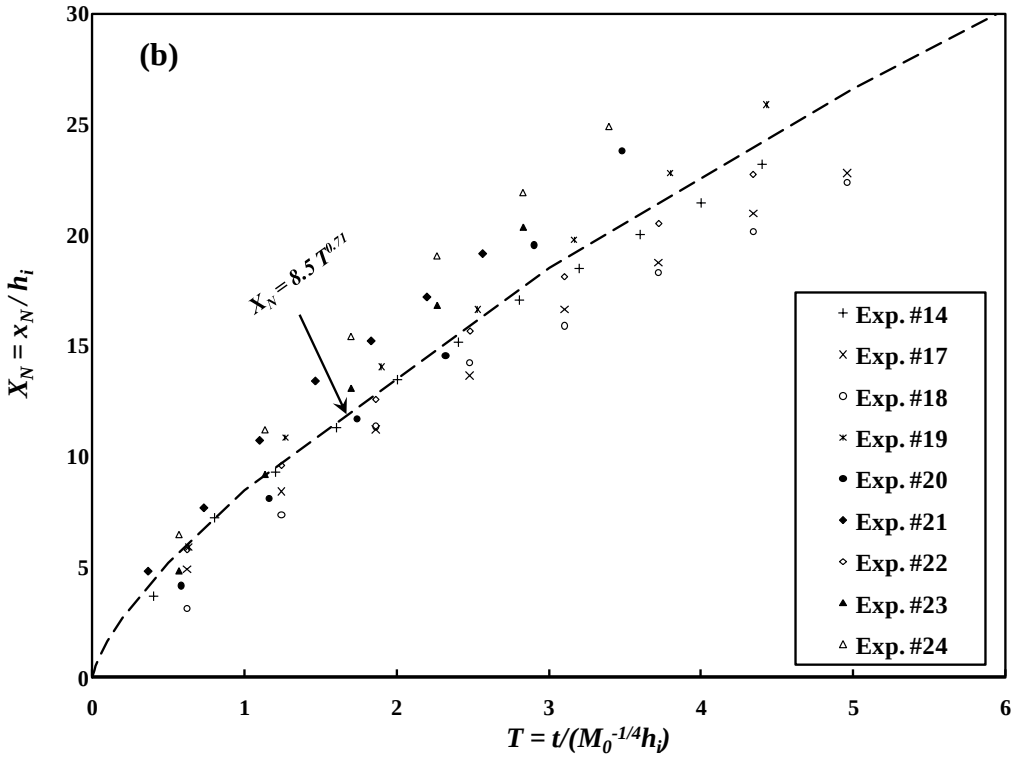
(b)
30
25
20
15
10
5
0
0
1
2
3
4
5
6
$X_N = x_N / h_i$
$T = t/(M_0^{-1/4} h_i)$
$X_N = 8.5\,T^{0.71}$
Exp. #14
Exp. #17
Exp. #18
Exp. #19
Exp. #20
Exp. #21
Exp. #22
Exp. #23
Exp. #24

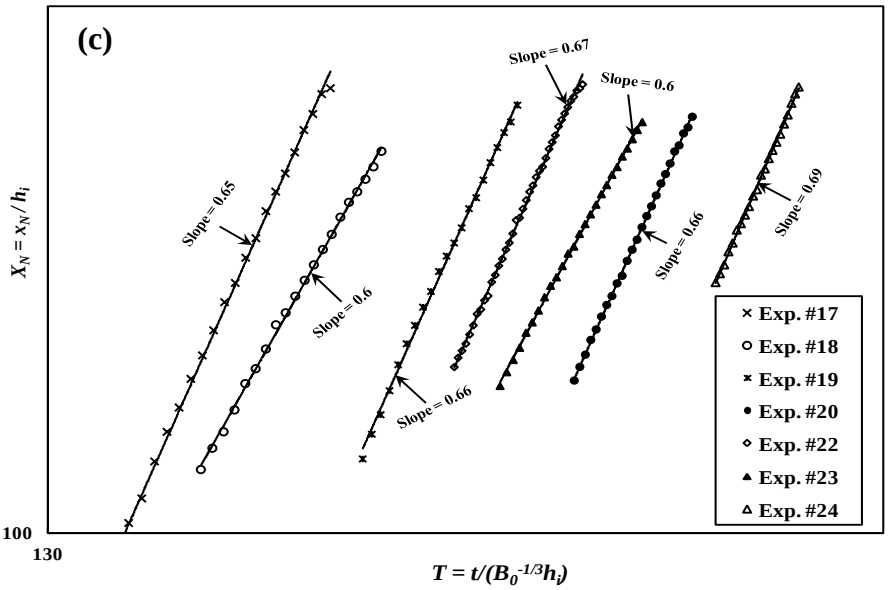

Figure 4.8. Scaled front position, X_N, vs. scaled time, T, for all of the 2-D constant flux release experimental currents listed in Table 3.2. Experimental data for all three propagation phases (i.e., jet, inertial, and viscous) are shown in (a), only the jet part of the curves is shown in (b) with scaling of jet, and the slope of the viscous part of the data for Exps. # 17-24 are shown in (c). Solid lines represent the slopes of the current position curves.

4.2.2 Radial Axisymmetric Fluid Mud Underflows

In order to determine the propagation dynamics of underflows presented in Fig. 4.6, scaled radial front positions of the experimental gravity flows ($R = r_N/h_d$; h_d – discharge height) as a function of scaled time ($T = \dfrac{t}{h_d^{4/3}B_0^{-1/3}}$; here, $B_0 = g_a'Q_0$) are plotted as a log-log plot in Fig. 4.9a. Note that a similar form of scaling was used as in for two-dimensional constant flux release experiments. In well-established buoyant jet analysis, a virtual origin offset is typically made in order to account the effect of a non-ideal area source. Fig. 4.9b is the counterpart of Fig. 4.9a in which the virtual origin offset is made by replacing h_d with h_d+z_{avs} where z_{avs} is the distance of a asymptotic virtual source

above the actual source at $z=0$. z_{avs} is calculated for the experiments listed in Table 3 using the scale diagram of Morton and Middleton (1973) and Bremer and Hunt (2010).

As seen in Fig. 4.9a, the initial portions of the propagation curves for all of the experiments collapse on a line (dash-line). After some propagation time, the curves collapse on the inertial slope of 0.75. Since the scaling used in the Fig 4.9 is based on inertial propagation of a gravity current, the initial jet portion is plotted in Fig. 4.10 based on jet scaling. The curves of Exps. #32, 34 and 35 deviates from the inertial line indicating the transition from the inertial phase to the viscous phase. It is evident from Fig. 4.9 that most of these fluid mud gravity currents (except Exps. #32, 34, and 35) in the radial experiments are governed by the inertia-buoyancy balance for most of their propagation before reaching the side walls of the pool for the experimental conditions studied.

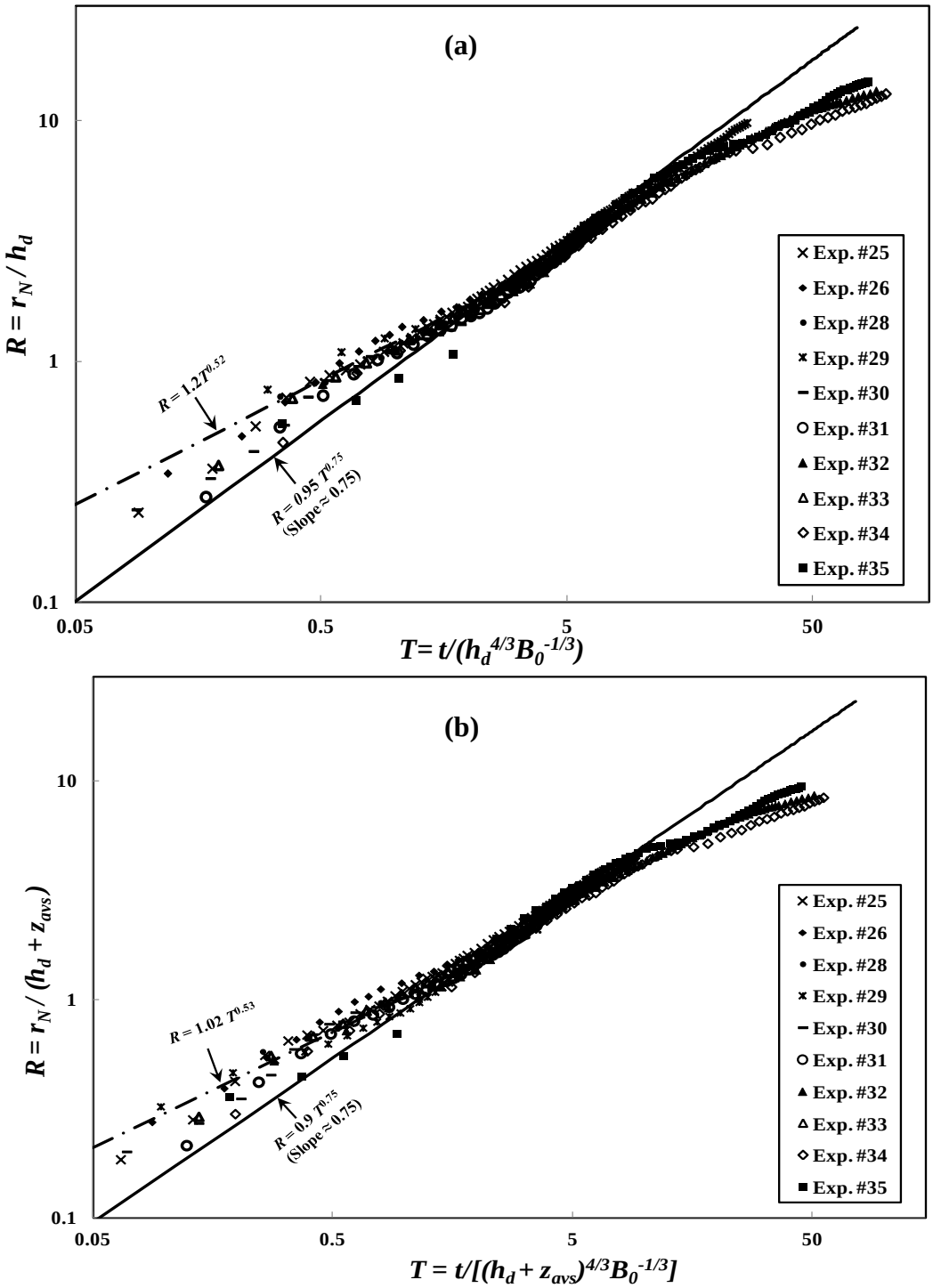

Figure 4.9. Log-log plot of dimensionless radial front position, *R*, vs. dimensionless time, *T* is shown without virtual origin offset in (a), and with virtual origin offset in (b). Symbols represent the data from the experiments tabulated in Table 3.3 and are defined in the legend.

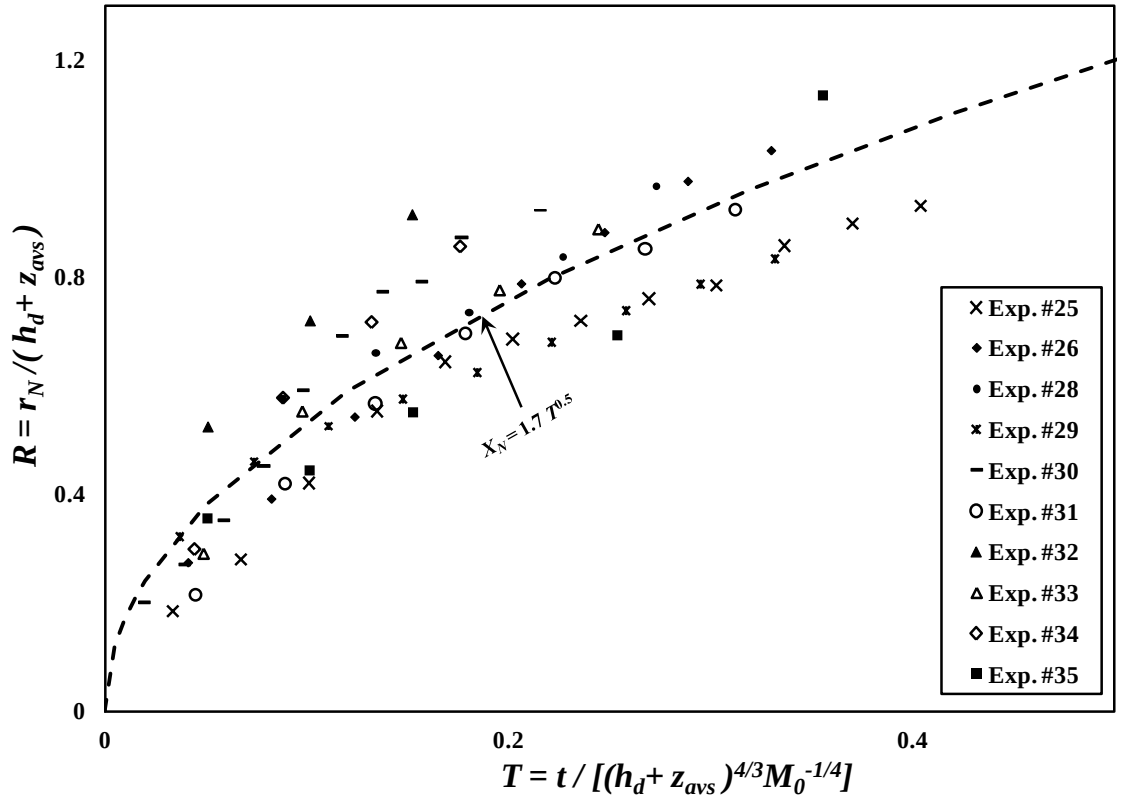

Figure 4.10. Dimensionless radial front position, *R*, vs. dimensionless time, *T* for the jet-like propagation of radial experiments (Table 3.3). Scaling is based on theoretical model of buoyant wall-jet propagation.

4.3 Transition Time and Position

In this section, the transition time and position from one propagation phase to another phase are analyzed.

4.3.1 Constant Volume Release

There are two phase transition times in the fixed-volume release experiments characterizing transitions: (i) from slumping phase to inertial phase, t^*, and (ii) from slumping/inertial phase to viscous phase, t^{**}. Determining the value of the dimensionless transition time from slumping to inertial phase, t^{**} is relatively

straightforward using a log-log plot of the experimental data in Fig. 4.7a. The experimental data from slumping and inertial phases collapses onto two separate lines (shown as solid lines in Fig. 4.7a) and the T^* value corresponds to the T value at the intersection point of these two lines (i.e., T=24).

$$T^* = \frac{t^*}{x_0 \Big/ \sqrt{g'_{a,0} h_0}} = 24. \tag{4.1}$$

The estimated transition time to inertial phase, t^*, for all of the experiments are given in Table 4.2. It can be seen from this table that t^* decreases as the initial concentration of the fluid mud increases. However, since the propagation velocity of higher concentration suspensions are higher, the transition length x^* ($x^* = x_N$ at t^*), the propagation distance till the end of slumping phase, is approximately constant (≈ 215 - 255 cm) for all the experiments, except Exp. #12. This x^* value corresponds to approximately 9-10 lock-lengths for the experimental set-up and conforms to observations of previous studies for compositional Newtonian gravity currents that reported x^* values of 5-10 lock-lengths (see Meiburg and Kneller, 2010). For very high concentration suspensions, the current may make a transition to the viscous phase even before the slumping phase has been completed and the inertial phase may be absent (see Exp. #12 in Fig. 4.7). This is the reason why the slumping length, x^*, in Exp. # 12 is much less than that of other experiments.

The transition time to viscous phase, t^{**}, is determined both experimentally and theoretically and are presented in Table 4.2. The experimental t^{**} is calculated by determining the dimensionless time that the experimental data start deviating from the

Table 4.2. The transition times and positions for experiments in Table 3.1. The front positions, x_N at t^* and t^{**} are determined from the experimental data.

Exp. #	**t^* (s) (from Eq. 4.1)**	**x_N at t^* (cm) (expt.)**	**t^{**} (from Eq. 4.2)**	**t^{**} (s) (expt.)**	**x_N at t^{**} (cm) (expt.)**
1	39.2	238.0	-------	-------	-------
2	27.8	236.0	401.4	-------	-------
3	22.8	241.0	134.3	-------	-------
4	19.9	234.0	88.7	-------	-------
5	16.4	248.0	52.2	-------	-------
6	14.3	250.0	35.4	-------	-------
7	12.9	255.0	25.7	26.0	363.6
8	11.9	240.0	19.9	18.0	303.6
9	11.1	249.0	16.1	16.0	298.5
10	10.5	215.5	13.8	12.0	249.7
11	9.9	225.0	11.5	11.0	236.0
12	13.6	188.0	13.1	10.7	179.9

solid trend lines in Fig. 4.7. The theoretical t^{**} is calculated using the derived parameterization in appendix A for a non-Newtonian gravity current. The simplified form of this theoretical expression for a constant volume release case $(\alpha = 0)$ is as follows:

$$t^{**} = c_1 \left(\frac{\rho_c{}^3 q_0{}^{n+3}}{m^3 g_c'^{2n}} \right)^{\frac{1}{n+6}}. \qquad (4.2)$$

Here, $q_0=q$ is the volume released per unit width for fixed volume release. This expression is based on the dimensional considerations when the viscous force becomes comparable to the inertia force acting on gravity current. Therefore, an empirical constant coefficient, c_1, term is embedded in Eq. (4.2). Using the experimental t^{**} values, the estimated value of c_1 is 6.6 (see Fig. 4.11). Experimental and calculated t^{**} values using Eq. (4.2) are presented in Table 4.1.

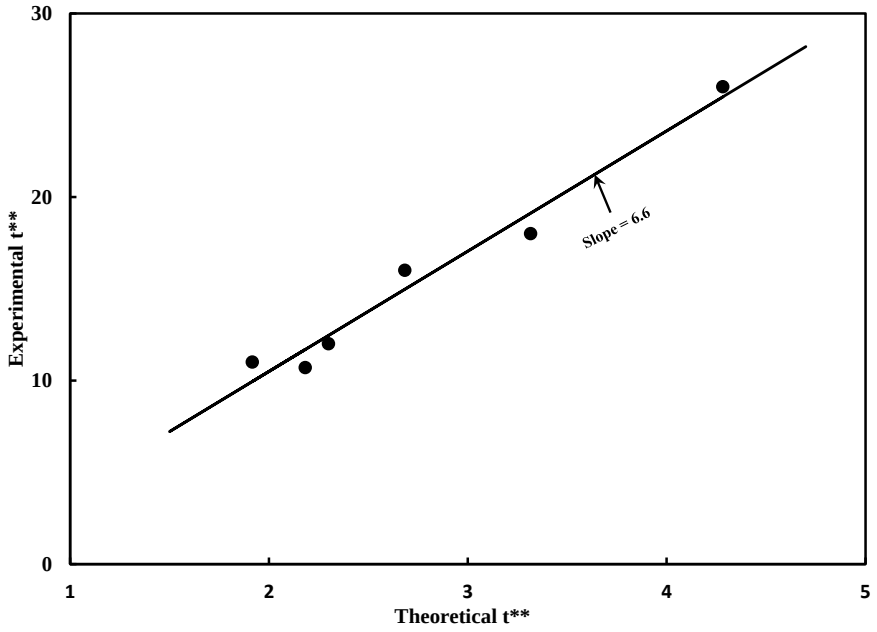

Figure 4.11. Theoretical t** vs. experimental t** for different experimental fluid mud gravity currents. Solid line represents the best-fit line with a slope of 6.6, which is the value of C_1 in Eq. 4.2.

4.3.2 Constant Flux Release

There are two phase transition times in the constant flux release experiments characterizing transitions: (i) from initial buoyant wall jet to inertial phase, t_{cf}^{*}, and (ii) from jet/inertial phase to viscous phase, t_{cf}^{**}. The dimensionless transition time, T_{cf}^{*} and position, X_{cf}^{*} from jet to inertial phase corresponds to T and X_N value at the intersection point of the jet line and inertial line. For two-dimensional fluid mud gravity current, the T_{cf}^{*} and X_{cf}^{*} are:

$$T_{cf}^{*} = \frac{t_{cf}^{*}}{h_i B_o^{-\frac{1}{3}}} = 29.0 \tag{4.3a}$$

$$X_{cf}^{*} = \frac{x_{cf}^{*}}{h_i} = 31.7 \tag{4.3b}$$

The transition time and position from jet to inertial phase, t_{cf}^{*} and x_{cf}^{*}, corresponding to Eq. (4.3) for all of the two-dimensional constant flux release experiments are given in Table 4.3.

For radial axisymmetric fluid mud underflows, the transition times and lengths from initial buoyant wall jet to inertial phase are:

$$T_{cf,r}^{*} = \frac{t_{cf,r}^{*}}{h_d^{\frac{3}{4}} B_o^{-\frac{1}{3}}} = 2.4 \tag{4.4a}$$

$$R_{cf,r}^{*} = \frac{r_{cf,r}^{*}}{h_d} = 1.8 \tag{4.4b}$$

The transition time from jet to inertial phase, $t^*_{cf,r}$ and $r^*_{cf,r}$ corresponding to Eq. (4.4) for all of the radially axisymmetric experiments are given in Table 4.4.

The experimental t** is calculated by determining the dimensionless time that the experimental data starts deviating from either of the jet (in the absence of inertial phase) or the inertial line and they are given in Tables 4.3 and 4.4. Please note that some of the gravity currents in the experiments tabulated in Table 4.3 and 4.4 directly transitions to viscous phase from the jet phase, bypassing the inertial phase. In that case, the viscous transition time, t^{**} is less than the jet transition time.

Table 4.3. Experimental transition time and positions for the jet and viscous phases for two-dimensional constant flux release experiments in Table 3.2.

Exp. #	t^*_{cf} (s)	x_N at t^*_{cf} (cm)	t^{**} (s)	x_N at t^{**} (cm)
13	5.0	26.3	-----	------
14	8.5	97.9	24.0	212.3
15	8.5	130.0	-----	-----
16	7.0	134.9	----	----
17	5.5	88.0	9.5	126.8
18	6.0	98.3	8.5	140.0
19	5.0	103.2	9.0	140.0
20	5.0	98.2	8.5	131.2
21	6.0	131.0	9.0	163.0
22	4.0	77.5	12.0	142.0
23	5.5	111.7	6.0	115.0
24	--	--	6.0	107.8

Table 4.4. The transition time and positions for the jet and viscous phases for radially axisymmetric experiments in Table 3.3.

Exp. #	$t^*_{cf,r}$ **(s)**	r_N **at** $t^*_{cf,r}$ **(cm)**	t^{**} **(s)**	r_N **at** t^{**} **(cm)**
25	11.0	67.4	-----	-----
26	10.5	79.3	-----	-----
28	13.0	70.7	-----	-----
29	5.0	42.0	-----	-----
30	13.5	67.3	-----	-----
31	6.0	62.0	-----	-----
32	3.0	20.8	13.0	94.0
33	6.0	72.7	-----	-----
34	4.0	18.6	27.0	71.6
35	4.5	21.8	29.5	81.8

CHAPTER FIVE

INERTIAL PROPAGATION OF FLUID MUD UNDERFLOWS

In this chapter, results on the inertial propagation of fluid mud underflows (i.e. inertial gravity current phase of the fluid mud underflow) in which the inertia and buoyancy forces are the governing forces are described. Three widely used mathematical modeling approaches are chosen to model the inertial propagation of fluid mud gravity currents. Prediction capabilities of these models are evaluated using laboratory experiments. Evaluated models are at different levels of complexities. These models, from the simplest to the most complex are the force-balance model, box models for the compositional and suspension currents, and shallow water models for the compositional and suspension currents. All five models assume that the current is fully inviscid and the flow is governed by pure inertia-buoyancy balance. Therefore, laboratory experimental data for $t<t^{**}$ (i.e., discarding the viscous phase data) are used in this evaluation. For completeness, each model is briefly introduced, and appropriate references are provided for the detailed derivations. Part of the results and analysis presented in this chapter appeared in Chowdhury and Testik (2011a) and Chowdhury and Testik (2011b).

5.1 Mathematical Modeling of Inertial Propagation

This section describes the modeling approaches for the inertial propagation of gravity currents. The three selected modeling approaches – force-balance, box and shallow water modeling approaches – are briefly described for two-dimensional gravity currents in Section 5.1.1 and for radially axisymmetric gravity currents in Section 5.1.2

5.1.1 Two-dimensional Propagation

Consider a two-dimensional inertial (inviscid) gravity current of an incompressible fluid of density ρ_c propagating under an ambient fluid of lesser density ρ_a along a horizontal bottom, as shown in Fig. 5.1.

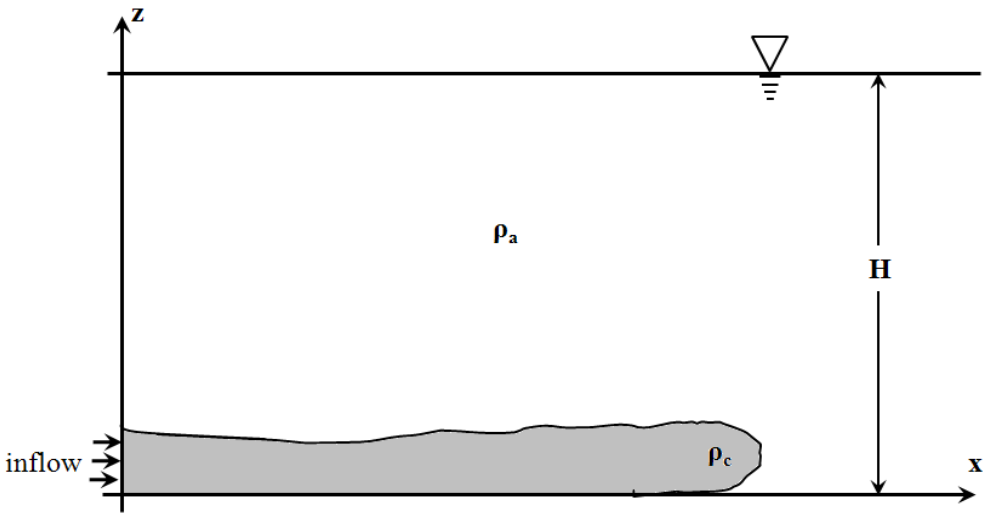

Figure 5.1. Schematic description of a two-dimensional gravity current

The current is generated due to the inflow of the denser fluid at the origin, $x = 0$ (see Fig. 5.1), and the volume of the fluid released per unit width, *V*, of the current at any instant of time, t, is given by:

$$V = qt^{\alpha}. \tag{5.1}$$

Here q (> 0) is a dimensional constant and α (≥ 0) is a constant that represents the type of released fluid volume source. The case of $\alpha = 0$ represents gravity currents originating because of the release of a fixed volume of fluid. The case of $\alpha = 1$ represents gravity currents that originate due to the release of a constant fluid volume flux, and the case of

$\alpha > 1$ represents gravity currents that form due to a leak or eruption which worsens with time (Ungarish, 2009). For $\alpha = 0$, q represents the initial volume released per unit width (i.e., $q = q_0 = V$).

In box and shallow water modeling approaches, a Froude number $\left(Fr = \frac{u_N}{\sqrt{g'_a h_N}} \right)$ condition at the current head is used as the boundary condition. Huppert and Simpson (1980) obtained two different *Fr* conditions for two-dimensional saline gravity currents with $\alpha = 0$ depending on the relative depth (h_n/H). For a current in shallow ambient which implies that the ratio of the current height and the depth of the ambient fluid is $0.075 \le \frac{h_n}{H} < 1$, the Fr condition is:

$$Fr = 0.5\left(\frac{h_n}{H} \right)^{-\frac{1}{3}}. \tag{5.2a}$$

For a current in deep ambient which implies that the ratio of the current height and the depth of the ambient fluid is $\frac{h_n}{H} < 0.075$, the Fr condition is:

$$Fr = 1.19. \tag{5.2b}$$

The Froude number conditions for the constant volume release gravity current (Eq. 5.2) are widely accepted and have been found to be in good agreement with experimental data. However, there have not been much experimental studies to determine such a Froude number condition for constant flux release experiments. For constant flux release (i.e. $\alpha = 1$), Ungarish (2009) stated that *Fr* = 0.8 yields fair agreements with available

experiments, while Bonnecaze et al. (1995b) mentioned that Huppert and Simpson (Unpublished Data, 1980) experimentally obtained Fr = 0.72 for $\frac{h_N}{H} \ll 1$. The reason for different Froude number conditions at the front of fixed volume and constant flux release gravity currents is the different flow dynamics of these two currents. Unlike fixed-volume release current, fluid continually flows into the head from the body of the constant flux release gravity current. Note that the Froude number conditions presented above are experimentally determined which include the effects of viscous drag and Reynolds stresses along the head of the current (Bonnecaze et al., 1995).

The force-balance, box model and shallow water model formulations for two-dimensional gravity currents are as follows.

5.1.1.1 Force-Balance Model

This simple single-equation model for the inertia-buoyancy propagation phase is based on the balance between the buoyancy and the inertia forces (see Huppert, 1982 for details). Neglecting the mixing process at the interface between the two fluids, the fluid volume defined in Eq. (5.1) for a rectangular, two-dimensional gravity current (see Fig. 5.1) can be related by an order-of-magnitude relationship, given below (Didden and Maxworthy, 1982; Huppert, 1982):

$$V = q\, t^{\alpha} \sim h_N(t) x_N(t). \tag{5.3}$$

Here, ~ implies an order-of-magnitude relationship, V is the volume released per unit width from the source, and h_N is the representative height of the current of length x_N.

From dimensional grounds and using Eq. (5.3), the order of magnitudes of the inertia, F_i, and buoyancy, F_g, forces for the two-dimensional propagation of a gravity current can be estimated as follows (Huppert, 1982):

$$F_g \sim \rho_c g_a' {h_N}^2 w \sim \frac{\rho_c g_a' q^2 t^{2\alpha} w}{{x_N}^2}. \tag{5.4}$$

$$F_i \sim \rho_c {u_N}^2 {h_N}^2 w \sim \frac{\rho_c q x_n w}{t^{2-\alpha}}. \tag{5.5}$$

Here, w is the width of the current, and ~ implies an order of magnitude relationship. Equating Eqs. (5.4) and (5.5), one obtains the expression for the front position of a two-dimensional gravity current as follows:

$$x_n = K_I (g_a' q)^{\frac{1}{3}} t^{\frac{\alpha+2}{3}}. \tag{5.6}$$

In Eq. (5.6), K_I is a constant of proportionality and its value should be obtained experimentally.

5.1.1.2 Box Model

Box models for two-dimensional propagation assume that the current evolves in a series of equal-area rectangles with uniform properties at any instant of time (Huppert, 1998). Two different types of box models are used to model the inertia-buoyancy dominated propagation of compositional and suspension gravity currents. Although fluid mud gravity currents are suspension-driven currents, given the very small settling velocity of the cohesive sediment and the experimental propagation length, the box model for compositional gravity currents is appropriate for the analysis. To ensure completeness, both models and their predictions, first for compositional currents and then

for suspension currents, are presented in this section. The box model solution for a compositional gravity current was obtained by combining two governing conditions (see the detailed derivation by Huppert and Simpson, 1980): (i) conservation of volume and (ii) Froude number condition at the current head (Eq. 5.2). In addition to these two governing conditions, the box model for the suspension gravity currents includes a third governing condition that incorporates the evolution of particle concentration due to deposition as the gravity current propagates (Gladstone and Woods, 2000). The box model parameterization for the front position of the two-dimensional propagation of a compositional gravity current is expressed below.

$$x_N = \left(\frac{3Fr}{\alpha + 2} \right)^{\frac{2}{3}} (g_a'^3 q)^{\frac{1}{3}} t^{\frac{\alpha+2}{3}}. \tag{5.7}$$

For the fixed volume release fluid mud gravity current experiments conducted in this investigation (Table 3.1), the shallow ambient Fr condition (Eq. 5.2a) is more applicable. The resulting parameterization for the front position of a compositional gravity current from the lock-gate is expressed below (Huppert and Simpson, 1980).

$$x_N = [\frac{7}{12} (g_a'^3 q_0 H^2)^{\frac{1}{6}} t]^{\frac{6}{7}}. \tag{5.8}$$

The box model solution for 2-D suspension currents from fixed-volume release by Dade and Huppert (1995a) is employed in this study. Omitting the details and derivations (see Dade and Huppert, 1995a), the dimensionless front position, X_N, for a suspension current in a shallow ambient is parameterized as follows.

$$X_N \approx \left(\frac{Q_{ND} D^2}{\sigma_s^6} \right)^{\frac{1}{7}} f_s(\sigma_s T). \tag{5.9}$$

Here, $\sigma_s = \left(\frac{D^{2/7} \beta}{6.9 C_s Q_{ND}^{6/7}} \right)^{7/13}$, $Q_{ND} (= q_0 / h_0^2)$ is the dimensionless 2-D volume behind the lock-gate, β ($w_s / \sqrt{g'_{a,0} h_0}$) is the dimensionless settling number, and $D (= H / h_0)$ is the dimensionless ambient water depth. C_s is a free parameter that is equal to unity for a compositional gravity current and varies for a suspension current based on a number of factors such as initial concentration and size of particles (Dade and Huppert, 1995). The expression for $f_s(\sigma_s T)$ is found in Appendix B of that article. It should be noted that in the calculations of Eq. (5.9) for fluid mud suspension currents investigated in this study, the hindered settling velocity (W_h) which is suitable for cohesive sediments and concentrated suspensions as suggested by Winterwerp and Kesteren (2004) and Coussot (1997) is used instead of the Stokes settling velocity ($W_s = (\rho_p - \rho_w) g d^2 / 18 \mu_w$; μ_w and ρ_w - dynamic viscosity and density of water, respectively) that is used by Dade and Huppert (1995) to model the experimental observations of non-cohesive suspension current of Bonnecaze et al. (1993). The hindered settling velocity can be expressed as (Winterwerp and Kesteren, 2004):

$$W_h = W_s (1 - \frac{k C_v}{100})^p. \tag{5.10}$$

Here k and p are empirical constants. We used k=1 and p=5.1 for estimating hindered settling velocity of the clay particles since they have been found to agree well with the experimental observations for cohesive sediments (see page 19 of Coussat, 1997).

5.1.1.3 Shallow Water Model

Shallow water models for gravity current propagation are based upon the Navier-Stokes solutions with the basic assumption that vertical accelerations are negligible so that the pressure field is purely hydrostatic. Unlike box models, shallow water models provide horizontal variations of current properties (such as height) (Kneller and Buckee, 2000). Depending upon the relative depth of the ambient fluid (h_N/H, see Huppert and Simpson, 1980), either one-layer or two-layer shallow water model formulations are employed (see Meiburg and Kneller, 2010; Ungarish, 2009). One-layer shallow water formulations neglect the motion of the overlying fluid; hence, they are more applicable for a gravity current with a deep ambient ($h_n/H<0.075$). Conversely, two-layer shallow water formulations account also for the dynamics of the overlying ambient fluid layer, and are more applicable for a gravity current with a shallow ambient ($0.075\leq h_n/H\leq 1$). In this investigation, only the evaluation of shallow water model solutions for fixed volume release experiments (Table 3.1) are attempted. Hence, the shallow water model for fixed volume release experiments is described below.

For the propagation of the compositional gravity currents in the inertia-buoyancy phase, a similarity solution for the one-layer shallow water model exists. However, a closed analytical solution for the two-layer model is unavailable and numerical solution is required. Based upon the reasoning in Section 5.1.1.2, compositional shallow water models are adequate for the analysis of the experimental observations in Table 3.1. To ensure completeness, both shallow water models and their predictions, first for

compositional currents and then for suspension currents, are presented in this section. Although the two-layer models are more applicable for the experimental conditions, one-layer shallow water models are employed in this investigation since they can provide similarity solution.

As detailed derivations and formulations of the one-layer model are found in Bonnecaze et al. (1993), a brief description is provided here. Similarity solution for the front position, x_n, is expressed as:

$$x_N = \left(\frac{27Fr^2}{12-2Fr^2} \right)^{\frac{1}{3}} (g_a'^3 q)^{\frac{1}{3}} t^{\frac{2}{3}}. \tag{5.11}$$

Given that the one-layer shallow water model assumes a deep ambient, a deep water Fr condition (Fr=1.19, from Eqn. 5.2b) is typically used in Eq. (5.11). In the front position calculation for the experiments in Table 3.1, the deep water Fr determined from experimental observations by Huppert and Simpson (1980) is employed and then the actual Fr measurements that correspond to the shallow ambient condition in the experiments is employed.

Because there is no exact solution for one- or two-layer shallow water models of suspension gravity currents, shallow water models for suspension currents are solved numerically (e.g., Bonnecaze et al., 1993). Hogg et al. (2000) and Harris et al. (2001) in two separate communications provided asymptotic solutions for shallow water models of suspension gravity currents. These solutions are obtained for the case when the settling velocity of the particles is much less than the initial velocity of propagation of these currents (Hogg et al., 2000). This is clearly the case for the experiments with cohesive

sediments as discussed earlier. Since the intent of the asymptotic solution by Harris et al. (2001) is to capture the flow behavior throughout the current's entire propagation within the inertia-buoyancy phase, rather than using Hogg's solution (with propagation time limits) Harris et al.'s solution (see Eq. 3.69 of Harris et al., 2001) is employed in this study. Please see Harris et al. (2001) for the asymptotic solution formulations in their entirety.

5.1.2 Radial Axisymmetric Propagation

In this section, the force-balance, box and shallow water modeling are described for radial axisymmetric gravity currents. Consider a horizontal, radial axisymmetric (cylindrical cross-section) inertial gravity current of an incompressible fluid of density ρ_c propagating under ambient fluid of lesser density ρ_a along a horizontal bottom, as shown in Fig. 5.2. The current is generated due to the inflow of the denser fluid at the origin, $r = 0$ and the z axis represents the axis of symmetry. The volume of the fluid released V at any instant of time t is given by:

$$V = Qt^{\alpha}. \tag{5.12}$$

Here, V [Length^3] is the volume released from the source and Q is a dimensional constant with dimension [Length^3.Time$^{-\alpha}$]. For $\alpha = 0$, $Q = V$ represents the initial fixed volume released and the dimension is [Length^3]. For $\alpha = 1$, Q is the constant flux of fluid and the dimension is [L^3T^{-1}].

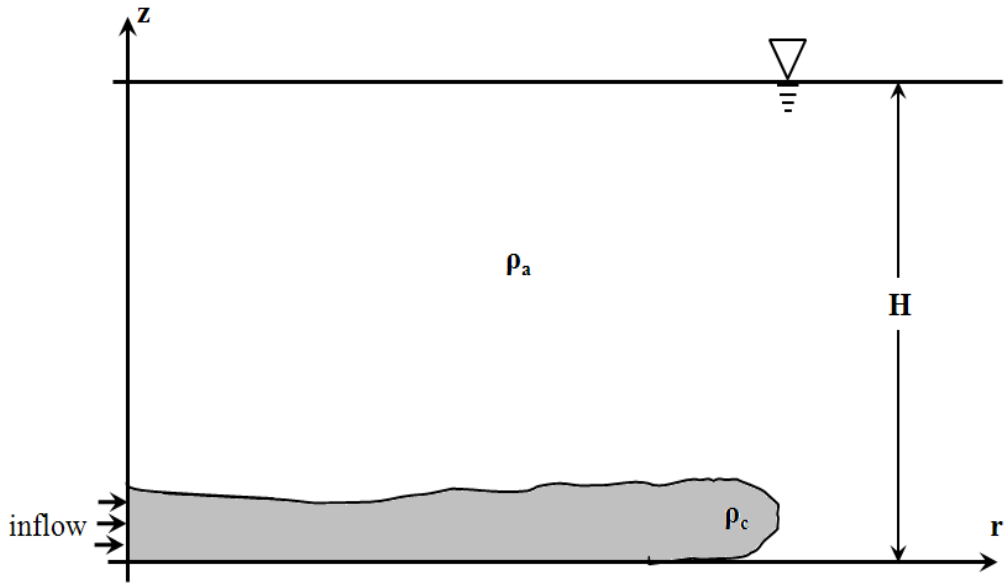

Figure 5.2. Schematic description of radially axisymmetric gravity current. *z* axis represents the axis of symmetry.

5.1.2.1 Force-Balance Model

Following a procedure similar to that of Section 5.1.1.1, and neglecting the mixing process at the interface between the two fluids, the order of magnitude of the fluid volume a cylindrical, axisymmetric gravity current can be described by the following expression (Didden and Maxworthy, 1982; Huppert, 1982):

$$V = Qt^{\alpha} \sim h_N r_N{}^2. \tag{5.12}$$

Here, h_N is the representative height of the current of length r_N. For the radially axisymmetric propagation (Huppert, 1982):

$$F_g \sim \frac{\rho_c g_c' Q^2}{r_N^3} t^{2\alpha}. \tag{5.13}$$

$$F_i \sim \frac{\rho_c Q r_N}{t^{2-\alpha}}. \tag{5.14}$$

Equating Eqs. (5.13) and (5.14), one can obtain the expression for the front position of a radially axisymmetric gravity current as follows:

$$r_N = K_I (g_a' Q)^{\frac{1}{4}} t^{\frac{\alpha+2}{4}}. \tag{5.15}$$

In Eq. (5.15), K_I is a constant of proportionality; its value should be obtained experimentally.

5.1.2.2 Box Model

In the box modeling approach for gravity flows, the gravity flow is considered to evolve as an axisymmetric cylinder that has uniform properties at any instant in time. The first governing equation of the box model is provided by the volume continuity requirement expressed as:

$$\pi r_N^2 h_N = V = Q t^{\alpha}. \tag{5.16}$$

Note that if the experiment is conducted in a sector tank with an angle Φ (e.g. Bonnecaze et al., 1995b), Eq. (5.16) should be modified to:

$$\frac{\Phi}{2\pi} \pi r_N^2 h_N = V = Q t^{\alpha}. \tag{5.17}$$

When the flow spread uniformly in all direction, the pre-factor $\frac{\Phi}{2\pi}$ is unity. Using this boundary condition and a *Fr* number condition in the head, the box model solution for the

propagation of compositional axisymmetric gravity currents can be expressed as (Huppert and Simpson, 1980; Dade and Huppert, 1995b; Ungarish, 2009):

$$r_N = \left(\frac{4Fr}{\alpha+2}\right)^{\frac{1}{2}} \left(\frac{g'_a Q}{\pi}\right)^{\frac{1}{4}} t^{\frac{\alpha+2}{4}}. \tag{5.18}$$

The same Froude number condition mentioned for two-dimensional gravity currents (Eq. 5.2) is generally applied for radially axisymmetric gravity currents considering a radially axisymmetric gravity currents is locally two-dimensional (see Huppert and Simpson, 1980).

5.1.2.3 Shallow Water Model

The similarity solution of the shallow water modeling approach for a radially axisymmetric gravity current provides the radial front position, r_N of the current as follows (Bonnecaze et al., 1995b):

$$r_N = C\left(\frac{g'_a Q}{h_0^4 \Phi}\right)^{\frac{1}{4}} \left(\frac{h_0^4}{g'_a}\right)^{\frac{\alpha+2}{4}} t^{\frac{\alpha+2}{4}}. \tag{5.19}$$

Here h_0 is the characteristic length scale for a particular gravity current and C is a constant which can be obtained analytically for $\alpha = 0$. When Fr = 1.19, C is 1.29. However, C cannot be determined analytically for $\alpha > 0$. Hence, a continuous similarity solution does not exist for axisymmetric gravity current for $\alpha > 0$ (Grundy and Rottman, 1986; Bonnecaze et al., 1995b). This leaves the box-model approximation (Eq. 5.18) as the only practical analytical solution for axisymmetric gravity currents when $\alpha > 0$ at the present state of knowledge (Ungarish, 2009).

5.2 Experimental Evaluation of the Inertial Mathematical Models

In this section, predictive capabilities of the mathematical models for inertial propagations of fluid mud gravity currents are evaluated using laboratory experiments. First, the evaluation is performed for the models for two-dimensional gravity currents with the two-dimensional fluid mud gravity current experiments (Table 3.1 and 3.2) in Section 5.2.1 and then the radially axisymmetric experimental data of fluid mud gravity currents (Table 3.3) are used to evaluate the radially axisymmetric inertial models in Section 5.2.2.

5.2.1 Two-dimensional Fluid Mud Gravity Currents

First, the prediction capabilities of force-balance, box model and shallow water models are compared with the inertial propagation of fixed volume release fluid mud gravity currents (Table 3.1) in Section 5.2.1.1, and then the predictive capabilities of those models are compared with the inertial propagation of constant flux release experiments (Table 3.2) in Section 5.2.1.2.

5.2.1.1 Constant Volume Release Experiments

The front position predictions by the force-balance model expressed in Eq. (5.6) with α=0 and the experimental observations for the fixed volume release experiments (see Table 3.1) are presented in Fig. 5.3. Here, different symbols represent the experimental data for fluid mud suspensions with different initial concentrations and solid lines represent the predictions for the corresponding experiments.

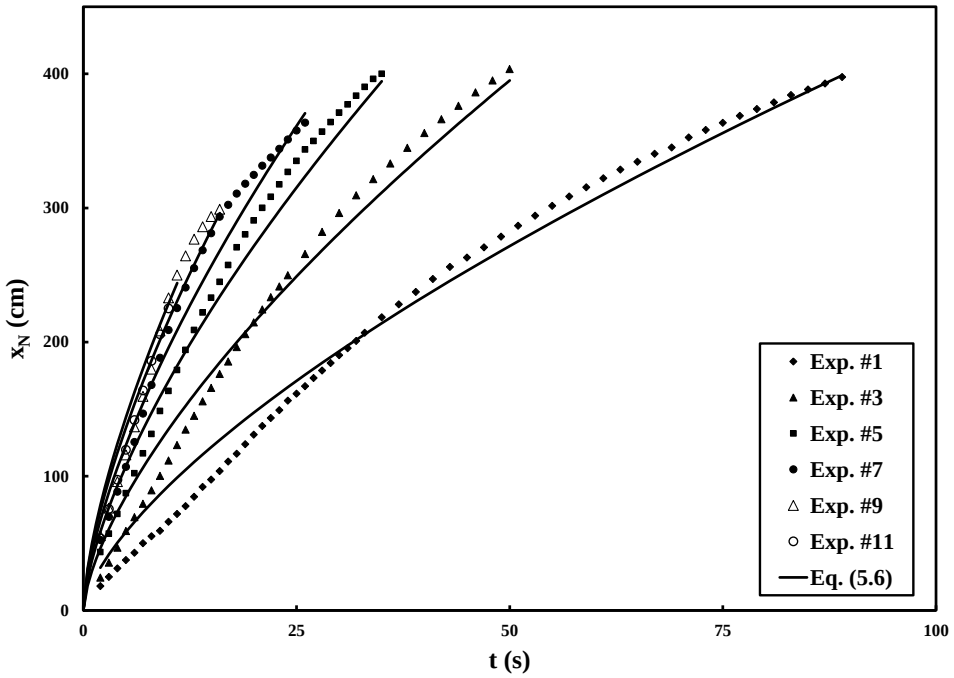

Figure 5.3. Comparison of the current front position predictions by the force-balance model [solid lines, Eq. (5.6)] with the 2-D constant volume release experimental data (Table 3.1).Every alternate experiment is shown in the figure for clarity purposes. Symbols represent the data from the experiments tabulated in Table 3.1 and are defined in the legend.

As is evident, the predictions from this simple model agree well with the experimental observations, except for the earlier times of the current propagation. The discrepancy in the earlier phases of the propagation is due to the omission of ambient water dynamics in the model. As soon as the gate is lifted in a lock-exchange set-up, an initial counter-flow of ambient water occurs above the forming fluid-mud current which then hits the end-wall and is reflected back, forming a bore (Rottman and Simpson, 1983). This bore affects the current until its energy is dissipated (i.e., till the end of slumping phase). Clearly, the simple expression in Eq. (5.6) is incapable of modeling this complex phenomenon. The best fit value of K_I for all of our experiments is calculated

to be 1.14, except for Exp. # 11 and 12. Average R^2 value for Exp. # 1-10 with K_I = 1.14 is 0.974 (see Table 3) and the average R^2 value decreases to 0.876 for the preset value of K_I=1 that represents an exact balance between the inertia and buoyancy forces. K_I value being larger than this preset value is partly due to the ambient water dynamics in the vicinity of the gate as described above and partly due to viscous effects. Though initially small, the viscous effects steadily accumulate as the current propagates.

In Fig. 5.4, the front position predictions by the compositional box model solution expressed in Eq. (5.8) and the experimental observations are presented. Here we see that for most part of the current propagation, the predictions of the compositional box model closely agree with the experimental data whereas at the later propagation times, the compositional box model over-predicts the current front position. This over-prediction is because the gravity current begins to experience increasing viscous affects while the box model is constructed with the inviscid flow assumption. At these later propagation times, the current flow is not purely dominated by the inertia-buoyancy balance; rather a relatively small magnitude viscous force retards the current propagation. Note that, unlike force-balance expression [Eq. (5.6)], the compositional box model solution has no adjustable parameter. Therefore, without any adjustable parameters, the compositional box model agrees well with the experimental observations for much of the current propagation.

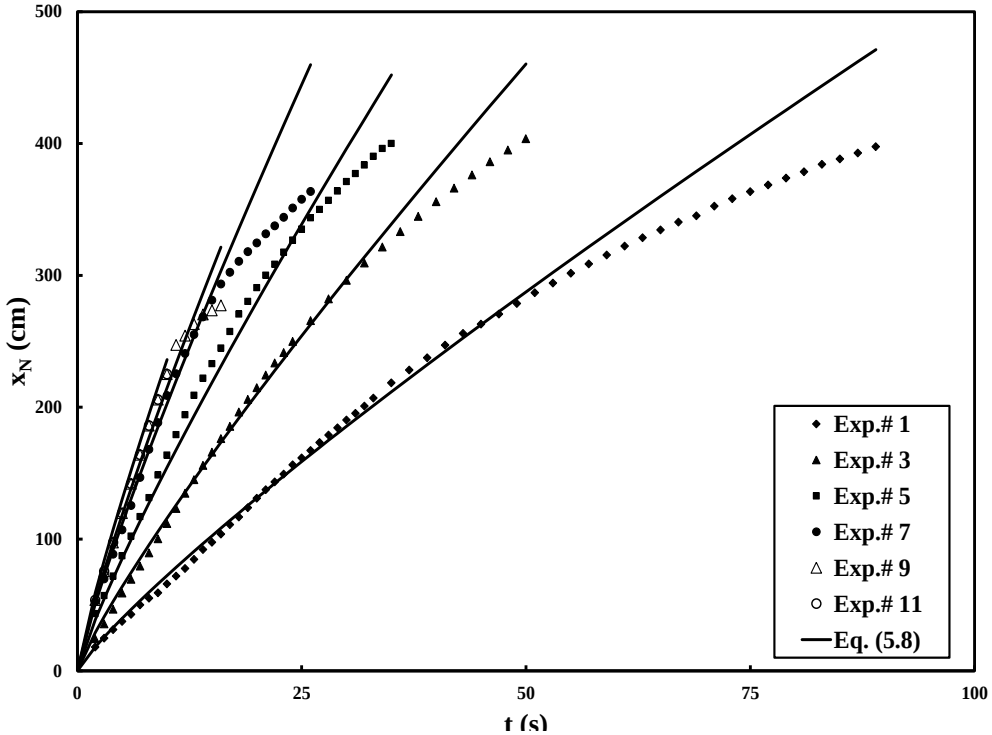

Figure 5.4. Comparison of the current front position predictions by the compositional box model (solid lines, Eq.5.8) with the 2-D constant volume release experimental data (Table 3.1). Every alternate experiment is shown in the figure for clarity purposes. Symbols represent the data from the experiments tabulated in Table 3.1 and are defined in the legend.

A comparison of the front position predictions by the box model solution for suspension currents (Eq. 5.9) and our experimental observations for fluid mud suspension currents is given in Fig. 5.5. Interestingly, the best fit value for the free parameter C_s with coefficient of correlation values, $R^2 > 0.92$, is 1 for all of the experiments. This observation confirms our earlier statement that fluid mud gravity currents behave like compositional gravity currents for small propagation times. Since the best C_s fit value is unity for suspension-box model solution, the prediction curves of the model are similar to that of compositional counterparts.

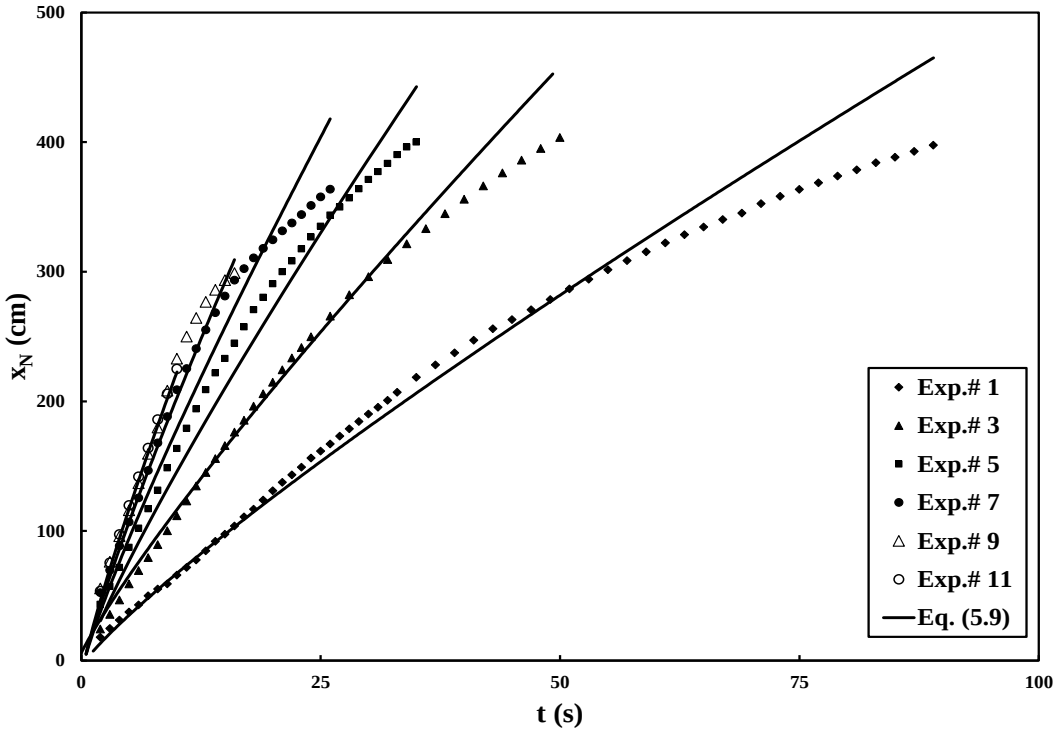

Figure 5.5. Comparison of the current front position predictions by the suspension box model (solid lines, Eq. 5.9) with the 2-D constant volume release experimental data (see Table 3.1). Every alternate experiment is shown in the figure for clarity purposes. Symbols represent the data from the experiments tabulated in Table 3.1 and are defined in the legend.

The front position predictions by the one-layer shallow water model expressed in Eq. (5.11) with Fr = 1.19 and experimental observations are presented in Fig. 5.5a. Here, the model predictions significantly over-predict the experimental observations, mainly due to the use of deep water Fr condition. If an Fr value of 0.8 is used, which is a more representative value for our shallow ambient experiments, the model predictions improve significantly (see Fig. 5.6b). The discrepancy observed here between the model predictions and the experimental data at the initial propagation times corresponds to the slumping phase of propagation in which the overlying water is very dynamic. The one-layer shallow water model does not consider this phenomenon.

The predictions of suspension shallow water model by Harris et al.'s solution and our experimental observations are presented in Fig. 5.7, which shows a close agreement between the predictions and the overall experimental data trend. As in the case of one-layer compositional shallow water model predictions, the discrepancy between the predictions and the data are attributable to the use of the deep water *Fr* condition. The use of a more representative shallow ambient *Fr* condition is quite complex in Harris et al.'s solution and is out of the scope of this study.

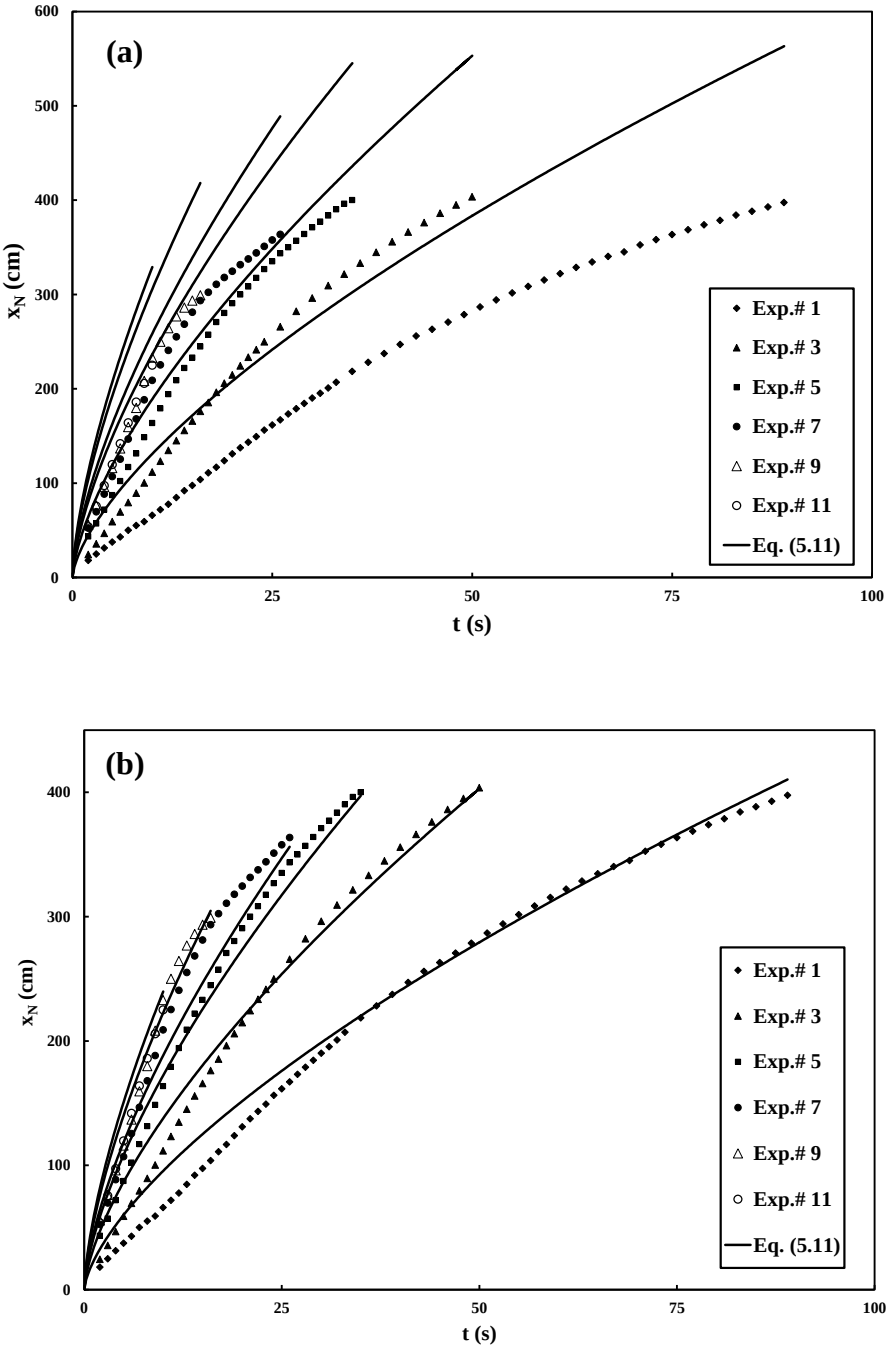

Figure 5.6. Comparison of the current front position predictions by the compositional shallow water model (solid lines, Eq. 5.11) using two different Fr conditions [(a) Fr = 1.19, and (b) Fr = 0.8] with the 2-D constant volume release experimental data. Every alternate experiment is shown in the figure for clarity purposes. Symbols represent the data from the experiments tabulated in Table 3.1 and are defined in the legend.

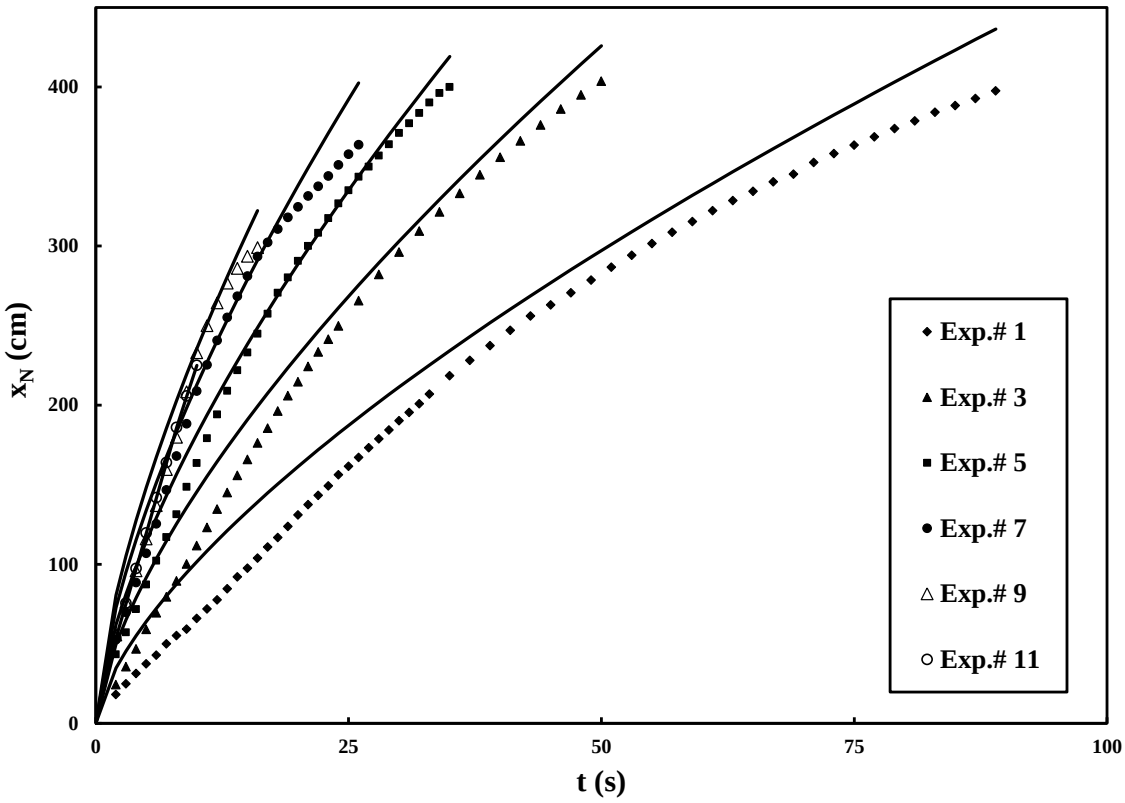

Figure 5.7. Comparison of the current front position predictions by the suspension shallow water model (solid lines) using deep ambient Fr condition (i.e., Fr = 1.19) with the 2-D constant volume release experimental data. Every alternate experiment is shown in the figure for clarity purposes. Symbols represent the data from the experiments tabulated in Table 1 and are defined in the legend.

5.2.1.2 Constant Flux Release Experiments

From Fig. 4.8 and the transition time in Table 4.3, it is evident that most fluid mud gravity currents (except Exps. #13 and 14) from the constant flux release experiments made transition from jet to viscous phase either bypassing the inertial phase or after propagating a very short duration (≈1-3 seconds) in the inertial phase. Therefore, only the inertial propagation of Exps. #13 and 14 are used to evaluate the inertial models. Among the three models, only the box model solution is used for the evaluation. For a

constant flux release two-dimensional gravity current, a closed-from self-similarity solution is not available in the literature though Ungarish (2009) mentioned that it can be obtained and hence, is not attempted here. In addition, unlike fixed volume release case, there is no widely accepted Fr number condition for constant flux release two-dimensional gravity currents. As noted earlier, Ungarish (2009) suggested Fr = 0.8 while Huppert and Simpson found Fr = 0.72 for $\frac{h_N}{H} \ll 1$ in an unpublished study. Therefore, we a best-fit Froude number for the inertial propagation of constant flux release fluid mud gravity currents is obtained in this study. Since Froude number is used as a free-parameter in implementing the box model solution, box-model solution turns into a form of force-balance expression and hence, the original force-balance solution is also not attempted. Fig. 5.8 shows the comparison of the box model prediction with the experimental observations of constant flux release two-dimensional fluid mud gravity currents. In Fig. 5.8a, the origin of the inertial propagation was considered at the inlet position while in Fig. 5.8b, the jet portions of the curves are omitted and the source is shifted to a virtual origin at the jet transition position $\left(x_{cf}^{*}, t_{cf}^{*} \right)$. As it can be seen from Fig. 5.8, when the jet portion is omitted, the prediction of the model agrees better with the experimental data.

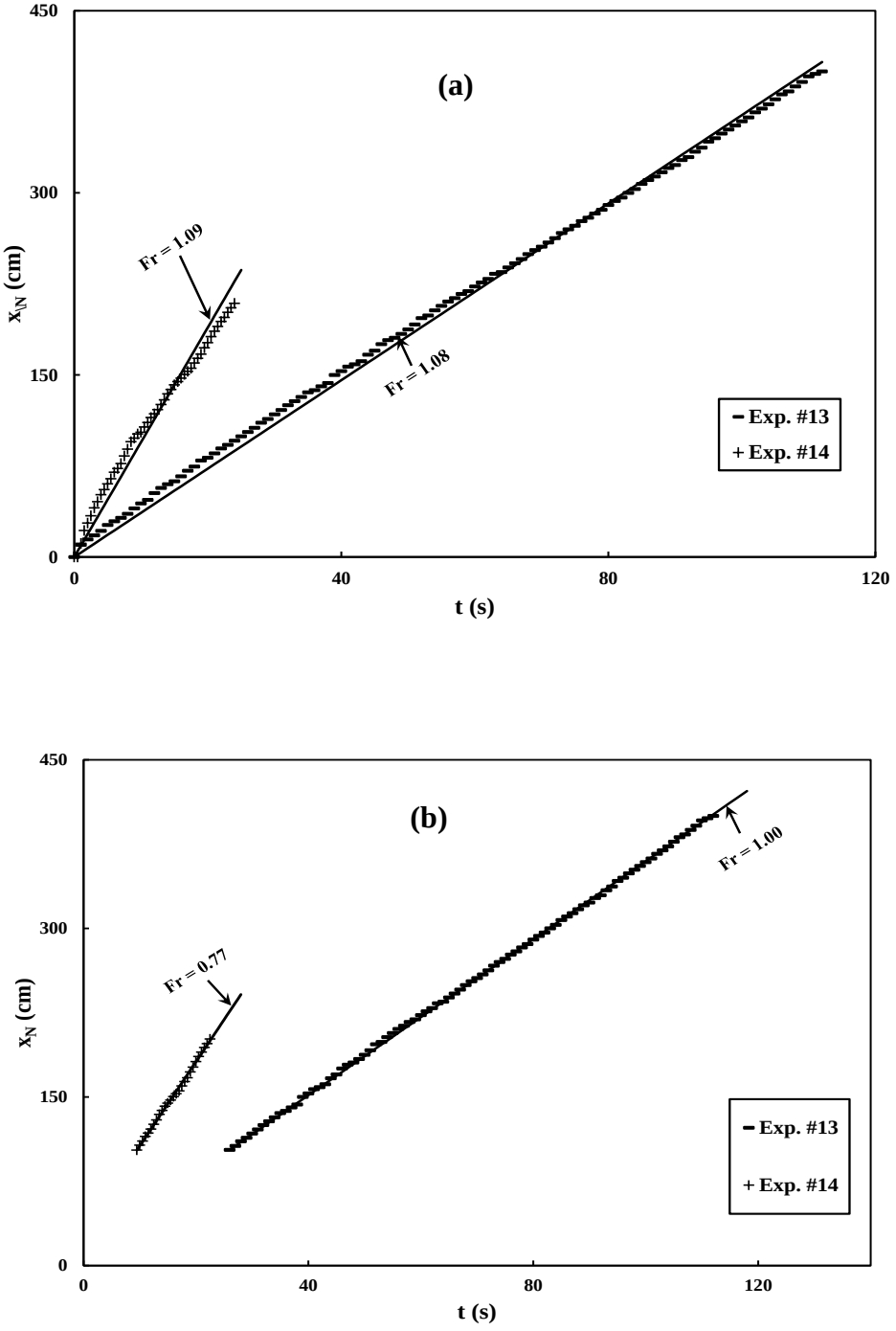

Figure 5.8. Comparison of the current front position predictions by the compositional box model (solid lines, Eq. 5.8) with the 2-D constant flux release experimental data (Table 3.2). a) Source at inlet and b) source at the jet transition position. Symbols represent the data from the experiments tabulated in Table 3.2 and are defined in the legend.

5.2.2 Radial Axisymmetric Fluid Mud Gravity Currents

In this investigation, the radial fluid mud gravity currents were generated from constant flux release of fluid mud. As is stated in Section 5.1.2.3, there is no analytical solution of the shallow water model for $\alpha = 1$. In addition, there is no widely accepted Froude number condition for constant flux release experiments to implement in the box model solution. Therefore, it is more effective to implement the Froude number in the box model solution (Eq. 5.18) as a free parameter and obtain a best fit Froude number condition based upon the experimental data. In this case, it is not worthwhile to employ a force-balance model. Hence, in this study, only box model solution with the best-fit Fr condition is used to predict the radial fluid mud gravity current experimental observations. The experimentally best-fit Froude numbers for constant flux release experiments (both two-dimensional and radial) are tabulated in Table 5.1. It can be seen that the experimentally obtained best-fit Froude number values are much higher than the suggested values of Huppert and Simpson (Unpublished data, 1980) and Ungarish (2009).

The predictions of the box model solution and the radially axisymmetric fluid mud gravity currents experimental data are plotted in Fig. 5.9. Please note that the jet portion is not deleted in this plot. Hence, except Exp. #33 in Fig. 5.9b, initially the model under-predicts the experimental data, but then the model predictions are observed to be in good agreement with the data in the inertial propagation phase. In Exp. #33, current

transitioned into viscous phase approximately at 12 seconds and hence, the inviscid box model over predicts the viscous propagation in this experiment.

Table 5.1. Best-fit Froude number for constant-flux released fluid mud underflow experiments

Exps. #	***Fr* #**	**Experiment Type**
13	1.09	Two-dimensional experiments
14	1.08	
26	1.21	Radial Experiments
27	1.05	
28	0.92	
29	0.99	
30	0.95	
31	0.99	
32	1.05	
33	0.82	
34	1.22	

.

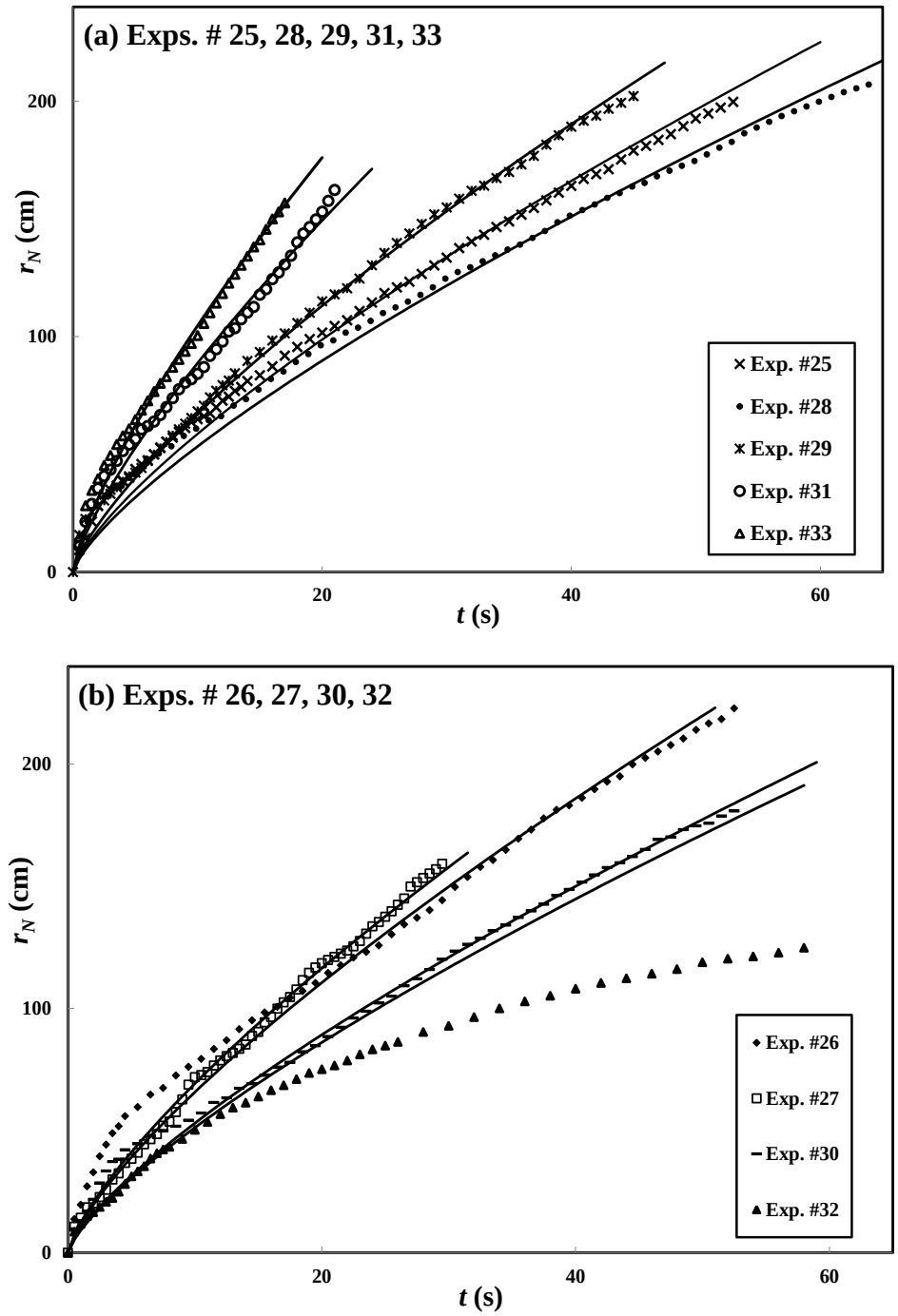

Figure 5.9. Comparison of the radial current front position predictions by the compositional box model (solid lines, Eq. 5.18) with the radial constant flux release experimental data (Table 3.3). Presented in two separate graphs for clarity purposes. Symbols represent the data from the experiments tabulated in Table 3.3 and are defined in the legend.

CHAPTER SIX

VISCOUS PROPAGATION OF FLUID MUD UNDERFLOWS

This Chapter elucidates the viscous propagation of the fluid mud underflows (i.e. viscous gravity current part of the fluid mud underflow) in which the viscous and buoyancy forces are the governing forces. Fluid mud gravity currents with sufficiently high levels of concentration (see Fig. 3.7) have a non-Newtonian rheology and their viscous propagation characteristics vastly differ from the Newtonian gravity currents. As discussed in Chapter 2, the numbers of experimental and theoretical studies on viscous gravity currents have been far less than that of inertial counterparts. Even among the available studies on the viscous propagation, most of them are on Newtonian viscous gravity current, while fluid mud gravity current is non-Newtonian. There are no viscous force-balance and box model solutions available for non-Newtonian gravity currents. Hence, force-balance and box model solutions for the both rectangular two-dimensional and radial axisymmetric viscous non-Newtonian gravity currents are derived in detail in this Chapter. There are recent self-similarity solutions based on lubrication theory for rectangular two-dimensional (Di Federico et al., 2006a) and cylindrical axisymmetric (Di Federico et al., 2006b) viscous propagation of a non-Newtonian gravity current that have not been laboratory tested before this doctoral research. These three models - non-Newtonian force-balance, box and lubrication approximation models- are laboratory tested to evaluate their predictive capabilities in Section 6.2. Part of the results and

analysis presented in this chapter appeared in Chowdhury and Testik (2011a) and under review in Chowdhury and Testik (2011c).

6.1 Mathematical Modeling of Viscous Propagation

This section describes three mathematical modeling approaches (force-balance, box and lubrication approximation) for viscous propagation of a non-Newtonian gravity current. First, these three modeling approaches are described for a rectangular, two-dimensional viscous current in Section 6.1.1 and then, they are described for a radial axisymmetric viscous non-Newtonian current in Section 6.1.2. A theoretical analysis for the resulting expressions of three modeling approaches is provided in Section 6.1.3.

6.1.1 Two-Dimensional Non-Newtonian Gravity Current

Following the same procedure of Section 5.1, consider a two-dimensional viscous gravity current of an incompressible non-Newtonian fluid of density ρ_c propagating under a Newtonian ambient fluid of lesser density ρ_a along a horizontal bottom. The surface tension effects along the interface and nose of the current as well as the entrainment of the ambient fluid into the gravity current are considered negligible. The current is generated due to the inflow of the denser fluid at the origin, $x = 0$ (see Fig. 5.1), and the volume of the fluid released per unit width V of the current at any instant of time *t* is given by Eq. (5.1).

6.1.1.1 Force-Balance Model

A force-balance expression for the front position in the viscous-buoyancy phase of a non-Newtonian gravity current can be obtained by equating the order of magnitudes of buoyancy and viscous forces acting on the current. In this derivation, a similar procedure by Didden and Maxworthy (1982) is followed by considering the non-Newtonian rheological properties of fluid mud suspensions expressed by Ostwald power-law constitutive equation (Eq. 2.2) as follows.

Neglecting the mixing process at the interface between the two fluids, the fluid volume defined in Eq. (5.1) for a rectangular, two-dimensional gravity current can be related by an order-of-magnitude relationship, given by Eq. (5.3). The order of magnitude of the viscous force acting on a 2-D non-Newtonian gravity current, based on the Ostwald power-law constitutive relationship (Eq. 2.2), can be obtained as follows.

$$F_v \sim m\left(\frac{U_N}{h_N}\right)^n x_N w \sim m x_N{}^{2n+1} q^{-n} t^{-n(\alpha+1)} w. \tag{6.1}$$

Equating Eqs. (5.4) and (6.1), one can obtain the following force-balance relationship for the current front position.

$$x_N = K_v\, q^{\frac{2+n}{2n+3}} \left[\frac{\rho_c g_c'}{m}\right]^{\frac{1}{2n+3}} t^{\frac{\alpha(n+2)+n}{2n+3}}. \tag{6.2}$$

Here K_v is a free parameter included based upon dimensional considerations and it needs to be determined experimentally. Note that reduced gravity based on current density, g_c' $\left(g_c' = g(\rho_c - \rho_a)/\rho_c\right)$ is usually used for viscous analysis of the gravity current instead

reduced gravity in terms of ambient density, g'_a. Following this convention, g'_c will be used for this chapter.

6.1.1.2 Box Model Solution

Ungarish (2009) described a box model solution for quantifying the viscous propagation of Newtonian gravity currents that has not yet been evaluated experimentally. In this section, a box model solution for non-Newtonian gravity currents is derived, which will be evaluated via laboratory observations.

In box modeling approach, the current is approximated by a rectangular box of length x_n and height h_N at a given propagation time t as shown in Fig. 6.1 (a simplified representation of Fig. 5.1). With this assumption on the shape of the gravity current, two governing equations are employed to obtain box model solutions.

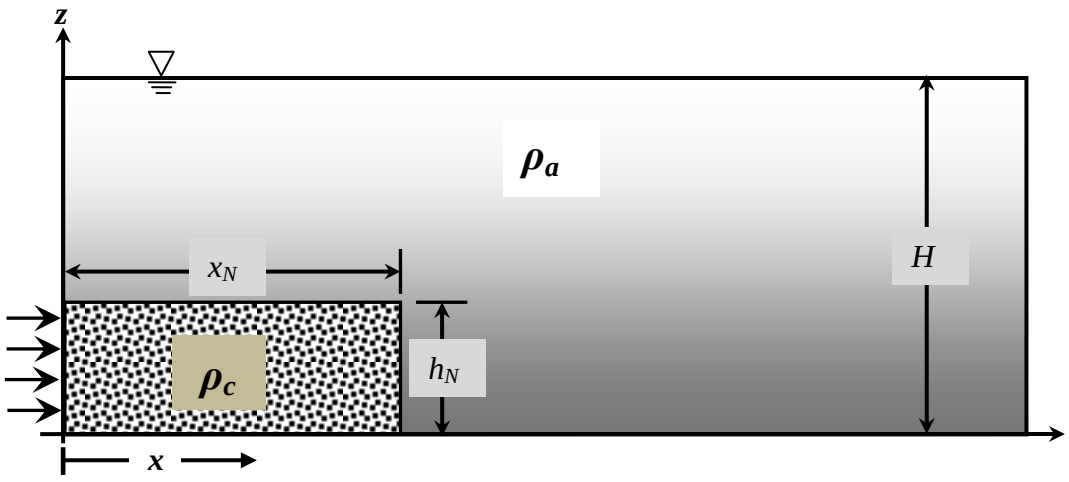

Figure 6.1. Conceptual sketch of the box model. The source of the current is located at x=0. Symbols: H – ambient fluid height; ρ_c and ρ_a - densities of the current and the ambient fluids, respectively; h_n and x_n – height and front position of the gravity current at a given time, respectively.

The first governing equation of the box model is provided by the volume continuity requirement provided in Eq. (6.3) based upon Eq. (5.1).

$$V = q\, t^{\alpha} = h_N x_N . \tag{6.3}$$

The second governing equation involves a dynamic consideration which can be obtained by equating the expressions of the driving buoyancy force and retarding viscous force (Ungarish, 2009). Assuming a hydrostatic pressure distribution, the driving buoyancy force per unit width, F_B, of the propagating current can be expressed as:

$$F_B = \frac{1}{2}(\rho_c - \rho_a) g h_N^2 = \frac{1}{2}\rho_c g_c' h_N^2 . \tag{6.4}$$

Using Eq. (2.2), the viscous force per unit width, F_v, is expressed as:

$$F_v = \frac{1}{n+1} m \left(\frac{u_N}{h_N} \right)^n x_N . \tag{6.5}$$

The second governing equation for the viscous propagation of a non-Newtonian gravity current is then can be obtained by equating Eq. (6.4) and (6.5) as:

$$u_N = \frac{dx_N}{dt} = \left[\frac{n+1}{2} \frac{\rho_c g_c' h_N^{2+n}}{m x_N} \right]. \tag{6.6}$$

Please note that this boundary condition of (6.6) appears inconsistent with the box model simplification at x=0 as observed by Ungarish (2009). However, it is assumed that this discrepancy has negligible effect on the global balances in Eqs. (6.4) and (6.5). Combining Eqs. (6.4) and (6.5) and performing a time integration yields the box model expression for the front position of a non-Newtonian gravity current as follows:

$$x_N = \left(\frac{(2n+3)^n (n+1)}{2(\alpha+\alpha n+n)^n} \right)^{\frac{1}{2n+3}} q^{\frac{2+n}{2n+3}} \left(\frac{\rho_c g_c'}{m} \right)^{\frac{1}{2n+3}} t^{\frac{n+\alpha(n+2)}{2n+3}}. \quad (6.7)$$

The expression for the height of the current, h_N, can be obtained by combining Eqs. (6.3) and (6.7), which is expressed as:

$$h_N = \left(\frac{(2n+3)^n (n+1)}{2(\alpha+\alpha n+n)^n} \right)^{-\frac{1}{2n+3}} q^{\frac{n+1}{2n+3}} \left(\frac{\rho_c g_c'}{m} \right)^{-\frac{1}{2n+3}} t^{\frac{n+\alpha(n+1)}{2n+3}}. \quad (6.8)$$

These box model parameterizations [Eqs. (6.7) and (6.8)] provide current position and height predictions for the viscous propagation of non-Newtonian compositional gravity currents originating from a source with any α value. Note that for n = 1, Eq. (6.7) and (6.8) simplify to the box model solution of Ungarish (2009) for Newtonian viscous gravity currents.

6.1.1.3 Lubrication Theory

Extending the work of Huppert (1982a) that is for Newtonian viscous gravity currents, Di Federico et al. (2006a) recently provided self-similarity solution from one-layer lubrication theory for rectangular two-dimensional viscous propagation of a non-Newtonian gravity current. The lubrication theory solution is the viscous counterpart of the shallow water model solution that is for inertial gravity currents where the main assumption is the vertical velocity is negligibly small as compared to the horizontal velocity and hence, the pressure is hydrostatic (Ungarish, 2009). In the solution by Di Federico et al. (2006a), the rheological properties of the intruding non-Newtonian fluid are represented by the Ostwald power-law constitutive relationship. Please note that this

solution has not been experimentally tested and in this Chapter, we will evaluate the predictive capabilities of this model experimentally.

The self-similarity solution for the front position, x_N, of the two-dimensional viscous propagation of a non-Newtonian gravity current is (Di Federico et al., 2006a):

$$x_n = \eta_N \left(\frac{n}{2n+1} \right)^{\frac{n}{2n+3}} q_{sw}^{\frac{1}{2}} \left(\frac{\rho_c g_c' q_{sw}^{\frac{1}{2}}}{m} \right)^{\frac{\alpha(n+2)+n}{n(2n+3)}} t^{\frac{\alpha(n+2)+n}{2n+3}}. \tag{6.9}$$

Here, η_N is the similarity variable at the nose of the current and it needs to be determined by numerically integrating Eqs. (15) and (16) of Di Federico et al. (2006a) for $\alpha \neq 0$ (the interested reader is kindly referred to Di Federico et al., 2006), and q_{sw} is a constant related to volume released per unit width, V, expressed as:

$$V = q_{sw}^{\frac{2n+\alpha}{2n}} t^{\alpha} \left(\frac{\rho_c g_c'}{m} \right)^{\frac{\alpha}{n}}. \tag{6.10}$$

Using Eqs. (5.1) and (6.10), one can manipulate Di Federico's front position expression (Eq. 6.9) into the same functional form of the force-balance expression in Eq. (6.4) and the box model solution in Eq. (6.7) as follows.

$$x_N = \eta_N \left(\frac{n}{2n+1} \right)^{\frac{n}{2n+3}} q^{\frac{2+n}{2n+3}} \left[\frac{\rho_c g_c'}{m} \right]^{\frac{1}{2n+3}} t^{\frac{\alpha(n+2)+n}{2n+3}}. \tag{6.10}$$

6.1.2 Radial Axisymmetric Non-Newtonian Gravity Current

In this section, the force-balance, box and lubrication theory models are described for cylindrical axisymmetric non-Newtonian gravity currents. Consider a horizontal, radially axisymmetric viscous gravity current of an incompressible non-Newtonian fluid

of density ρ_c propagating under a Newtonian ambient fluid of lesser density ρ_a along a horizontal bottom (see Fig. 5.2). The current is generated due to the inflow of the denser fluid at the origin, $r = 0$ and the z-axis represents the axis of symmetry.

6.1.2.1 Force-Balance Model

Following the similar procedure of Section 6.1.1.1 and neglecting the mixing process at the interface between the two fluids, the order of magnitudes of the fluid volume for a radially axisymmetric gravity current can be expressed by Eq. (5.12). The order of magnitude of the viscous force acting on a cylindrical axisymmetric gravity current, based on the Ostwald power-law constitutive relationship (Eq. 2.2), can be expressed as follows.

$$F_v \sim m\left(\frac{U_N}{h_N}\right)^n r_N{}^2 \sim m r_N{}^{3n+2} Q^{-n} t^{-n(\alpha+1)}. \tag{6.11}$$

Equating order of magnitude of buoyancy (Eq. 5.13) and viscous (Eq. 6.11) forces, one can obtain the following force-balance relationship for the current front position.

$$r_N = K_v Q^{\frac{2+n}{3n+5}} \left[\frac{\rho_c g_c'}{m}\right]^{\frac{1}{3n+5}} t^{\frac{\alpha(n+2)+n}{3n+5}}. \tag{6.12}$$

Here K_v is a free parameter included based upon dimensional considerations and its value needs to be determined experimentally.

6.1.2.2 Box Model

In box modeling approach for radially axisymmetric gravity current, the current is approximated by a cylindrical box of radius r_N and height h_N at a given propagation time t

as shown in Fig. 6.1. Please note that, for radially axisymmetric case, x and x_N will be replaced by r and r_N and the z-axis represents axis of symmetry. The first governing equation of the box model is provided by the volume continuity requirement expressed by Eq. (5.16).

The second governing equation involves a dynamic consideration which can be obtained by equating the expressions of the driving buoyancy force and retarding viscous force (Ungarish, 2009). Assuming a hydrostatic pressure distribution, the driving buoyancy force per unit width, F_B, of the propagating current is expressed as:

$$F_B = \frac{1}{2}(\rho_c - \rho_a) g r_N h_N^2 = \frac{1}{2}\rho_c g_c' r_N h_N^2. \tag{6.13}$$

Using Eq. (2.2), the viscous force per unit width, F_v, is expressed as:

$$F_v = \frac{m}{n+2}\left(\frac{u_N}{h_N}\right)^n r_N{}^2. \tag{6.14}$$

The front condition for the viscous propagation of a non-Newtonian gravity current is then obtained by equating Eq. (6.13) and (6.14) as:

$$u_N = \frac{dr_N}{dt} = \left[\frac{n+2}{2}\frac{\rho_c g_c' h_N^{2+n}}{m r_N}\right]^{\frac{1}{n}}. \tag{6.15}$$

Combining Eqs. (5.16) and (6.15) and performing a time integration yields the box model expression for the front position of a non-Newtonian gravity current, which is expressed as:

$$r_N = \left(\frac{(3n+5)^n (n+2)}{2(n+\alpha n+2\alpha)^n}\right)^{\frac{1}{3n+5}} \left(\frac{Q}{\pi}\right)^{\frac{2+n}{3n+5}} \left(\frac{\rho_c g_c'}{m}\right)^{\frac{1}{3n+5}} t^{\frac{n+\alpha(n+2)}{3n+5}}. \tag{6.16}$$

The expression for the height of the current, h_N, can be obtained by combining Eqs. (5.16) and (6.16), which is expressed as:

$$h_N = \left(\frac{(3n+5)^n (n+2)}{2(n+\alpha n+2\alpha)^n} \right)^{-\frac{1}{3n+5}} \left(\frac{Q}{\pi} \right)^{\frac{2+n}{3n+5}} \left(\frac{\rho_c g_c'}{m} \right)^{-\frac{1}{3n+5}} t^{\frac{n+\alpha(n+2)}{3n+5}}. \quad (6.17)$$

These box model parameterizations [Eqs. (6.16) and (6.17)] provide current position and height predictions for the viscous propagation of non-Newtonian compositional gravity currents originating from a source with any α value. Note that for n = 1, Eq. (6.16) and (6.17) simplify to the box model solution of Ungarish (2009) for Newtonian viscous gravity currents.

6.1.2.3 Lubrication Theory Model

Here, the self-similarity solution of Di Federico et al. (2006b) for radial axisymmetric viscous non-Newtonian gravity currents is described. In this solution, the front position, r_N, of a cylindrical axisymmetric non-Newtonian gravity current is (Di Federico et al., 2006b):

$$r_N = \xi_N \left(\frac{n}{2n+1} \right)^{\frac{n}{3n+5}} \bar{h}^{\frac{(n+2)(3n+\alpha)}{n(3n+5)}} \left(\frac{\rho_c g_c'}{m} \right)^{\frac{\alpha(n+2)+n}{n(3n+5)}} t^{\frac{\alpha(n+2)+n}{3n+5}}. \quad (6.18)$$

Here, $\bar{h}$ is a typical length scale and ξ_N is the similarity variable at the nose of the current that needs to be determined by numerically integrating Eqs. (15) and (16) of Di Federico et al. (2006b) for $\alpha \neq 0$ (the interested reader is kindly referred to Di Federico et al., 2006b). Taking a length scale, $\bar{h} = Q^{\frac{1}{3}}$ and using Eq. (6.15), one can manipulate Di

Federico's front position expression (Eq. 6.18) into the same functional form of the force-balance expression in Eq. (6.20) as follows.

$$r_N = \xi_N \left(\frac{n}{2n+1} \right)^{\frac{n}{3n+5}} Q^{\frac{n+2}{3n+5}} \left[\frac{\rho_c g_c'}{m} \right]^{\frac{1}{3n+5}} t^{\frac{\alpha(n+2)+n}{3n+5}}. \tag{6.19}$$

6.1.3 Inter-Model Analysis

In the previous section, three different non-Newtonian viscous propagation models are described. The resulting expressions for these models have a similar form, as can be in Table 6.1.

Table 6.1. Front position parameterization for two-dimensional and radial axisymmetric gravity current.

Current		**Force-Balance**	**Lubrication Theory**	**Box Model**
2D	$x_N =$	$K_v q^{\frac{2+n}{2n+3}} \left[\frac{\rho_c g_c'}{m} \right]^{\frac{1}{2n+3}} t^{\frac{\alpha(n+2)+n}{2n+3}}$		
	$K_v =$	empirical K_v	$\eta_N \left(\frac{n}{2n+1} \right)^{\frac{n}{2n+3}}$	$\left(\frac{(2n+3)^n (n+1)}{2(\alpha+\alpha n+n)^n} \right)^{\frac{1}{2n+3}}$
Axisymmetric	$r_N =$	$K_v Q^{\frac{2+n}{3n+5}} \left[\frac{\rho_c g_c'}{m} \right]^{\frac{1}{3n+5}} t^{\frac{\alpha(n+2)+n}{3n+5}}$		
	$K_v =$	empirical K_v	$\xi_N \left(\frac{n}{2n+1} \right)^{\frac{n}{3n+5}}$	$\left(\frac{(3n+5)^n (n+2)}{2(n+\alpha n+2\alpha)^n} \right)^{\frac{1}{3n+5}}$

A comparison of the resulting expressions shows that the only differences among them are the pre-multiplicative proportionality constants, K_v which is a function of α and n. In this dissertation, the K_v of the force-balance model will be referred as empirical K_v,

the K_v of the lubrication theory model will be referred as self-similar K_v and the K_v of the box model solution will be referred as the box model K_v.

For two-dimensional gravity currents, the empirical K_v needs to be determined experimentally while the box model and the self-similar K_v are $\left(\frac{(2n+3)^n(n+1)}{2(\alpha+\alpha n+n)^n}\right)^{\frac{1}{2n+3}}$ and $\eta_n\left(\frac{n}{2n+1}\right)^{\frac{n}{2n+3}}$, respectively. In the self-similar K_v, η_n is obtained by numerically integrating an equation (Eq. 15 of Di Federico et al., 2006a) that represents the shape of the gravity current. Therefore, only the box model solution provides a closed form analytical solution for any value of α and n. However, the box model suffers from a number of simplifying assumptions and inconsistencies (see Section 6.1.1.2) which somewhat reduces the motivation of using the box model solution (Ungarish, 2009). However, for very quick prediction, the box model solution would be a good alternative. Fig. 6.2 presents a comparison of the box model and the self-similar K_v calculated for different values of α for n = *0.15*, *0.25*, *0.5* and *1.0*. For the self-similar K_v, η_n is determined by solving Eq. (15) of Di Federico et al. (2006) by the fourth-order Runge-Kutta method. As can be seen in Fig. 6.2, the proportionality constants for the box model solution are higher than that of the lubrication theory model solution when the fluid is Newtonian (n = 1) for different values of α, which is in line with the observation of Ungarish (2009). However, the difference of proportionality constant between the two models decreases as n decreases and when n = 0.25, they are almost equal. For n = 0.15, which is representative condition for the experiments conducted in this study, the

proportionality constants of the box model solution is less than that of lubrication theory model (see Fig. 6.2c).

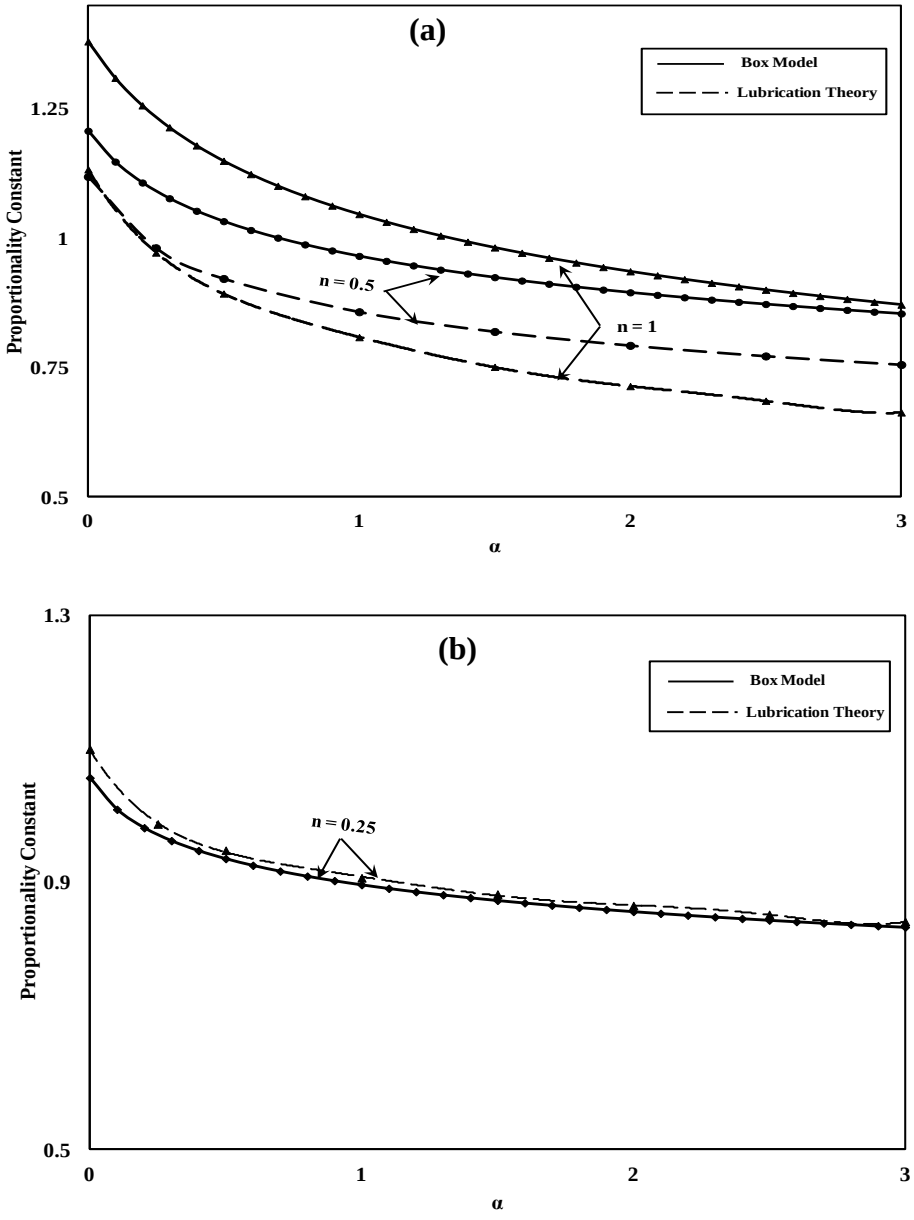

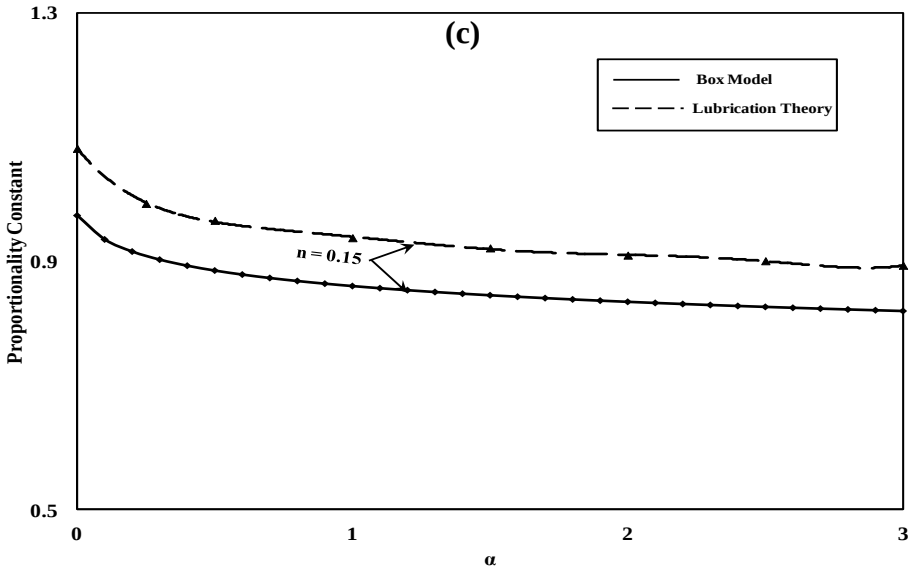

Figure 6.2. Variation of the viscous proportionality constants, K_v, for the box (solid line) and lubrication theory model (dashed line) models with α for n = 1.0, 0.5 in (a), n = 0.25 in (b), and n = 0.15 in (c).

6.2 Experimental Evaluation of the Models

This section presents the comparison of the predictions of the mathematical models discussed in Section 6.1 with the fluid mud gravity current propagation data from viscous propagation experiments. Only those experiments that fluid mud gravity currents propagated in the viscous-buoyancy phase for a significant time period are used. Please note that the evaluation of viscous models with experimental data is complicated. It is because even for the simple case of $\alpha = 0$, the transition process from inertial to viscous solution (i.e. the position to apply the viscous propagation model) is not clear and for $\alpha > 0$, the situation is more difficult (Ungarish, 2009). Since the above mentioned viscous models are valid for $t >> t^{**}$, it is very difficult to define a virtual origin for the

starting position for the viscous model predictions. Ungarish (2009) suggested to use a virtual origin corresponding to $(t^{**}+\gamma_v)$ with a proper choice of γ_v. However, it is not clear what would be the value of γ_v for a particular experiment. Hence, in evaluating the models, we assume that they are valid for $t = t^{**}$ and $x_N = x^{**}$, i.e. the virtual origin is at the transition point. Therefore, experimental data for $t \geq t^{**}$ (i.e., discarding the data corresponding to inertia-buoyancy phase) are used in our evaluation.

First, the models for two-dimensional non-Newtonian gravity current are evaluated using the date from viscous propagation experiments for two-dimensional fluid mud gravity currents and then the radially axisymmetric models are evaluated using the data from viscous propagation experiments for radial axisymmetric fluid mud gravity currents.

6.2.1 Two-Dimensional Fluid Mud Gravity Currents

First, the two-dimensional viscous propagation experiments for fluid mud gravity currents from constant volume release of fluid mud are used to evaluate the mathematical models described in Section 6.1 with $\alpha = 0$. Then, the constant flux release experiments are used to evaluate the mathematical models with $\alpha = 0$.

6.2.1.1 Constant Volume Release

In addition to determining the virtual origin in modeling the viscous propagation, calculating the model predictions for the viscous propagation characteristics of the gravity currents in lock-exchange experiments is cumbersome and requires a careful

consideration of the problem (see also the discussion in page 257 of Ungarish, 2009). The direct implementation of the respective expressions of the force-balance (Eq. 6.4), box (Eq. 6.13) and the lubrication theory models (Eq. 6.7) for $\alpha = 0$ is inadequate. Upon release of the fluid mud suspension, the initial propagation of the current in the inertia-buoyancy phase is considered to be inviscid. When the viscous transition occurs after a significant propagation distance, the current has already been well-established with a characteristic height and velocity. Though the viscous transition occurs over a finite propagation distance, for modeling simplicity it must be assumed that the transition occurs at a well-defined spatial position. When the current head passes the viscous transition position, most of its body is still in the inviscid region. For viscous propagation modeling purposes, the portion of the current in the inviscid region can be replaced with a source of fluid mud located at the viscous transition position (i.e., x_N at t**). A crude, but an essential assumption, in this analysis is that this source supplies a constant flux ($\dot{V} = U^{**}h^{**}$, U** and h** are the representative velocity and height of the laboratory gravity current at the transition position, respectively) fluid mud (i.e., $\alpha = 1$). Characteristics of this hypothetical viscous gravity current originating from the source is representative of the characteristics of the laboratory generated fluid mud gravity current in the viscous-buoyancy phase. Considering the transition position as the origin, the total released volume of fluid mud per unit width, *V*, at a particular time, *t*, from the source can be calculated as:

$$V = h^{**}U^{**}t. \tag{6.20}$$

Equating Eqs. (6.20) and (5.1) for α =1, one can show that $q = h^{**}U^{**}$. Once q is calculated, current front position with respect to the viscous transition position can be determined by using the selected viscous propagation model. Simplified representation of the inviscid portion of the current as a source at the transition position has limitations. The viscous transition position as the origin (i.e., location of the source) cannot be considered for the full duration of the viscous current propagation. When the entire current is in the viscous-buoyancy phase, the source location should be shifted. Hence, in mathematical modeling of the viscous propagation of the current, when the released fluid mud volume from the source, *V*, becomes equal to the initial lock volume, q_0, the source location should be shifted to the respective front position at that particular time.

A comparison of the force balance model predictions and the experimental observations corresponding to the viscous-buoyancy phase for current front positions in select experiments for clarity purposes are presented in Fig. 6.2. The estimated m and n values (see Table 3.1) are employed in these calculations. In Fig. 6.2a, the source is considered to be stationary at the viscous transition position throughout the experiment. As is evident in Fig. 6.2a, the predictions of the force-balance expression with the stationary source approach are in good agreement with the experimental data until $V=q_0$ and deviations of the predictions from the experimental observations increase as the current propagates. These deviations can be mitigated by shifting the source location as the entire current volume enters the viscous region. Figure 6.2b presents typical

comparison of model predictions by shifting the source location and the experimental data. The time at which the source location is shifted (i.e., when $V = q_0$) is indicated by an arrow in the graph. The velocity U^{**} at the shifted position can now be determined from the model prediction as the time required to travel the distance between the new and previous source locations are known. The best fit K_v values are calculated and tabulated in Table 6.1.

Based on the same mathematical modeling considerations described above, the self-similar solution expressed by Eq. (6.10) and box model solution by Eq. (6.7) are implemented to predict the viscous propagation of fluid mud gravity current. The self-similar and box model K_v values (tabulated in Table 6.1) are very close to the empirical K_v values in the force-balance expression and expectedly, the box model K_v values for a particular experiment is higher than that of self-similar K_v. Lubrication theory and box model predictions, which are in good agreement with the experimental data, are presented in Fig. 6.4 and Fig. 6.5, respectively. Comparing the force-balance, box model and lubrication theory model predictions with the experimental data, it is found that the R^2 values are very similar, with slightly better values for the force-balance model predictions. This is simply due to the fact that the force-balance expression has a free parameter which is fitted using the experimental data (i.e., empirical K_v) while the other two model lack this free parameter. It is important to note that although the three models are intended for compositional gravity currents, their predictions are in good agreement with the experimental data for the fluid mud gravity currents.

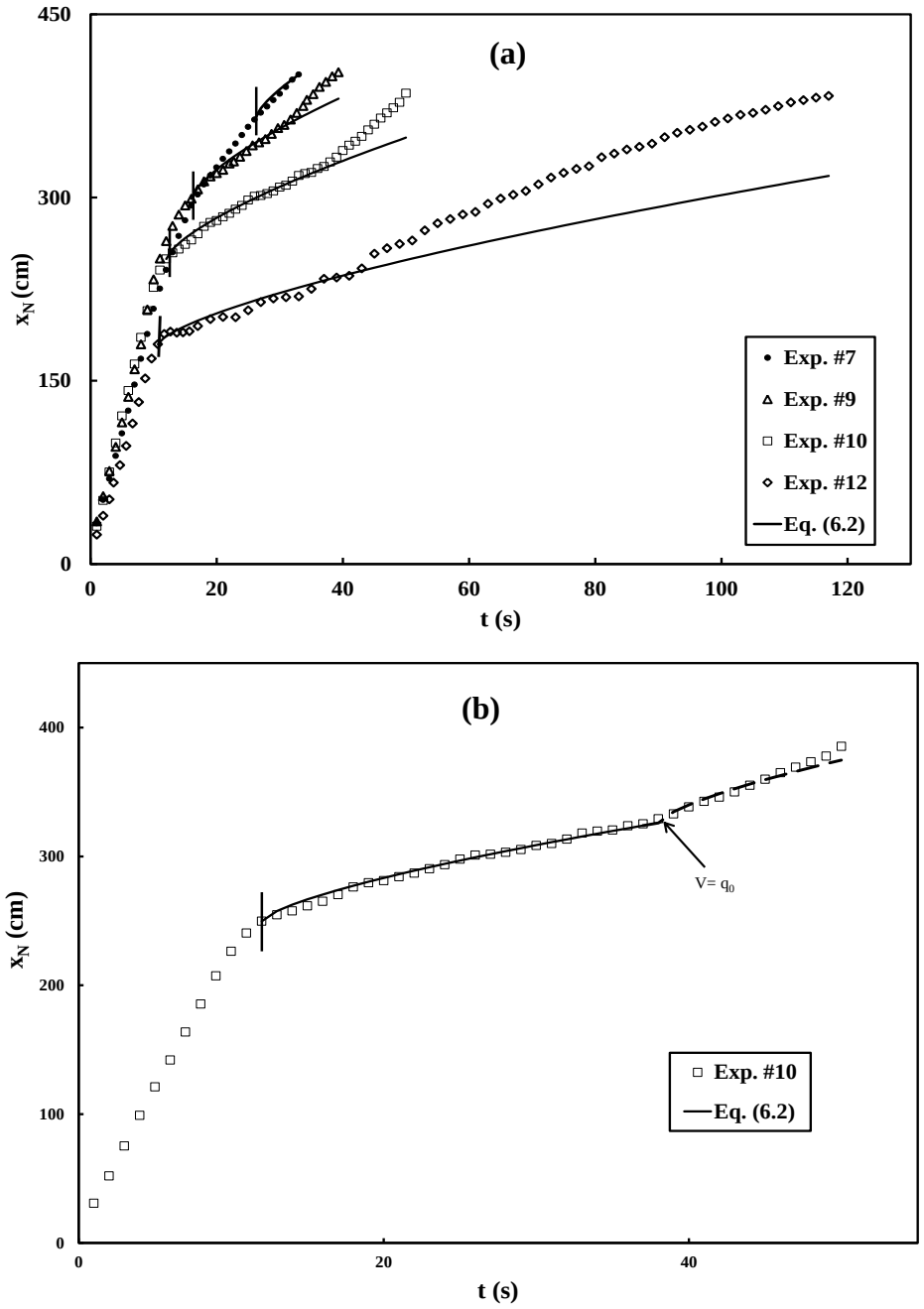

Figure 6.3. Comparison of the predictions by the viscous force-balance model (solid lines) with the 2-D constant volume release experimental data (symbols, see the legend) for the front position of the fluid mud gravity currents in the viscous-buoyancy propagation phase. (a) Predictions using a fixed source location (x_N at t**, shown with thick vertical solid lines) for the entire experimental viscous propagation, (b) predictions for Exp. # 10 using a shifting source location (shown in the graph) as *V* becomes equal to $q_{0.}$

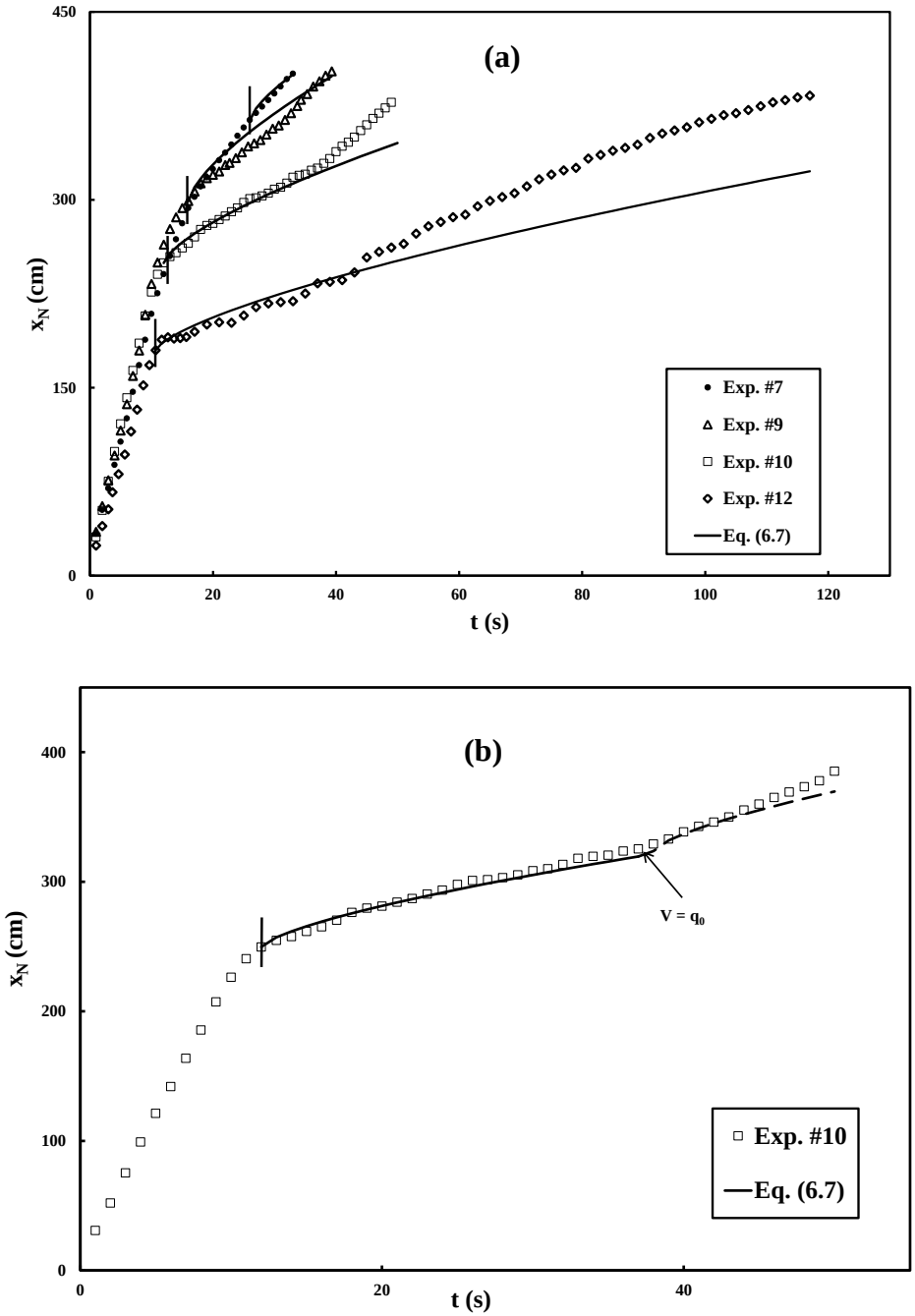

Figure 6.4. Comparison of the predictions by the viscous box model (solid lines) with the 2-D constant volume release experimental data (symbols, see the legend) for the front position of the fluid mud gravity currents in the viscous-buoyancy propagation phase. (a) Predictions using a fixed source location (x_N at t^{**}, shown with thick vertical solid lines) for the entire experimental viscous propagation, (b) predictions for Exp. # 10 using a shifting source location (shown in the graph) as V becomes equal to q_0.

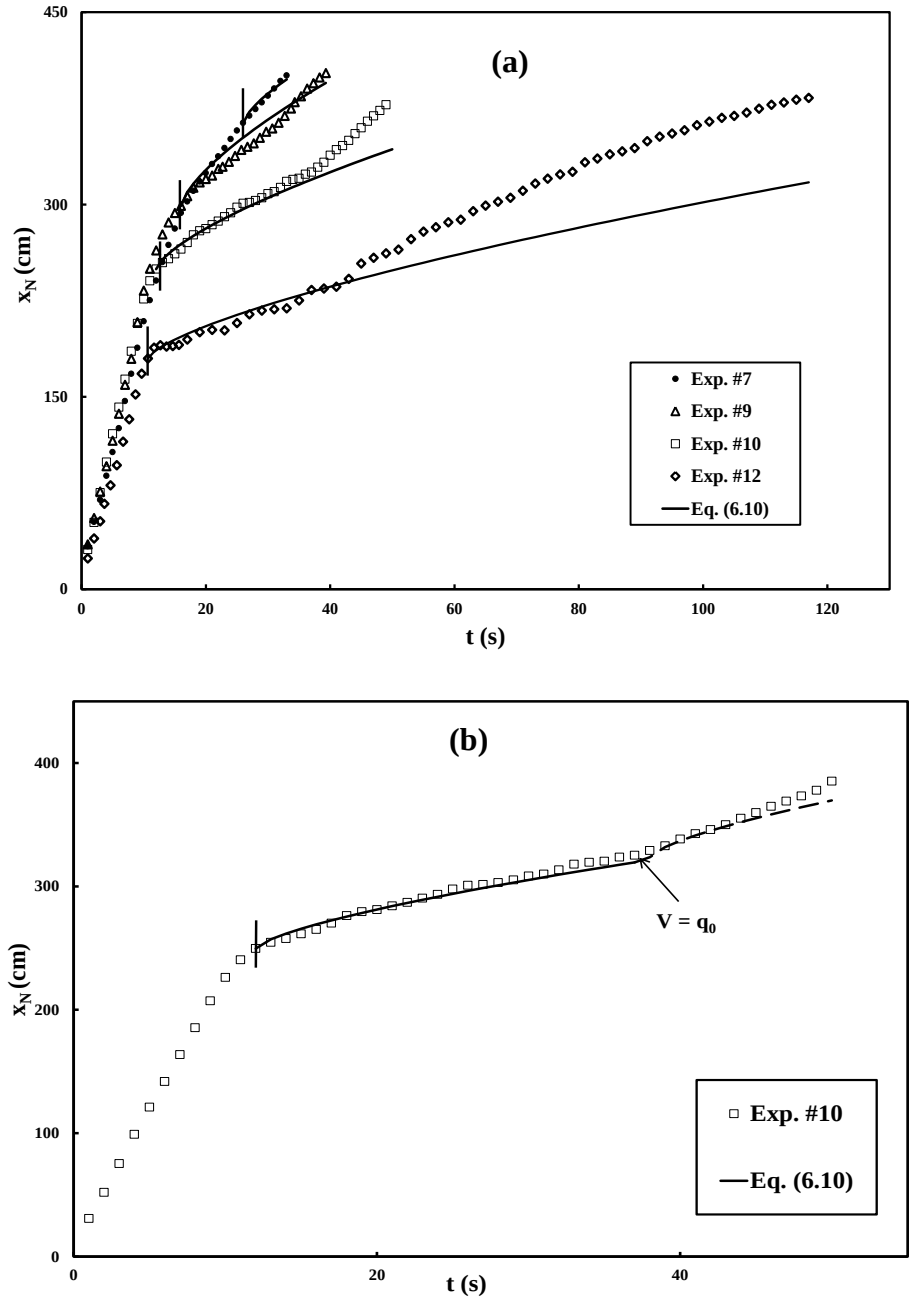

Figure 6.5. Comparison of the predictions by the lubrication theory (solid lines) with the 2-D constant volume release experimental data (symbols, see the legend) for the front position of the fluid mud gravity currents in the viscous-buoyancy propagation phase. (a) Predictions using a fixed source location (x_N at t^{**}, shown with thick vertical solid lines) for the entire experimental viscous propagation, (b) predictions for Exp. # 10 using a shifting source location (shown in the graph) as V becomes equal to q_0.

Table 6.1. Proportionality constant, K_v, and coefficient of correlation, R^2, values for viscous non-Newtonian force-balance, box and lubrication theory models for the viscous phase of the 2-D constant-volume release experiments in Table 3.1.

Exp. #	Force-balance		Lubrication Theory		Box Model	
	K_v	R^2	K_v	R^2	K_v	R^2
7	0.93	0.965	0.9287	0.962	0.994	0.945
8	0.96	0.9	0.933	0.896	0.982	0.856
9	0.8	0.98	0.936	0.86	0.973	0.8
10	1	0.987	0.941	0.975	0.963	0.96
11	0.98	0.966	0.9433	0.952	0.959	0.934
12	0.8	0.98	0.936	0.944	0.973	0.93

6.2.1.2 Constant Flux Release

In modeling calculations for constant flux release experiments, a discrete transition at the viscous transition position was assumed although viscous transition occurs over a finite propagation distance. Moreover, in viscous propagation calculations the portion of the current in the inviscid region was replaced with a two-dimensional source of constant fluid mud flux located at the viscous transition position. Therefore, the experimentally determined transition position is considered as the virtual origin for the viscous propagation phase. In our calculations, the associated transition lengths are added to the model front position predictions. In this section, only the predictive capabilities of the box model and lubrication theory models are provided, primarily to see how the closed form analytical solution of the box model performs in comparison to the lubrication theory, which needs numerical solution for constant flux release experiments.

In Fig. 6.6, comparisons of the current front position observations and the corresponding box model and lubrication theory model predictions are presented. Comparisons of only select experiments are shown for the clarity of the figure. In this figure, data from the inertia-buoyancy propagation phase is omitted and only the front position data for the viscous-buoyancy propagation phase is plotted. Model predictions are calculated beginning from viscous transition points. As can be seen from this figure, although predictions by both of the models agree well with the experimental data, the box model solution usually provides lower values of front position, x_N, the lubrication theory model solution for a given time, t. The underestimation of the box model solution is due to the differences in the proportionality constants, K_v for our experimental conditions (see Fig. 6.2).

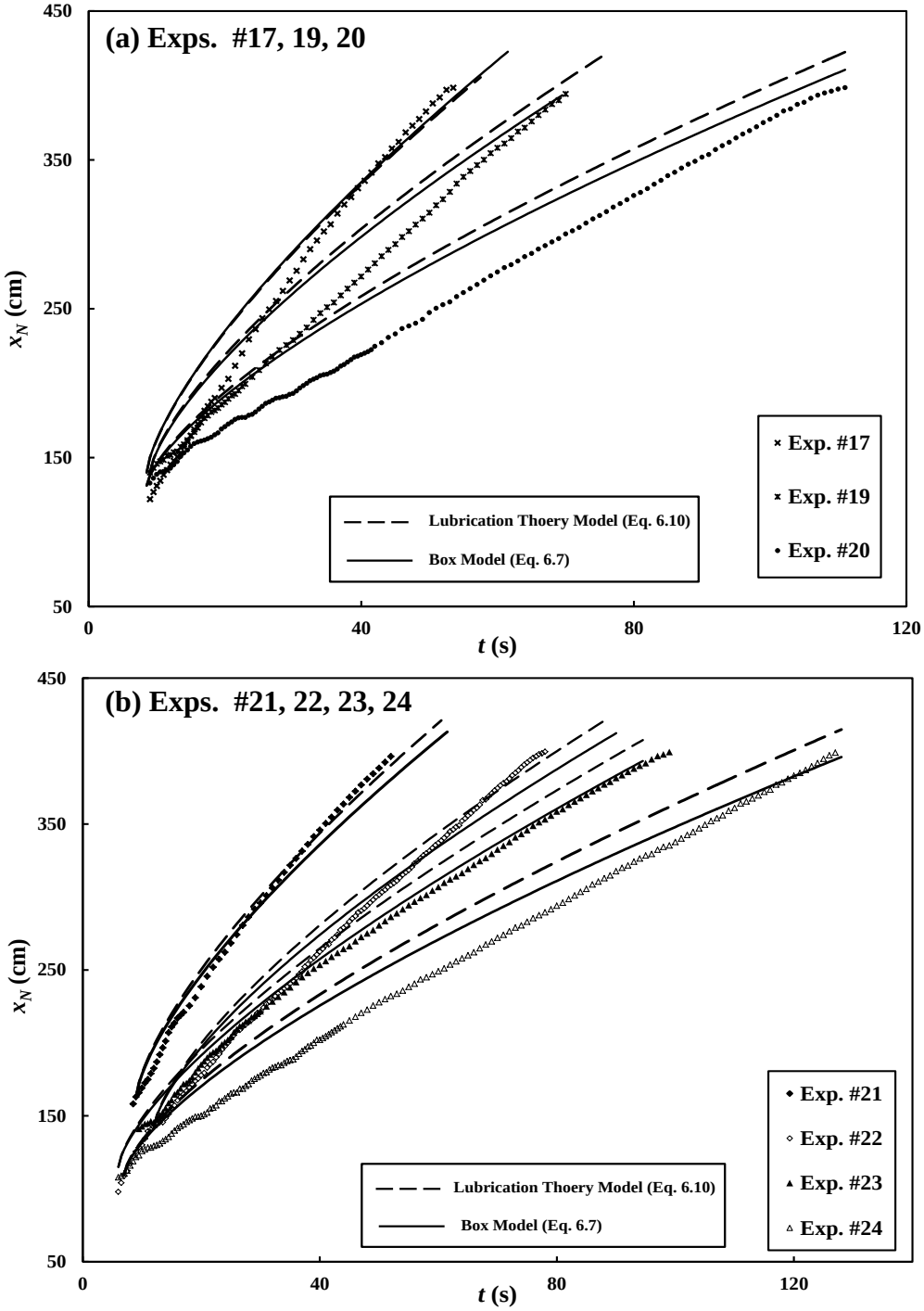

Figure 6.6. Comparison of the current front position, x_N, predictions by the box model solution (solid lines, Eq. 6.7) and lubrication theory model (dash lines, Eq. 6.10) with the 2-D constant flux release experimental data. Exp. #18 is not shown in the figure for clarity purposes. Symbols represent the data from the experiments tabulated in Table 3.2 and the corresponding experiment identifiers are defined in the legend.

6.2.2 Radial Axisymmetric Fluid Mud Gravity Current

Following the same procedure of two-dimensional constant flux release experiments (Section 6.2.1.2), the viscous propagations of radially axisymmetric experiments (Expt. #32, 34 and 35) are compared with the predictions of radial viscous box model solution in Eq. (6.16) which is shown in Fig. 6.7. As it was the case for two-dimensional gravity current, the trend of the prediction of box model solution is in good agreement with the experimental data, however the box model overestimate the experimental observation.

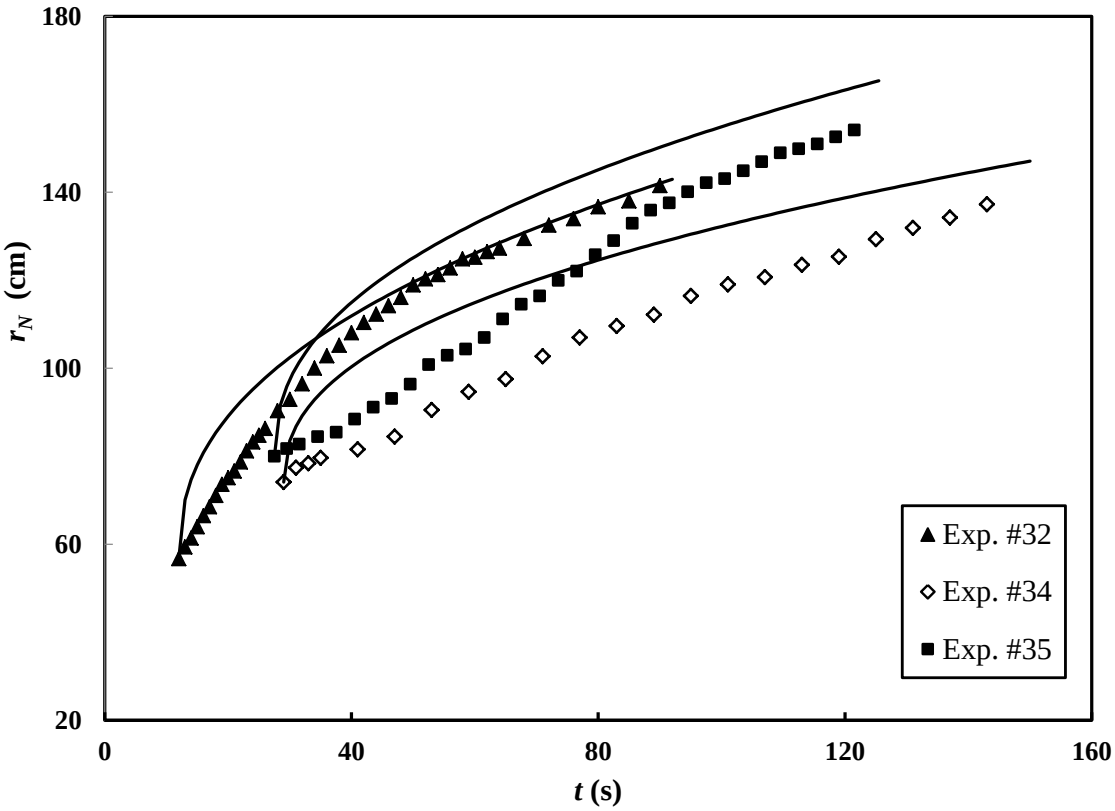

Figure 6.7. Comparison of the current radial front position, r_N, predictions by the viscous box model solution (solid lines, Eq. 6.16) with the experimental data. Symbols represent the data from the experiments tabulated in Table 3.3 and the corresponding experiment identifier is defined in the legend.

CHAPTER SEVEN

CONCLUSIONS AND FUTURE WORK

Conclusions of this investigation are summarized in Section 7.1. Noteworthy scientific contributions of this investigation are listed briefly in Section 7.2. Recommendations for the future work are also provided in Section 7.3.

7.1 Conclusions

In this dissertation, the results of a thorough theoretical and experimental investigation on fluid mud underflows generated in a typical coastal dredge disposal operation have been presented. The investigation was performed to determine the influence of the disposal characteristics (e.g. discharge configuration, initial concentrations and rheological properties of discharged fluid mud) on the propagation dynamics of the fluid mud underflows.

Laboratory experiments were conducted with different initial fluid mud concentrations in three different experimental set-ups: rectangular flume for constant volume release, rectangular flume for constant flux release, and a square pool for radial constant flux release of fluid mud. The experiments in the rectangular flume generated two-dimensional underflows. The experiments in the pool simulated typical open water pipeline disposal operations with submerged vertical discharge configuration in the field and radially axisymmetric three-dimensional fluid mud underflows were generated in these experiments. To determine the propagation phases for each experiment, the

propagation curves (front positions vs. time) were scaled using appropriate length and time scales for each release configuration and the scaled propagation curves were plotted in log-log plots to distinguish the propagation phase for each experiments. The log-log plots of the scaled propagation curves revealed that constant volume release experiments generated gravity currents of fluid mud that exhibit slumping, inertial and viscous propagation phases while constant flux release experiments generated initial horizontal buoyant wall jets which then transform into gravity currents that exhibit inertial and viscous propagation phases. These plots also showed that the propagations of underflows were significantly influenced by the non-Newtonian rheology of the released fluid mud. Underflows formed by low concentration fluid mud releases did not experience the viscous propagation phase in the limited experimental set-ups that were used in the investigation. However, high concentration fluid mud releases rapidly transitioned into viscous propagation phase, sometimes even bypassing the expected inviscid phase. The transition times and positions/lengths for propagation phase transitions were also determined from the experimental data. For the constant volume release experiments, the transition length, x^*, from slumping to inertial phase was found to be constant and was approximately 9-10 lock-lengths which conforms to the observations reported by previous studies for compositional Newtonian gravity currents. However, the transition time, t^*, from slumping to the inertial phase decreases as the concentration of fluid mud increases, for release of the same fluid mud volume. For constant flux release experiments, the transition length from the initial jet to the gravity current, x_j , was found to be related with the inlet height for the two-dimensional and the discharge height

(height from the discharge port to the bottom) for the radially axisymmetric gravity currents. On the other hand, the transition time from the initial jet to the gravity current, t_j , was found to depend on the buoyancy flux, B_0, and the inlet height (for two-dimensional) or the discharge height (for radially axisymmetric). The viscous transition time, t^{**} was found to depend on the released volume or volume flux of the fluid mud and the rheological properties. If the same volume or flux is released in two separate experiments with different concentrations, having the higher viscosity, the fluid mud current with the higher initial concentration would make faster transition to the viscous phase. For some of the experiments, currents made transitions to the viscous phase directly from the slumping phase or the jet phase bypassing the expected inertial phase. Sometimes, the viscous transition occurred even before the underflow propagated the expected jet or slumping length mentioned above.

The theoretical part of this investigation included experimental evaluation of three mathematical modeling approaches to model the inertial and viscous propagation of fluid mud gravity currents. These three mathematical modeling approaches are, from simplest to the most complex: force-balance, box and shallow water/lubrication theory approximation models. For constant volume release experiments, the predictions of force-balance, box and shallow water model with a representative Froude number condition were in good agreement with the inertial propagation of experimental fluid mud gravity currents. The predictive capabilities of the compositional box and the shallow water models were also compared with the predictions of their suspension counterparts in which settling of the particles are incorporated. These comparisons revealed that the

inertial propagation of fluid mud can be modeled by the mathematical models for the compositional gravity current without compromising much accuracy. However, note that for longer propagation distances/times that the ones in our experiments, the settling effects may be significant, and accuracy of the compositional models may be compromised. The predictions of the box model solution were also compared with the inertial propagations of two-dimensional and radial axisymmetric constant flux released experiments. Best-fit Froude number conditions for each constant flux release experiment were obtained since there is no widely accepted Froude number condition for the constant flux release experiments. It was found that the best-fit Froude number values are much higher than the suggested value in the literature. For the inertial propagation of fluid mud gravity currents, it was concluded that the box model would be the most efficient analytical model due to its closed-form solution for all of the release configurations and its predictive accuracy (based upon its experimental evaluation and inter-comparisons of the models).

Unlike the inertial gravity currents, the mathematical modeling attempts for the non-Newtonian viscous gravity currents are limited in the literature. For example, there were no force-balance and box model solutions for viscous propagation of non-Newtonian gravity currents. These two models were derived for both two-dimensional and radially axisymmetric gravity currents in this investigation. The prediction capabilities of these two proposed models, force-balance and box models, along with the available self-similarity solution based upon the lubrication theory were using the viscous propagation experiments of fluid mud gravity currents. However, the implementations of

viscous models are complicated and need careful consideration of the problem. It is because the viscous models are valid when $t>>t^{**}$. Hence, a virtual origin needs to be set from which the predictions of the viscous models starts. It is suggested in the literature to use a virtual origin corresponding to $\left(t^{**}+\gamma_v\right)$ with a proper choice of γ_v. However, it was not clear what would be the proper value of γ_v for a particular flow condition. In our evaluation of the viscous models, the virtual origin was placed at t^{**} considering $\gamma_v = 0$. In addition, it is shown that the fixed volume release experiments need to be considered as a constant flux release case viscous modeling calculations. Experimental evaluation of the box and lubrication theory models indicated that the lubrication theory model has better predictive capabilities. However, there is a pre-multiplicative constant in the lubrication theory model that needs to be determined numerically for constant flux release experiments whereas box model solution is a closed form analytical solution for all possible release configurations making it a good alternative, especially for quick predictions. A parameterization for t^{**} that includes an empirical coefficient was derived from the order-of-magnitude relationships and the predictions of this parameterization were compared with the experimental data for constant volume release experiments the value of the empirical coefficient was determined.

7.2 Major Research Contributions

This section lists the major research contributions (experimental contributions in Section 7.2.1 and theoretical contributions in Section 7.2.2) of this doctoral research.

7.2.1 Experimental Contributions

There are very few experimental investigations on fluid mud underflows and the experimental component of this doctoral research contributed the literature as follows:

- Large data sets of the propagation of two-dimensional fluid mud underflows from both constant volume and constant flux release of fluid mud are provided. Though Van Kessel and Kranenburg (1996) conducted two-dimensional constant flux release fluid mud experiments, the current propagation data was not provided.

- An experimental data set of the propagation of radially axisymmetric fluid mud underflows from laboratory experiments that simulated typical coastal dredge disposal operations is provided. To the best the author's knowledge, this is the first thorough attempt to obtain experimental data on the radial advance of fluid mud underflows over time.

- Based on the analysis of the experimental data, this investigation provided much insight on how fluid mud underflows experience different propagation phases and how they transition from one phase to another. It also experimentally determined the transition positions and times.

- Non-Newtonian rheology effects on the propagation dynamics of the underflows are elucidated thoroughly.

7.2.2 Theoretical Contributions

In evaluating the mathematical models, the inertial propagation of fluid mud gravity currents were modeled using the available inertial models. However, since models for all the mathematical modeling approaches were not available for viscous propagation of non-Newtonian gravity currents, the following theoretical contributions have been made:

Contributions	Equation number
Derivation and evaluation of Force-balance expressions for two-dimensional and radially axisymmetric viscous non-Newtonian (power-law) gravity currents.	(6.2), (6.12)
Derivation and evaluation of box model expression for two-dimensional propagation of a viscous non-Newtonian (power-law) gravity current	(6.7), (6.8)
Derivation and evaluation of box model solution for radially axisymmetric viscous non-Newtonian (power-law) gravity current	(6.16), (6.17)

7.3 Future Work

It is expected that the work presented in this dissertation will stimulate more research on the fluid mud underflows generated in coastal dredge disposal operations or in other applications, particularly on the following areas:

1. The most obvious extension of the experimental investigation part of this work is to conduct a thorough laboratory study on the fluid mud underflows

generated from horizontal (see Fig. 2.2b and 2.2c for example) or other discharge configurations. It is expected that the underflows will not be asymmetric and the downstream portion will be more pronounced than the upstream portion for horizontal discharge configuration. The first step of the investigation would be to find the impingement angle in relation to the discharge angle. Then, the propagation for both upstream and downstream propagation can be studied to determine the propagation dynamics and inter-transition of propagation phases.

2. In this investigation, fluid mud underflows were investigated with horizontal bottom and the slope of the bottom was not considered. However, slope of the bottom is expected to influence the propagation dynamics significantly. It will be interesting to see how the propagation transition position and time varies in relation to the slope angle.

3. In addition to the slope of the bottom, the ambient water conditions will also affect the propagation of underflows generated in a typical dredge disposal operation. It is highly likely that either current or waves or both may be present in most disposal locations. Experimental investigations are necessary to see the effects of these ambient conditions on the propagation dynamics of underflows. Several such studies on the propagation of saline gravity currents are available in the literature which can be the basis of such complex fluid mud studies.

4. Though this investigation provided insights on the influence of the rheological properties on the transition from inertial to viscous phase, there is a need for further studies. A Reynolds number criterion for the transition of laminar to turbulent gravity current is of importance among others.

5. Developing mathematical models for the propagation of asymmetric fluid mud underflows is of importance. A box model solution which will incorporate the impingement angle in the derivation for quick prediction of such currents may be possible. As discussed in Chapter 5, the inertial box model solution can be easily modified for the experiments conducted in a sector tank which can be the basis for developing such a model. If the impingement angle can be related to the discharge angle from the experimental investigation mentioned above (see 1), such a model would give the complete information for the propagation fluid mud underflows generated from different discharge configurations

6. Finally, experimental investigations are necessary to determine the run-out length of fluid mud underflows. Such experiments may need a large experimental facility.

APPENDICES

Appendix A

Parameterization of Viscous Transition Time

As noted earlier, the mathematical models described in Section 6.1 are valid when $t>>t^{**}$. Therefore, it is of importance to provide a mathematical expression for t^{**}, propagation time that corresponds to transition between inertia-buoyancy and viscous-buoyancy phases. Huppert (1982) proposed a parameterization for t^{**}, for two-dimensional and radial propagation of Newtonian compositional gravity currents. Following Huppert's procedure, in this section, parameterizations for t^{**} for two-dimensional and radial propagation of a non-Newtonian compositional gravity current are derived.

A.1 Two-dimensional Gravity Current

Considering a two-dimensional power-law viscous gravity current of an incompressible non-Newtonian fluid of density ρ_c propagating under a Newtonian ambient fluid of lesser density ρ_a along a horizontal bottom, the order of magnitude expressions for the buoyancy force F_g, inertia force F_i, and viscous force F_v can be obtained as follows:

$$F_g \sim \rho_c g_c' h_N^2 w = \rho_c g_c' q^2 x_N^{-2} w t^{2\alpha}. \tag{A.1}$$

$$F_i \sim \rho_c U_N^2 h_N w = \rho_c q x_N w t^{\alpha-2} \tag{A.2}$$

$$F_v \sim m\left(\frac{U_N}{h_N}\right)^n x_N w = m x_N{}^{2n+1} q^{-n} t^{-n(\alpha+1)} w \tag{A.3}$$

Equating Eqs. (A.1) and (A.2) [i.e. the current propagates under inertia-buoyancy balance], one can show that:

$$x_n \sim \left(g_c' q\right)^{\frac{1}{3}} t^{\frac{\alpha+2}{3}}. \tag{A.4}$$

Equating (A.2) and (A.3) [i.e. inertia and viscous forces become comparable], and using (A.4), the transition time t^{**} can be obtained as:

$$t^{**} \sim \left(\frac{\rho_c^3 q^{n+3}}{m^3 g_c'^{2n}}\right)^{\frac{1}{3(2-\alpha)+n(1-\alpha)}}. \tag{A.5}$$

A.2 Radial Axisymmetric Gravity Current

Following the same procedure of section A.1 and considering a radially axisymmetric power-law viscous gravity current of an incompressible non-Newtonian fluid propagating under a Newtonian ambient fluid along a horizontal bottom, the order of magnitude expressions for the buoyancy force F_g, the inertia force F_i, and the viscous force F_v can be obtained as follows:

$$F_g \sim \rho_c g_c' h_N^2 r_N = \rho_c g_c' Q^2 r_N^{-3} t^{2\alpha}. \tag{A.6}$$

$$F_i \sim \rho_c U_N^2 h_N r_N = \rho_c Q r_N t^{\alpha-2} \tag{A.7}$$

$$F_v \sim m\left(\frac{U_N}{h_N}\right)^n r_N{}^2 = m r_N{}^{3n+2} Q^{-n} t^{-n(\alpha+1)} \tag{A.8}$$

Equating Eqns. (A.6) and (A.7) [i.e. the current propagates under inertia-buoyancy balance], one can show that:

$$r_n \sim \left(g_c^{'} Q\right)^{\frac{1}{3}} t^{\frac{\alpha+2}{4}}. \tag{A.9}$$

Equating Eqns. (A.7) and (A.8) [i.e. inertia and viscous forces become comparable], and using (A.9), the transition time t^{**} can be obtained as:

$$t^{**} \sim \left(\frac{\rho_c^4 Q^{n+3}}{m^4 g_c^{'1+3n}}\right)^{\frac{1}{(10-3\alpha)+n(2-\alpha)}}. \tag{A.10}$$

BIBLIOGRAPHY

Acton, J., Huppert, H., and Worster, M., (2000). Two-dimensional viscous gravity currents flowing over a deep porous medium. *Journal of Fluid Mechanics, 440*, 359-380.

Altinakar, M., Graf, W., and Hopfinger, E., (1996). Flow structure in turbidity currents. *Journal of Hydraulic Research, 34*, 713 – 718.

Barnard, W., (1978). Prediction and control of dredged material dispersion around dredging and open water pipeline disposal operations: *Technical Report DS-78-13, US Army Engineer Waterways Experiment Station, Vicksburg,* MS.

Benjamin, T., (1968). Gravity currents and related phenomena. *Journal of Fluid Mechanics, 31*, 209-248

Blanchette, F., Piche, V., Meiburg, E., and Strauss M., (2006). Evaluation of a simplified approach for simulating gravity currents over slopes of varying angles. *Computers and Fluids , 35*, 492-500.

Bonnecaze, R., Hallworth, M., Huppert, H., and Lister, J., (1995). Axisymmetric particle-driven gravity currents. *Journal of Fluid Mechanics, 294*, 93-121.

Bonnecaze, R., Huppert, H., and Lister, J., (1993). Particle-driven gravity currents. *Journal of Fluid Mechanics, 250*, 339-339.

Bonnecaze, R., and Lister, J., (1999). Particle-driven gravity currents down planar slopes. *Journal of Fluid Mechanics, 390*, 75-91.

Bowen, A., Normark, W., and Piper, D., (1984). Modelling of turbidity currents on Navy submarine fan, California continental borderland. *Sedimentology , 31*, 169-185.

Brandsma, M., and Divoky, D., (1976). Development of models for prediction of short-term fate of dredged material discharged in the estuarine environment. *Contract Report D-76-5, US Army Engineer Waterways Experiment Station, Vicksburg,* MS.

Bremer, T., and Hunt, G., (2010). Universtal solution for boussinesq and non-boussinesq plumes. *Journal of Fluid Mechanics, 644*, 165-192.

Britter, R., (1979). The spread of a negatively buoyant plume in a calm environment. *Atmoshpheric Environment, 13*, 1241-1247.

Britter, R., and Simpson, J., (1978). Experiments on the dynamics of a gravity current head. *Journal of Fluid Mechanics, 88*, 223-240.

Burt, T., and Fletcher, C., (1997). Disposal in the sea. *Terra et Aqua, 66*, 3-13.

Cantero, M., Balachandar, S., and Garcia, M., (2007). High-resolution simulations of cylindrical density currents. *Journal of Fluid Mechanics, 590*, 437-469.

Cavalletti, A., and Davies, P., (2003). Impact of vertical, turbulent, planar, negatively buoyant jet with rigid horizontal bottom boundary. *Journal of Hydraulic Engineering*, *129*(1), 54-62. doi: 10.1061/(ASCE)0733-9429(2003)129:1(54).

Chen, J., (1980). *Studies on gravitational propagation currents*. PhD thesis, California Institute of Technology.

Chen, J., and Rodi, W., (1980). Turbulent buoyant jets – a review of experimental data. *Pergamon*.

Chowdhury, M., and Testik, F., (2011a). Laboratory testing of mathematical models for high-concentration fluid mud turbidity currents. *Ocean Engineering, 38*(1), 256-270. Elsevier. doi: 10.1016/j.oceaneng.2010.10.020.

Chowdhury, M., and Testik, F., (2011b). Subaqueous sediment gravity flows from open water pipeline dredge disposal: experiment and modeling. *In Proceeding of 2011 Conference on Coastal Engineering Practice: Engineering Sustainable Coastal Development*. August 21-24, California.

Chowdhury, M., and Testik, F., (2011c). Viscous propagation of two-dimensional non-Newtonian gravity currents. *Submitted to Fluid Dynamics Research (under revision).*

Chowdhury, M. R., Testik, F. Y., and Khan, A. A., (2009). Three-dimensional flow structure at the frontal zone of a gravity-driven fluid mud flow. *Journal of the Visualization, 12* (4).

Coussot, P., (1997). *Mudflow Rheology and Dynamics*. International Association for Hydraulic Research monograph series, Balkema, Rotterdam, p. 255. .

Dade, W., and Huppert, H., (1995a). A box model for non-entraining, suspension-driven gravity surges on horizontal surfaces. *Sedimentology, 42*, 453-472.

Dade, W., and Huppert, H., (1995b). Runout and fine-sediment deposit of axisymmetric turbidity currents. *Journal of Geophysical Research, 100*, 18597-18609.

Dankers, P., (2002). The behaviour of fines released due to dredging: a literature review. *Delft University of Technology, the Netherlands*, p59.

De Silva, I., Fernando, H., Eaton, F. and Hebert, D., (1996). Evolution of Kelvin-Helmholtz billows in nature and laboratory. *Earth and Planetary Science Letters, 143*, 217-231.

Didden, N. and Maxworthy, T., (1982). The viscous propagation of plane and axisymmetric gravity currents. *Journal of Fluid Mechanics, 121*, 27-42.

Di Federico, V., Malavasi, S., and Cintoli, S., (2006a). Viscous Propagation of Non-Newtonian Gravity Currents on a Plane. *Meccanica, 41*, 207-217.

Di Federico, V., Malavasi, S., and Bizzarri, G., (2006b). Viscous Spreading of Non-Newtonian Gravity Currents in radial geometry. *WIT Transactions on Engineering Sciences, 52*, 399-408.

Drago, M., (2002). A coupled debris flow-turbidity current model. *Ocean Engineering*, 29, 1769-1780.

Fan, L., (1967). Turbulent buoyant jets into stratified or flowing ambient fluids. *Technical Report KHR-15, W.M. Keck Laboratory of Hydraulics and Water Resources, California Institure of Technology, Passdena, CA, USA*.

Fischer, H., List, E., Koh, R., Imgerger, J., and Brooks, N., (1981). *Mixing in inland and coastal waters.* p 478. Academic Press.

Fleischmann, C. M., Pagni, P. J., and Williamson, R. B., (1994). Salt water modeling of fire compartment gravity currents. *Fire Safety Science – Proceedings of the Fourth International Symposium*, Ottawa, June 13-17, Internation Association for Fire Safety Science, Gaithersburg 253-264.

George, R. (1980). Impinging jets. *Engineering research Centre Technical Report REC-ERC-80-8, Water and Power Research Service, Denver, Colorado*.

Gladstone, C., Phillips, J. and Sparks, R., (1998). Experiments on bidisperse, constant-volume gravity currents: propagation and sediment deposition. *Sedimentology, 45*, 833-844.

Gladstone, C. and Woods, A., (2000). On the application of box models to particle-driven gravity currents. *Journal of Fluid Mechanics, 416*, 187-195.

Gratton, J., and Minotti, F., (1999). Thoery of creeping gravity currents of a non-Newtonian liquid. *Physical Review E, 60*, 6960-6967.

Grundy, R. and Rottman, J., (1985). The approach to self-similarity of the shallow-water equations representing gravity-current releases. *Journal of Fluid Mechanics, 156*, 39-53.

Haertel, C., Meiburg, E. and Necker, F., (2000). Analysis and direct numerical simulation of the flow at a gravity-current head. Part 1. Flow topology and front speed for slip and no-slip boundaries. *Journal of Fluid Mechanics, 418*, 189-212.

Hales, L., (1996). Analysis of dredged material disposed in open water: summary report for technical area 1. *Technical Report DRP-96-4, US Army Engineer Waterways Experiment Station, Vicksburg*, MS.

Hall, N., Elenany, M., Zhu, D., and Rajaratnam, N., (2010). Experimental Study of Sand and Slurry Jets in Water. *Journal of Hydraulic Engineering*, *136*(10), 727-738. doi: 10.1061/(ASCE)HY.1943-7900.0000235.

Hallez, Y., and Magnaudet, J., (2009). A numerical investigation of horizontal viscous gravity currents. *Journal of Fluid Mechanics, 630*, 71-91.

Hallworth, M., Hogg, A., and Huppert, H., (1998). Effects of external flow on compositional and particle gravity currents. *Journal of Fluid Mechanics , 359*, 109-142.

Harris, T., Hogg, A. and Huppert, H., (2001). A mathematical framework for the analysis of particle-driven gravity currents. *Proceedings of the Royal Society of London-A-Mathem and Physical and Engin Sciences, 457*, 1241-1272.

Henry, G., Neal, R., and Greene, S., (1978). Laboratory investigation of the dynamics of mud flows generated by open-water pipeline disposal operations. *Technical Report D-78-46, US Army Engineer Waterways Experiment Station, Vicksburg*, MS.

Hogg, A., Huppert, H., and Hallworth, M. (1999). Reversing buoyancy of particle-driven gravity currents. *Physics of Fluids , 11*, 2891-2900.

Hogg, A., Ungarish, M. and Huppert, H., (2000). Particle-driven gravity currents: asymptotic and box model solutions. *European Journal of Mechanics B- Fluids , 19*, 139-165.

Holliday, B., Johnson, B., and Thomas, W., (1978). Predicting and monitoring dredged material movement. *Technical Report D-78-3, US Army Engineer Waterways Experiment Station, Vicksburg*, MS.

Hoult, D., (1972). Oil propagation on the sea. *Anuual Review of Fluid Mechanics, 4*, 341-368.

Huang, X. and Garcia, M., (1998). A Herschel--Bulkley model for mud flow down a slope. *Journal of Fluid Mechanics, 374*, 305-333.

Huppert, H. E. and Simpson, J. E., (1980). The slumping of gravity currents. *Journal of Fluid Mechanics, 99*, 785-799.

Huppert, H. E., (1982a). The propagation of two-dimensional and axisymmetric viscous gravity currents over a rigid horizontal surface. *Journal of Fluid Mechanics, 121*, 43-58.

Huppert, H., (1982b). Flow and instability of a viscous current down a slope. *Letters to Nature, 300*, 427-429.

Huppert, H., (1998). Quantitative modelling of granular suspension flows. *Philosophical Transactions: Mathematical, Physical and Engineering Sciences, 356*, 2471-2496.

Huppert, H., (2004). Gravity currents in nature and industry. *15thAustralasian Fluid Mechanics Conference, The university of Sydney, Australia.*

Huppert, H., (2006). Gravity currents: a personal perspective. *Journal of Fluid Mechanics, 554*, 299-322.

Hurzeler, B., Imberger, J. and Ivey, G., (1996). Dynamics of turbidity current with reversing buoyancy. *ASCE Journal of Hydraulic Engineering, 122*, 230-236.

Jiang, J., Law, A., and Cheng, N., (2005). Two-phase analysis of vertical sediment-laden jets. *Journal of Engineering Mechanics, 131*(3), 308. doi: 10.1061/(ASCE)0733-9399(2005)131:3(308).

Jiang, L., and Leblond, P., (1993a). Numerical modelling of an underwater Bingham plastic mudslide and the waves which it generates. *Journal of Geophysical Research, 98*, 10303-10317.

Jiang, L., (1993b). *Numerical modeling of submarine landslides and surface water waves which they generate*. PhD thesis, The University of British Columbia.

Jirka, G., and Doneker, R.., (1992). Hydrodynamic classification of submerged single-port discharges. *Journal of Hydraulic Engineering*, *117*(9), 1095-1112.

Jirka, G. H. (2004). Integral model for turbulent buoyant jets in unbounded stratified flows . part I: single round jet. *Environmental Fluid Mechanics*, 1-56.

Johnson, B., (1974). Investigation of mathematical models for the physical fate prediction of dredged material. *Technical Report D-74-1, US Army Engineer Waterways Experiment Station, Vicksburg,* MS.

Kirwan, A., Doyle, L., Bowles, W. and Brooks, G., (1986). Time-dependent hydrodynamic models of turbidity currents analyzed with data from the Grand Banks and Orleansville events. *Journal of Sedimentary Petrology*, 56, 379-386.

Koh, R , and Brooks, N., (1975). Fluid mechanics of waste-water disposal in the ocean. *Annual Review of Fluid Mechanics*, *7*(1), 187-211.

Kotsovinos, N., (2000). Axisymmetric submerged intrusion in stratified fluid. *Journal of Hydraulic Engineering*, *126*(6), 446-456.

Kneller, B., and Buckee, C., (2000). The structure and fluid mechanics of turbidity currents: a review of some recent studies and their geological implications. *Sedimentology, 47*, 62-94.

Kuenen, P., (1952). Estimated size of the Grand Banks turbidity current. *American Journal of Science, 250*, 874-884.

Krieger, I., and Dougherty, T., (1959). A mechanism for non-Newtonian flow in suspensions of rigid spheres. *Transactions of the Royal Society of Rheology, 3*, 137-152.

La Rocca, M., Adduce, C., Sciortino, G., and Pinzon, A., (2008). Experimental and numerical simulation of three-dimensional gravity currents on smooth and rough bottom. *Physics of Fluids*, *20*, 106603.

List, E., and Imberger, J. (1973). Turbulent entrainment in buoyant jets and plumes. *Journal of the Hydraulic division*, *99*, 1461-1472.

Lister, J., and Kerr, R., (1989). The propagation of two-dimensional and axisymmetric viscous gravity currents at a fluid interface. *Journal of Fluid Mechanics, 203*, 215-249.

Liu, K., and Mei, C., (1990) Approxiamtae equatios for the slow propagation of a thin sheet of Bingham plastic fluid. Physics of Fluids, 2: 30-36

Marks, B. J. (1994). *Initial Dilution of a Horizontal Jet in a Strong Current*. MS thesis, The University of British Columbia, Canada.

Maxworthy, T., (1983). Gravity currents with variable inflow. *Journal of Fluid Mechanics, 128*, 247-257.

McAnally, W., Friedrichs, C., Hamilton, D., Hayter, E., Shrestha, P., Rodriguez, H., and et al. (2007). Management of Fluid Mud in Estuaries, Bays, and Lakes. I: Present State of Understanding on Character and Behavior. *Journal of Hydraulic Engineering , 133*, 9.

Meiburg, E., and Kneller, B., (2010). Turbidity currents and their deposits. *Annual Review of Fluid Mechanics*, 42, 135-156.

Middleton, G., (1993). Sediment deposition from turbidity currents. *Annual Review of Earth and Planetary Sciences, 21*, 89-114.

Merton, B., and Middleton, J., (1973). Scale diagrams for forced plumes. J*ournal of Fluid Mechanics,* 58, 165-176..

Mulder, T., Syvitski, J. and Skene, K., (1998). Modeling of erosion and deposition by turbidity currents generated at river mouths. *Journal of Sedimentary Research, 68*, 124-137.

Neal, R., Henry, G. and Greene, S., (1978). Evaluation of the submerged discharge of dredged material slurry during pipeline dredge operations. *TR D-78-44, US Army Engineers Waterways Experiment Station*, Vicksburg, Mississippi, 176 p.

Necker, F., Haertel, C., Kleiser, L. and Meiburg, E., (2002). High-resolution simulations of particle-driven gravity currents. *International Journal of Multiphase Flow, 28*, 279-300.

Ng, C., and Fu, S., (2002). On the propagation of a two-dimensional viscous density current under surface waves . *Physics of Fluids, 14*, 970-984.

Ng, C., and Mei, C., (1994). Roll waves on a shallow layer of mud modelled as a power-law fluid. *Journal of Fluid Mechanics, 263*, 151-183.

Nichols, M., Thompson, G., and Faas, R. (1978). A field study of fluid mud dredged material: its physical nature and dispersal. *Technical Report D-78-40, US Army Engineers Waterways Experiment Station*, Vicksburg, Mississippi, p 91.

Papakonstantis, I., and Christodoulou, G., (2010). Propagation of round dense jets impinging on a horizontal bottom. *Journal of Hydro-environment Research*, 1-12. Elsevier B.V. doi: 10.1016/j.jher.2010.07.001.

Papanicolaou, P., and List, E., (1988). Investigations of round vertical turbulent buoyant jets. *Journal of Fluid Mechanics, 195*, 341-391.

Pascal, H., (2000). The spread of a Non-Newtonian power law fluid under a shallow ambient layer . *Journal of Applied Mathamatics and Mechanics, 80*, 399-409.

Pascal, H., (1991). Gravity flow of a Non-Newtonian fluid sheet on an inclined plane . *Journal of Engineering Science, 29*, 1307-1313.

Rajaratnam, N. (1976). *Turbulent jets*. Elsevier Science Ltd.

Robinson, T., Simmons, R., and Earnes, I., (2005). The effect of wave action on gravity currents. *In Proceedings of Coastal Dynamics CD05, ASCE.*

Rottman, J., and Simpson, J., (1983). Gravity currents produced by instantaneous releases of a heavy fluid in a rectangular channel. *Journal of Fluid Mechanics, 135*, 95-110.

Schubel, J., Carter, H., Wilson, R., Wise, W., and Heaton, M. , (1978). Field investigations of the nature, degree, and extent of turbidity generated by open-water pipeline disposal operations. *Technical Report D-78-30, US Army Engineer Waterways Experiment Station, Vicksburg,* MS.

Seymour, R.J., (1986). Nearshore auto-suspending turbidity flows. *Ocean Engineering*, 13(5), 435-447.

Simpson, J., (1972). Effects of the lower boundary on the head of a gravity current. *Journal of Fluid Mechanics, 53,* 759-768.

Simpson, J., (1997). *Gravity currents: In the environment and the laboratory*. Cambridge University Press, p. 244.

Simpson, J., and Britter, R., (1979). The dynamics of the head of a gravity current advancing over a horizontal surface. *Journal of Fluid Mechanics, 1994*, 477-495.

Slim, A., (2006). *High Reynolds number gravity currents*. PhD Thesis, University of Cambridge.

Spearman, J., Brayb, R., Landb, J., Burta, T., Mead, C., and Scott, D. (2007). Plume dispersion modelling using dynamic representation of trailer dredger source terms. *Estuarine and Coastal Fine Sediments Dynamics INTERCOH 2003,* 417-448. Elsevier.

Takagi, D., and Huppert, H., (2007). The effect of confining boundaries on viscous gravity currents. *Journal of Fluid Mechanics, 577*, 495-505.

Teeter, A., (2002). Sediment Dispersion near dredge pipeline discharge in Laguna Madre, Texas. *Technical Note DOER-N-16, US Army Engineer Waterways Experiment Station, Vicksburg, MS*.

Teeter, A., (2001). Simulating underflow propagation from a shallow-water pipeline disposal. *Technical Note TN-DOER-N11, US Army Engineer Waterways Experiment Station, Vicksburg, MS*.

Teeter, A., (2000). Underflow propagation from an open-water pipeline disposal. *Technical Note TN-DOER-N7, US Army Engineer Waterways Experiment Station, Vicksburg, MS*.

Teeter, A., (1992a). Viscous characteristics of channel-bottom muds. *Technical Note TN-DRP-2-02, US Army Engineer Waterways Experiment Station, Vicksburg, MS*.

Teeter, A., (1992b). Erosion of cohesive dredged material in open-water disposal sites. *Technical Note TN-DRP-1-07, US Army Engineer Waterways Experiment Station, Vicksburg, MS*.

Thevenot, M., Prickett, T., and Kraus, N., (1992). Tylers Beach, Virginia, dredged material plume monitoring project, 27 September to 4 October 1991. *Technical Report DRP-92-7, US Army Engineer Waterways Experiment Station, Vicksburg, MS*.

Ungarish, M., (2009). *An introduction to gravity currents and intrustions*. Chapman and Hall/CRC Press, Boca Raton, Florida,. p 489.

USACE. (1983). Dredging and dredged material Disposal: *Enginneering Manual EM-1110-2-5025, US Army Corps Engineers, Washington, DC*.

Van Kessel, T., and Kranenburg, C. (1996) Gravity Current of Fluid Mud on Sloping Bed. Journal of Hydraulic Engineering, 123: 710-717

Vola, D., Babik, F. and Lathce, J., (2004). On a numerical strategy to compute gravity currents of non-Newtonian fluids. *Journal of Computational Physics, 201*, 397-420.

Von Karman, T., (1940). The engineer grapples with nonlinear problems. Bull. Am. Math. Soc., 46, 615-683.

Wang, H., and Law, W. (2002). Second-order integral model for a round turbulent buoyant jet. *Journal of Fluid Mechanics, 459*, 397-428. doi: 10.1017/S0022112002008157.

Whitehouse, R., Soulsby, R., Roberts, W., and Mitchener, H., (2000). *Dynamics of estuarine muds: a manual for practical applications*. Thomas Telford, London, p 209.

Winterwerp, J., and Kesteren, W. V., (2004). *Introduction to the physics of cohesive sediment in the marine environment,* Elsevier, Amsterdam. p 466.
